DEVELOPMENT OF A MULTIPLE ENERGY SYNCHROTRON BIOMEDICAL IMAGING SYSTEM

A Thesis Submitted to the

College of Graduate and Postdoctoral Studies

in Partial Fulfillment of the Requirements

for the Degree of Doctor of Philosophy

in the Department of Physics and Engineering Physics

University of Saskatchewan

Saskatoon

By

Bassey Ekpenyong Bassey

PERMISSION TO USE

In presenting this thesis in partial fulfillment of the requirements for a Postgraduate degree from the University of Saskatchewan, I agree that the Libraries of this University may make it freely available for inspection. I further agree that permission for copying of this thesis in any manner, in whole or in part, for scholarly purposes may be granted by the professor or professors who supervised my thesis work or, in their absence, by the Head of the Department or the Dean of the College in which my thesis work was done. It is understood that any copying or publication or use of this thesis or parts thereof for financial gain shall not be allowed without my written permission. It is also understood that due recognition shall be given to me and to the University of Saskatchewan in any scholarly use which may be made of any material in my thesis.

Requests for permission to copy or to make other uses of materials in this thesis in whole or part should be addressed to:

Head of the Department of Physics and Engineering Physics
116 Science Place
University of Saskatchewan
Saskatoon, Saskatchewan S7N 5E2
Canada

OR

Dean
College of Graduate and Postdoctoral Studies
University of Saskatchewan
116 Thorvaldson Building, 110 Science Place
Saskatoon, Saskatchewan S7N 5C9
Canada

ABSTRACT

A multiple energy imaging (MEI) system that can extract multiple endogenous or induced contrast materials as well as water and bone images would be ideal for imaging of biological subjects. The continuous spectrum available from synchrotron light facilities provides a nearly perfect source for MEI. This dissertation is on a novel MEI imaging system developed for biomedical imaging applications at the BioMedical Imaging and Therapy bend magnet beamline, Canadian Light Source. The developed MEI system prepares a horizontally focused polychromatic x-ray imaging beam. Its components are: a cylindrically bent Laue single silicon (5, 1, 1) crystal monochromator, scanning and positioning stages for the subjects, flat panel (area) detector, and a data acquisition and control system. The Si crystal is bent by means of a frame bender and has a bent radius of 0.5 m. Depending on the horizontal beam width of filtered synchrotron radiation (20 to 50 keV) incident on the monochromator; the size and spectral energy range of the focused beam prepared vary, and can be up to 15 keV. The spectral energy range covers the K-edges of iodine (33.17 keV), xenon (34.56 keV), cesium (35.99 keV), and barium (37.44 keV). Iodine, xenon and barium are commonly used biomedical and clinical contrast agents. A phantom composed of six materials: iodine, xenon, cesium, barium, water, and bone was imaged using the MEI system and their projected concentrations successfully extracted. For quantification of iodine, cesium and barium, the minimum detection limit of the MEI system is about 1.0 mg/ml for iodine and barium, and 0.5 mg/ml for cesium. The estimated dose rate to the phantom imaged at a ring current of 200 mA is 8.7 mGy/s, corresponding to a cumulative dose of 1.3 Gy. A crossover correction algorithm has also been developed to suppress crossover artifacts associated with the MEI system, dual-beam KES and spectral KES systems. Potential biomedical applications of the imaging system will include projection imaging that requires any of the extracted K-edges as a contrast agent and multi-contrast K-edge imaging.

ACKNOWLEDGEMENTS

I am, and will ever remain grateful to my supervisor Dr. Dean Chapman; his love for science knows no bounds. Not only has he been a supervisor to me but also a father- his support and advices were not limited to academics.

I acknowledge the contributions of my Academic Advisory Committee members: Dr. Rob Pywell, Dr. Alexander Moewes, Dr. David Cooper, and Dr. Andrew Alexander. I will never forget the role played by Dr. Chary Rangacharyulu in the first year of my PhD studies, without him, I would not have ended up being Dr. Dean Chapman's student. Thanks Dr. Chary. To Debbie Gjertsen and Marjorie Granrude, I say thank you for all the supports they offered to me. The contributions of Dr. George Belev, the BMIT facility staff, and members of the X-ray Imaging Group to this work will always be appreciated.

Dr. Dean Chapman is a Mentor, and I am a Fellow, in the Canadian Institutes of Health Research Training grant in Health Research Using Synchrotron Techniques (CIHR-THRUST). The financial support from the Natural Sciences and Engineering Research Council of Canada (NSERC), and the Canada Research Chair program is acknowledged. The research described in this thesis was performed at the CLS, which is funded by the Canada Foundation for Innovation, the NSERC, the National Research Council Canada, the CIHR, the Government of Saskatchewan, Western Economic Diversification Canada, and the University of Saskatchewan.

Acknowledged also is the support from my academic father and mentor, Professor David Eka of the University of Uyo, Nigeria. He made it possible for me to come over to Canada for graduate studies. The support from my uncle, Obong Okon Udo Ekpo is greatly appreciated. I am thankful to the Management of Akwa Ibom State University (AKSU) for the financial support during the first two years of my PhD studies. I appreciate the encouragement from my fellow AKSU colleagues- Dr. Aniekan Williams, Dr. Cletus Asuquo, Dr. Samuel Hanson, and Dr. Ubong Peters. I am thankful to God for the successful completion of our various PhD studies here in Canada.

Finally, I acknowledge the support and prayers from members of the Akwa Ibom State community, Saskatoon: Mrs. Nse Umoh, Inimfon Udoetok, Dr. Ubong Eduok, and Dr. Peter Ekanem, just to mention a few.

DEDICATION

To my late father Robin Ekpenyong Bassey.
Rest in peace father, your desire for me to attain this level of education has been granted.

To late Dr. Chris Newcomb, a member of my Academic Advisory Committee, who because of death did not live to see the completion of this research. May his soul rest in peace.

To my loving wife Iniobong, kids-Blessing, Ubokobong and Godswill, precious mother Affiong and siblings-Blessing, Emmanuel, Mfonobong, Ekaette, Anietie, and Emem.

CONTENTS

LIST OF TABLES

LIST OF FIGURES

LIST OF ABBREVIATIONS

BLA	Bent Laue Analyzer
BMIT	Biomedical Imaging and Therapy
BMIT-BM	Biomedical Imaging and Therapy Bend Magnet
BMIT-ID	Biomedical Imaging and Therapy Insertion Device
CLS	Canadian Light Source
CMOS	Complementary Metal-Oxide Semiconductor
CNR	Contrast-to-Noise Ratio
CT	Computed Tomography
DECT	Dual-Energy Computed Tomography
EID	Energy Integrating Detector
EM	Electromagnetic Waves
ESRF	European Synchrotron Radiation Facility
EXAFS	Extended X-ray Absorption Fine Structure
FB	Frame Bender
FFB	Four-Bar Bender
FPD	Flat Panel Detector
FWHM	Full-Width-Half-Maximum
HOPG	Highly-Oriented Pyrolytic Graphite
ID	Internal Diameter
KES	K-edge Subtraction
kVp	KiloVoltage peak
LLSQ	Linear Least Squares
MECT	Multiple Energy Computed Tomography
MEI	Multiple Energy Imaging
MIR	Multiple Image Radiography
NNLQ	Non-Negative Least Squares
NSLS	National Synchrotron Light Source
OD	Outer Diameter
PCD	Photon Counting Detector
POE	Primary Optical Enclosure
QM	Quasi-Mosaic

SLS	Swiss Light Source
SNR	Signal-to-Noise Ratio
SR	Synchrotron Radiation
SSRF	Shanghai Synchrotron Radiation Facility
SYRMEP	SYnchrotron Radiation for MEdical Physics
TOMCAT	TOmographic Microscopy and Coherent rAdiology experimenTs
XAFS	X-ray Absorption Fine Structure
XANES	X-ray Absorption Near Edge Spectroscopy
XAS	X-ray Absorption Spectroscopy

CHAPTER 1

INTRODUCTION

Generally, imaging has revolutionized the practice of health care since the discovery of x rays by Wilhelm Conrad Roentgen in 1895. It is extensively used for screening, diagnosis, and monitoring of the treatment of disease. X-ray imaging, be it in the medical or biomedical sciences, is a transmission-based technique in which x-rays from a source pass through a subject and are detected on the opposite of the subject by a detector (e.g. film or ionization chamber) [1]. An x-ray image is a representation of the spatial distribution of the x-ray energies (quanta) transmitted through a subject on a plane perpendicular to the direction of the incident x-ray beam [2]. If x-rays incident on a subject do not penetrate and undergo any form of interaction (e.g., absorption, scattering, diffraction, refraction, reflection) within the subject, then the detected x-rays will not contain information from which the image of the subject can be created [3]. X-ray imaging can be performed in either two-dimensional (planar) or three-dimensional (computed tomography-CT) mode. Irrespective of the mode, the ability to measure or differentiate the absorption characteristics makes material characterization possible [4, 5]. This is because the energy spectrum of x-rays after passage through a material contains information about the material such as its elemental composition, density, thickness, atomic size, atomic shape and atomic arrangements [5]. The continual drive to improve and expand the amount of information extracted from various x-ray imaging modalities has led to the use of multiple x-ray photon energies in imaging. Multiple energy x-ray imaging (MEI), also referred to as spectral x-ray imaging [6, 7], is the use of two (dual-energy) or more x-ray photon energies for imaging. With MEI, two or more materials can be segmented based on spectral absorption differences. MEI has been widely shown to be of benefit to medical and security applications [8-10]. Clinically, MEI has the potential to expand the application of tissue differentiation [4], and the ability to separate tissue types improves image contrast and diagnostic accuracy [11]. The interest in MEI is not only with the use of conventional x-ray sources but also with synchrotron x-ray sources [12]. Conventional x-ray sources as used in this thesis refers to x-ray tubes used in research laboratories, clinics and hospitals, and for which the energy range of x-rays produced is within the diagnostic energy range of 18 to 150 keV [1, 3].

The Canadian Light Source (CLS) is a third generation synchrotron light (radiation) source [13] and has several beamlines, which include the two beamlines of the Biomedical Imaging and Therapy (BMIT) facility-bending magnet (BMIT-BM) and insertion device (BMIT-ID) beamlines [14-16]. BMIT is among the eight existing biomedical imaging beamlines at synchrotron radiation (SR) facilities across the world. Others are: Biomedical beamline ID 17 at the European SR facility (ESRF), France [17]; Tomographic Microscopy and Coherent radiology experiments (TOMCAT) beamline at the Swiss Light Source (SLS) [18]; X-ray imaging and biomedical applications beamline (BL13W1) at the Shanghai SR facility (SSRF) [19]; SR for medical physics (SYRMEP) beamline at the Elettra SR facility, Italy [20]; Australian synchrotron imaging and medical beamline (IMBL) [21]; Beamline BL20B2 at SPring-8 SR facility, Japan [22]; and Beamline BL14C at the Photon Factory SR facility, Japan[23]. The imaging techniques at the BMIT-BM beamline are [24]: conventional absorption imaging; diffraction enhanced imaging (DEI), multiple image radiography (MIR); phase contrast or in-line holography; ultra-small, small, and wide angle scatter imaging in both projection (2D) or CT modes. This thesis is on a novel MEI system developed at the BMIT-BM beamline for biomedical imaging applications.

1.1 Aim

The primary optical enclosure-2 (POE-2) of the BMIT facility is the experimental hutch of BMIT-BM beamline. In POE-2, one can access either a white beam, that is, polychromatic SR or monochromatic x-rays (energy range: 20 - 40 keV) for experiments. We aimed at developing a novel bent crystal imaging system that will prepare a focused polychromatic x-ray beam for the simultaneous use of more than one x-ray (photon) energy for x-ray imaging of biomedical subjects. The imaging system will allow for identification of tissues types and contrast elements based on their wide energy range absorption properties. It will help provide a unique capability to augment other synchrotron imaging techniques available at the BMIT facility. Considering that a filtered white beam of energy range 20-50 keV is to be used, we are also interested in the number of materials concentrations that can be extracted from a subject imaged using the imaging system. The energy range 20-50 keV matches the lower end of the diagnostic imaging energy rage accessible by BMIT-BM, and includes the absorption edges (K-edges) of the

following elements: indium (27.940 keV), tin (29.200 keV), antimony (30.491 keV), tellurium (31.814 keV), iodine (33.169 keV), xenon (34.561 keV), cesium (35.985 keV), barium (37.441 keV), and lanthanum (38.925 keV). Some of these elements (iodine, xenon, barium) are commonly used as clinical and biomedical contrast agents.

1.2 Outline

Following this introductory chapter (Chapter 1) is a chapter in which some of the basic physics of x-rays are covered - Chapter 2. A critical component of the novel MEI synchrotron imaging system developed is single cylindrically bent Laue crystal. This necessitated the dedication of a chapter to bent Laue crystal optics, Chapter 3. An overview of MEI, including known established MEI methods that use conventional and synchrotron x-rays, is presented in Chapter 4. The focus of Chapter 5 is on the components of the novel MEI system, the measurements and results of various studies on the system. Images obtained from imaging systems are susceptible to artifacts, and this is the case with the developed novel imaging system. In Chapter 6, the crossover artifact, a major artifact peculiar to x-ray focusing imaging systems, is addressed. Finally, the conclusion and likely future work related to the MEI system are presented in Chapter 7.

1.3 Academic Contributions

The research reported in this thesis has been presented at three international conferences and was well received, resulted in two publications-a journal article and a conference paper, and two manuscripts. The two manuscripts are titled “Crossover artifacts in x-ray focusing imaging system: K-edge subtraction imaging” and “Bent Laue crystal optics: technology and application” (a review). Also, during the period of this research I have led and actively participated in other published research works. These publications are listed as follows along with my contributions. The publication listed as (1) was picked as one of the best articles published in the Institute of Physics (IOP) Biomedical Journals, and a cover story was written on it. The copyrights to use all or part of my published work in this thesis, as well as figures from other published work are presented in Appendix A.

(1) **B. Bassey**, M. Martinson, N. Samadi, G. Belev, C. Karanfil, P. Qi, D. Chapman (2016) Multiple energy synchrotron biomedical imaging system *Phys. Med. Biol.* **61**, 8180-8198: *I led the research and was involved in the experiments, analyzed the data, prepared and submitted the manuscript for publication.*

(2) N. Samadi, M. Martinson, **B. Bassey**, A. Gomez, G. Belev, D. Chapman (2016) An energy dispersive bent Laue monochromator for K-edge subtraction imaging *AIP Conf. Proc.* **1741**, 040004-1 - 040004-4: *I was involved in the experiments and writing of the paper.*

(3) **B. Bassey**, M. Mercedes, N. Samadi, G. Belev, C. Karanfil, D. Chapman (2015) Multiple Energy Synchrotron Biomedical Imaging System- Preliminary Results *Proc. of IFMBE* vol. **51**, 248-251: *I led the research and was involved in the experiments, analyzed the data, prepared and submitted the manuscript for publication.*

(4) **B. Bassey**, M. Beatriz, D. Chapman (2015) Synchrotron radiation shielding design and ICRP radiological protection quantities *J. Radiol. Prot.* **35**, 383: *I led this research, did the shielding calculations and also led in the writing and submission of the manuscript for publication.*

(5) N. Samadi, **B. Bassey**, M. Martinson, G. Belev, L. Dallin, M. de Jong, D. Chapman (2015) A phase-space beam position monitor for synchrotron radiation *J. Synchrotron Radiat.* **22**, 946-955.: *I did the literature search on beam position monitors and wrote the introduction section of the manuscript. I also proofread the manuscript.*

(6) M. Martinson, N. Samadi, **B. Bassey**, A. Gomez, D. Chapman (2015) Phase-preserving beam expander for biomedical X-ray imaging *J. Synchrotron Radiat.* **22**, 801-806: *I was involved in the experimental aspect of the research.*

(7) S. Wiebe, N. Samadi, G. Belev, M. Martinson, **B. Bassey**, D. Chapman (2015) Small and Ultra-Small Angle X-Ray Scattering Contrast Obtained With a Synchrotron-Based Shack-Hartmann Imaging System *IEEE Transactions on Nuclear Science* **62**, 2031-2035: *I was involved in the experimental aspect of the research.*

(8) **B. Bassey**, A. Abueidda, G. Cubbon, D. Street, A. Sabbir Ahmed, T.W. Wysokinski, G. Belev, D. Chapman (2014) Supplemental shielding of BMIT SOE-1 at the Canadian Light Source *Radiat. Phys. Chem.* **100**, 8-12: *I did the shielding calculations and led the writing and submission of the manuscript for publication.*

(9) **B. Bassey**, B. Moreno, A. Gomez, A.S. Ahmed, D. Ullrich, D. Chapman (2014) Synchrotron radiation shielding design for the Brockhouse sector at the Canadian light source *Radiat. Phys. Chem.* **98**, 109-112: *I did the shielding calculations and led in the writing and submission of the manuscript for publication.*

(10) M. Martinson, N. Samadi, G. Belev, **B. Bassey**, R. Lewis, G. Aulakh, D. Chapman (2014) Development of a bent Laue beam-expanding double-crystal monochromator for biomedical X-ray imaging *J. Synchrotron Radiat.* **21**, 479-483: *I was involved in the experimental aspect of the research, and proofreading of the manuscript.*

(11) Y. Zhu, N. Samadi, M. Martinson, **B. Bassey**, Z. Wei, G. Belev, D. Chapman (2014) Spectral K-edge subtraction imaging *Phys. Med. Biol.* **59**, 2485-2503: *I was involved in the experimental aspect of the research, and writing of the manuscript.*

(12) D. Chapman, N. Samadi, M. Martinson, **B. Bassey**, S. Boire, G. Belev, T. Wysokinski (2014) X-Ray Optics Development for Biomedical Imaging Applications at the Canadian Light Source *Phys. Can*. **70**, 19-23. *I was involved in some of the experiments reported in the paper, and the writing and proofreading of the manuscript.*

The three international conferences at which I gave an oral presentation of this research are:

(1) **B. Bassey**, M. Martinson, N. Samadi, G. Belev, C. Karanfil, D. Chapman (2015) Multiple Energy Synchrotron Biomedical Imaging System. *The 8th Medical Applications of Synchrotron Radiation Conference* October 5-8, Grenoble & Villard de Lans, France

(2) **B. Bassey**, M. Martinson, N. Samadi, G. Belev, C. Karanfil, D. Chapman (2015) Multiple Energy Synchrotron Biomedical Imaging System. *The 12th International Conference on Synchrotron Radiation Instrumentation* July 6-10, New York City, USA

(3) **B. Bassey**, M. Martinson, N. Samadi, G. Belev, C. Karanfil, D. Chapman (2015) Multiple Energy Synchrotron Biomedical Imaging System-Preliminary Results. *The 13th World Congress on Medical Physics and Biomedical Engineering* June 7-12, 2015, Toronto, Canada

CHAPTER 2

BASIC PHYSICS Of X RAYS

In physics, the terms wave and radiation are often used interchangeably [2, 25]. In this thesis the term radiation will refer to electromagnetic radiation or photons. Radiation is a disturbance that propagates in space and time, which usually results in the transfer of energy from one point to another; radiation is energy that propagates through space or matter [3]. Waves can be classified based on the direction of their propagation with reference to that of the disturbance: transverse waves if the waves propagate in a direction perpendicular to the direction of disturbance; longitudinal waves if the direction of propagation is the parallel to that of the disturbance. Waves can also be classified based on whether or not a material medium is required for their propagation: for example, sound wave is a type of mechanical wave that require a material medium whereas electromagnetic waves (EM) require no material medium. An x-ray is a transverse electromagnetic wave where the electric and magnetic fields are perpendicular to each other and to the direction of propagation [25]. In addition to not requiring a material medium for their propagation, all EM waves exhibit some common properties [3]- have no mass, are unaffected by either electrical or magnetic fields, have a constant speed in a particular medium, and a maximum group velocity or speed of 2.998 x 10^8 m/s in vacuum. This maximum speed is usually denoted by *c*, and referred to as the velocity of light. For a given type of EM wave, the relation between *c*, frequency (*f*) and wavelength (λ) of the wave is:

$$c = \lambda f \tag{2.1}$$

EM waves are sometimes treated as particles; their treatment as waves explains why they may undergo reflection, refraction, polarization, and diffraction while their ability to interact with matter is best explained when they are treated as particles [26]. When EM waves are treated as particles, they are considered as discrete bundles of energy called photons or quanta. The energy, E, of a photon is given by [3]:

$$E = hf \tag{2.2}$$

where h, is called the Planck's constant, 6.62 x 10^{-34} J-s (4.13 x 10^{-18} keV-s). From eqn. (2.1), eqn. (2.2) can also be written as:

$$E = \frac{hc}{\lambda} \tag{2.3}$$

When E is expressed in keV and λ in nanometers (nm), eqn. (2.3) becomes:

$$E\ (keV) = \frac{1.24}{\lambda(nm)} \tag{2.4}$$

A representation of all EM waves in terms of their wavelengths and frequencies is referred to as the EM spectrum (figure 2.1). The differences in properties of the different types of EM waves are attributed to their differences in wavelength (or frequency), for an example, the wavelength of an EM wave determines how it interacts with matter [26]. As shown in figure 2.1, x-rays have very short wavelengths, ranging from 10 - 0.01 nm (100 - 0.1 Angstrom, Å); x-rays with wavelengths 10 nm - 0.1 nm (100 - 1 Å) and 0.1 nm - 0.01 nm (1 to 0.1 Å) are called soft and diagnostic (hard) x-rays, respectively [26].

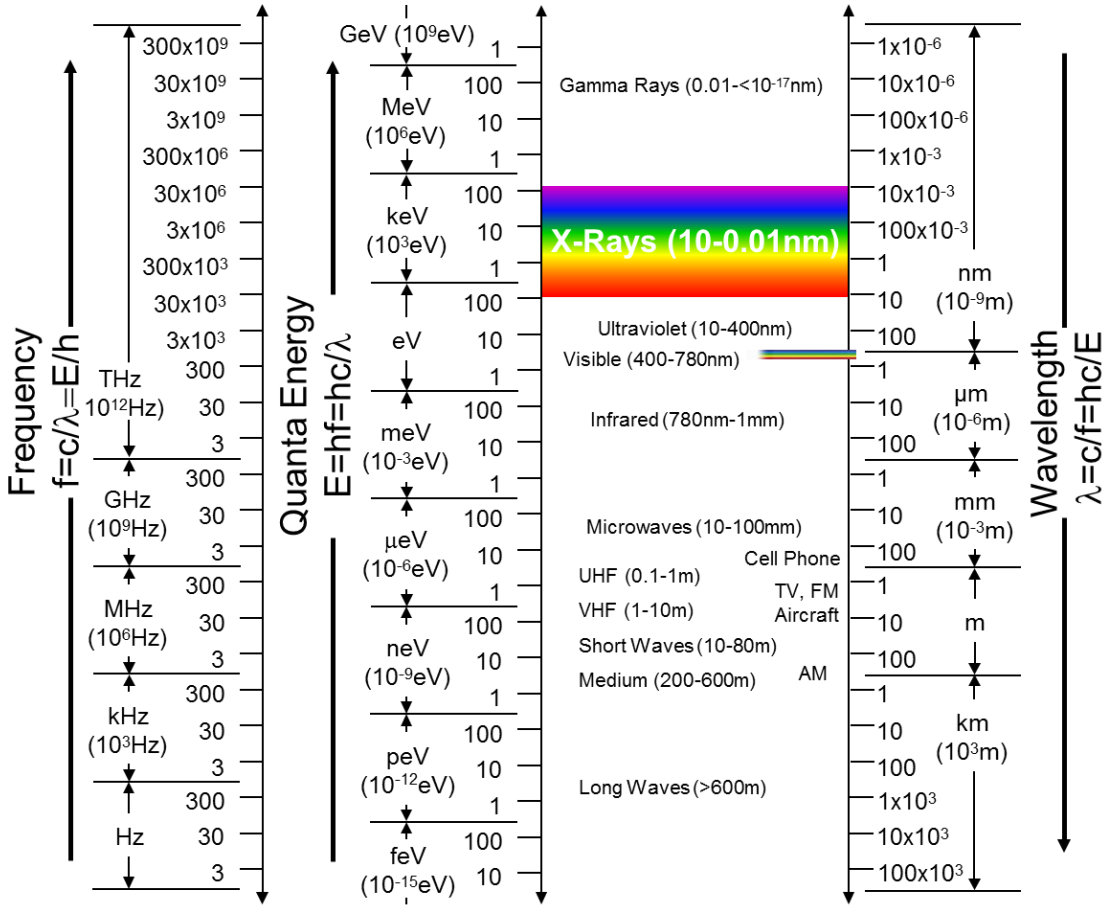

Figure 2.1: The electromagnetic spectrum showing the frequency, wavelength and energy of light most commonly used. **Source:** Synchrotron Imaging Methods (BIOE 850) lecture notes by Dean Chapman, used with permission.

2.1 Production of X rays

There are two main processes through which x-rays are produced: the acceleration of charged particles (usually electrons) and the transition of electrons from one atomic or ionic energy level to a lower one [2]. Electrons are not the only known charged particle, other examples are protons, deuterons, and alpha particles (helium atom nuclei). But in the production of x-rays via acceleration of charged particles, electrons are preferred because electrons are less massive. For example, the mass of a proton is 1836 times larger than that of an electron and under the same condition, protons will produce fewer of x-rays than electrons [3, 27, 28]. Another advantage of using electrons is that electrons can be easily and efficiently produced because electrons are found in every solid [27]. The production of conventional x-rays (x-rays produced from a conventional x-ray tube) involves the above two mentioned processes while in the production of synchrotron x-rays, only the acceleration of electrons is involved.

In a conventional x-ray tube, the main components are: filament, metal target, and an air evacuated glass or metal envelope. The filament is part of the cathode (negatively charged) and serves as the source of electrons while the metal target is part of the anode (positively charged). Though there have been several designs of x-ray tubes since its invention, the fundamental principles of operation have remained the same [29]. On passing electric current through the filament, it becomes heated and results in the production of electrons. This process of producing electrons is called thermionic emission. An applied potential difference (voltage), normally stated in kilovoltage peak (kVp), between the cathode and anode causes the electrons produced to be accelerated to the metal target. The kinetic energy acquired by the accelerated electrons is proportional to the applied potential difference [3]. As the electrons hit the metal target, their kinetic energies are converted to heat and x-rays. The spectrum of x-rays produced has two parts [25]. The first, dominant, and continuous part is called bremsstrahlung x-rays, produced due to sudden deceleration and stopping of the high-speed electrons by the metal target. The electrons deceleration is attributed to the inelastic interactions between the electrons and atomic nuclei of the metal target. These interactions result in a deflection of the electrons paths by the positively charged nuclei with a loss in kinetic energies of the electrons, which are converted to x-rays. It should be noted that the kinetic energies of the electrons are not actually lost but converted to x-rays. Thus, the energy of a bremsstrahlung x-ray photon can be any value up to and including the entire kinetic energy of the deflected electron [3]. A bremsstrahlung x-ray is said to have a

maximum energy (E_{max}) if the entire kinetic energy of an electron is converted, and the value of E_{max} in keV corresponds to the value of the accelerating voltage-the maximum value of the applied voltage [1]. The second part of the x-rays spectrum is called characteristic x-rays, which are discrete energy peaks superimposed on the bremsstrahlung x-ray spectrum. Characteristic x-rays, attributed mostly to electron-electron interactions, are produced when electrons descend from a higher to a lower atomic shell. Bremsstrahlung-electron interaction through the process of photoelectric effect also contributes to the production of characteristic x-rays [3]. An atom is made of a central nucleus containing proton(s) and surrounded by various orbits or shells in which electrons reside. The shells of an atom are designated as K, L, M, N, etc., with K shell being the innermost, highest and closest shell to the nucleus. Also, the electrons in the K shell have the highest binding energy [1]. An electron can only descend from, say, an L to a K shell, if there is a vacancy in the K shell. For a vacancy to be created in the K shell (i.e. removal of an electron from the K shell), the kinetic energies of the accelerated electrons must be higher than the binding energy of a K-shell electron of the metal target atom. Characteristic x-rays are named based on the shell in which the vacancy occurred, and the most common in the diagnostic energy range is the K-characteristic x-rays, which result from the filling of K-shell vacancies by electrons from the L, M and N shells [3, 29]. The K-characteristic x-rays are further designated as K_α or K_β if the electrons transitions are from L or M to the K shell, respectively. An emitted characteristic x-ray has energy equal to the difference between the electron binding energies of the two shells involved. Tungsten and molybdenum are examples of metal targets used in x-ray tubes. To produce K-characteristic x-rays in x-ray tubes with these targets, the applied voltages must be greater than 69.5 kVp for tungsten targets or 20 kVp for molybdenum targets [3].

Unlike conventional x-rays that are produced in x-ray tubes, synchrotron x-rays constitute a part of the SR spectrum produced in synchrotrons. A synchrotron is a particular type of accelerator that accelerates charged particles in circular orbit to very high relativistic energy [30]. SR refers to EM radiation emitted when electrons moving with relativistic speed (speed close to that of light, c) following a curved trajectory in vacuum under the influence of a magnetic field undergo radial acceleration [27, 30].The SR spectrum is very broad. It starts from far-infrared up to hard x-rays [28]. Apart from synchrotrons, SR is also produced in storage rings [25, 28]. In a storage ring, electrons circulate almost at the speed of light, c. At the CLS, the electrons speed is only about 5 m/s slower than c. The paths of the electrons are bent using dipole bend magnets,

and wherever the path of the electrons bends their velocity vector changes causing a radial acceleration that produces SR. A storage ring is not completely circular; it has some straight sections where insertion devices (e.g. wigglers and undulators) that also produce SR are placed. Insertion devices are periodic magnetic structures with alternating magnetic fields that force the electrons to follow oscillating paths instead of moving in a straight line [25]. It is the kinetic energy of the electrons that is converted to SR and thus, with time the electrons energy decreases. The energy lost by the electrons in the form of SR is given back to the electron's using radio-frequency cavities placed in the storage ring [13]. A schematic diagram of a storage ring is shown in figure 2.2. From the storage ring, the SR produced is then channelled using appropriate optical elements to different beamlines (experimental stations) for various experimental needs. A beamline is called a bending magnet (BM) or insertion device (ID) beamline if the SR channelled to the beamline is from a BM or ID, respectively. Bending magnets became the first and are also the commonest sources of SR for experiments because all synchrotrons and storage rings use bending magnets to keep the electrons on a circular path [27].

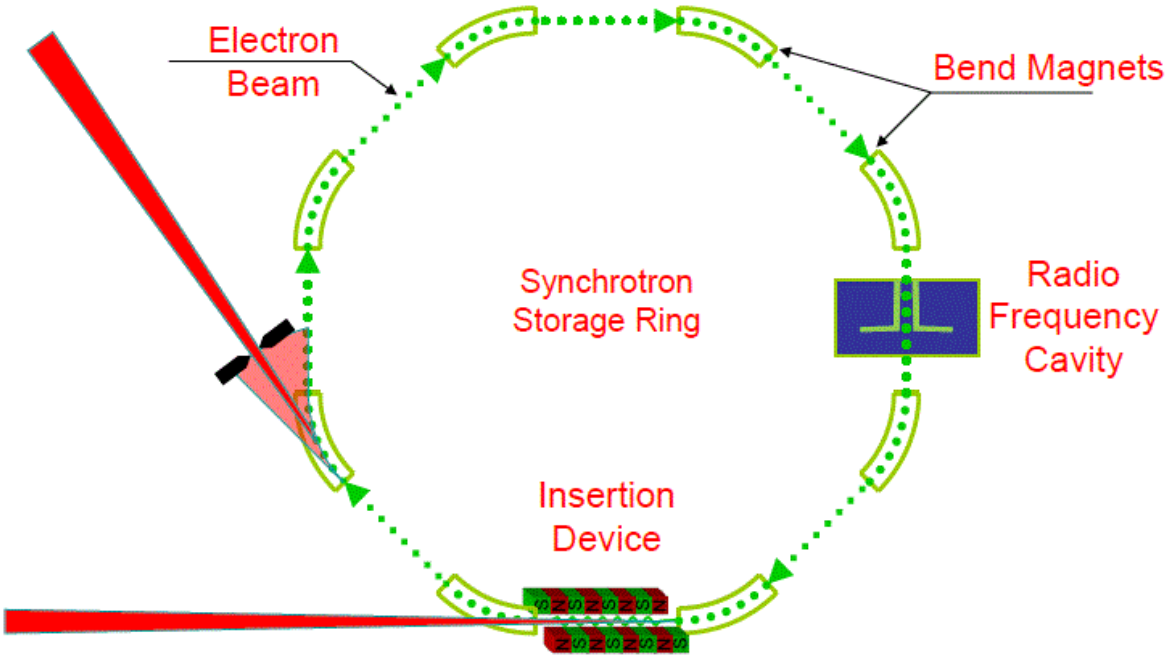

Figure 2.2: A schematic diagram of a storage ring. **Source:** Synchrotron Imaging Methods (BIOE 850) lecture notes by Dean Chapman, used with permission.

SR has some unique properties. These properties include high photon flux, wide-energy tunability (broad and continuous spectrum), natural collimation, high polarization, small source size, and pulsed time structure [13, 28]. Of these properties, natural collimation and broad spectral range are considered the most important [27]. The production of conventional and synchrotron x-rays involves the acceleration of electrons. Despite this, there are some differences in the production process that are worth emphasizing. See table 2.1.

Table 2.1. Differences in the production process of conventional and synchrotron x-rays.

	Conventional x-ray tube	**Synchrotron x-rays**
Speed, v, of the accelerated electrons	v is non relativistic. That is, v is small compared to c ($v \ll c$); 30 to 65% of c[2].	v is relativistic. That is, v is almost the same as that of light ($v \cong c$). At the CLS, v is 99.999984% of c.
Energy of accelerated electrons	In the order of 10 to 100keV.	In the order of MeV to GeV.
Acceleration of electrons	Linear acceleration.	Circular or radial acceleration.
Metal target	Accelerated electrons are made to hit a metal target.	Accelerated electrons do not hit a target. In fact, efforts are made to ensure that the electrons do not hit the walls of the pipe the electrons circulate in. If the electrons hit the walls, there will be severe hazardous effects.

2.2 Attenuation of X rays by Matter

When an x-ray beam (x-rays) is incident on a material, there will likely be some sort of interactions between the beam and the material; attenuation is one of such interactions [2]. It was earlier stated that, in considering the interactions of x-rays with materials, x-rays are typically treated as photons not as waves. There are three possible results that contribute to the loss of x-rays when an x-ray beam is incident on a material [29]. The photons, during one or more

interactions, may be (1) absorbed (transfer of photons' energy to atoms of the material), (2) scattered or (3) pass through the material without any interaction. Attenuation can be defined as the removal of photons from an x-ray beam as it traverses a material due to the absorption and scattering of the photons by the material's atoms [3, 29, 31]. The number of photons attenuated in a material is dependent on the number of photons traversing the material [29]. Assuming that: the number of photons in an x-ray beam incident on a slab of material of thickness t, is N_0; all the photons in the incident beam possess the same energy (i.e., the beam is monoenergetic or monochromatic); the photons are attenuated under conditions of good geometry (i.e., the beam is narrow and there are no scattered photons in the transmitted beam); then the number N of photons in the transmitted beam is given by [3, 29]

$$N = N_0 e^{-\mu t}, \tag{2.5}$$

where μ is the linear attenuation coefficient of the material. The number N_{at} of attenuated photons from the beam is

$$N_{at} = N_0 - N = N_0 - N_0 e^{-\mu t} = N_0(1 - e^{-\mu t}) \tag{2.6}$$

Since the exponent e has no units, if t is expressed in units of length, say, centimeters (cm) then μ will have the units of 1/length (cm^{-1}), and is called the linear attenuation coefficient-the fraction of photons removed per unit thickness of material. Linear attenuation coefficient is the most important parameter used for characterization of x-ray penetration into absorbing materials, and it depends on the energy (hf) of the photon and atomic number (Z) of the material [30]. The probability that a photon will not undergo any interaction is $e^{-\mu t}$. From eqn. (2.5), when $\mu t = 1$ or $t = 1/\mu$, $N = N_0/e$. It follows then that $1/\mu$ is the thickness of the material that N will be 1/e, or 37% of N_0.

The linear attenuation coefficient depends on the composition and density of the material. A more fundamental description of attenuation is the cross section for attenuation, σ. For a single element material the relationship between cross section and linear attenuation is:

$$\mu = \sigma_a \rho_a \tag{2.7a}$$

where ρ_a is the number of atoms per volume and the units of the cross section is area per atom. As stated before the unit of μ is inverse length. The atomic density (number of atoms per volume, ρ_a) is difficult to find, a more common property used is the mass density, ρ. If the cross section is divided by the atomic weight of the material then the atomic density can be replaced by the mass density, and μ becomes:

$$\mu = \sigma_a \rho_a = \left(\frac{\sigma_a}{Au}\right)\rho \tag{2.7b}$$

where A is the atomic weight, u is the nucleon mass and $\rho = Au\rho_a$ for a single element. Now the quantity $\frac{\sigma_a}{Au}$ is the cross section for attenuation per atomic mass. This is commonly referred to as mass attenuation coefficient and represented by $\frac{\mu}{\rho}$. Though it has the appearance of a ratio, it is a property of the atom. That is:

$$\mu = \left(\frac{\mu}{\rho}\right)\rho \tag{2.8}$$

For a multielement material, $\frac{\mu}{\rho}$ can be found using:

$$\frac{\mu}{\rho}(compound) = \sum_{i=1}^{N} \frac{\mu}{\rho_i} f_i \tag{2.9}$$

where is the mass fraction of the i[th] element. For example, the $\frac{\mu}{\rho}$ for water would be $\left(\frac{\mu}{\rho}\right)_{H_2O} = \left(\frac{\mu}{\rho}\right)_H \frac{2}{18} + \left(\frac{\mu}{\rho}\right)_O \frac{16}{18}$ since the atomic weights of hydrogen (H) and oxygen (O) are approximately 1 and 16, respectively and the molecular weight of water is 18.

Without the interaction of an x-ray beam with a material, there will be no attenuation of the beam, and the beam transmitted will not contain information about the material in the case of x-ray imaging. Thus, it is important that a brief description of the possible interactions of photons with a material be given. These interactions are as follows [1-3, 13, 25, 29, 30].

(a) ***Photoelectric absorption (photoelectric effect):*** It is an interaction in which an x-ray photon is completely absorbed by the atom of the material thereby transferring all of its energy to an electron in the atom. The excess energy now possessed by the electron enables the electron to be ejected (photoelectron) from the atom. A photoelectron has a kinetic energy that is equal to the difference between the energy of the x-ray photon and the binding energy of the electron. If the energy of the x-ray photon is less than the binding energy of a K-shell electron then only an L- or M-shell electron can be ejected. Photoelectric absorption occurs mostly with tightly bound shell (orbital) electrons - electrons with binding energy E_B that is either larger than or of the order of the photon energy (hf). Photoelectric absorption cannot occur if $E_B > hf$, its occurrence is only possible if $hf > E_B$. When $hf \geq E_B$ (K-shell electrons), over 80% of all photoelectric interactions occur with K-shell electrons. The probability of photoelectric absorption occurring increases with increase in atomic

number Z of the material but decreases as the energy E of the x-ray photon increases (i.e., it approximately depends on Z^3/E^3). The decrease in the probability of photoelectric absorption with increase in E has an exception for every element. This exception occurs at what is called the absorption edge or K-edge of an element, defined as an abrupt increase in x-ray absorption that occurs when the x-ray energy is equal to or slightly greater than the binding energy of the K-shell electrons [32]. The effect of photoelectric absorption on the mass attenuation coefficient as a function of energy shows a sharp discontinuity at the K-edge of every element, figure 2.3 shows the plots for the four elements of interest in this research as well as bone and water. From figure 3, it can be seen that the probability of photoelectric absorption for photons of energy just above a K-edge is much greater than that of photons of energy slightly below the K-edge. In x-ray transmission imaging, photoelectric absorption is considered advantageous because there are no additional non-primary photons (scattered photons) to degrade the image.

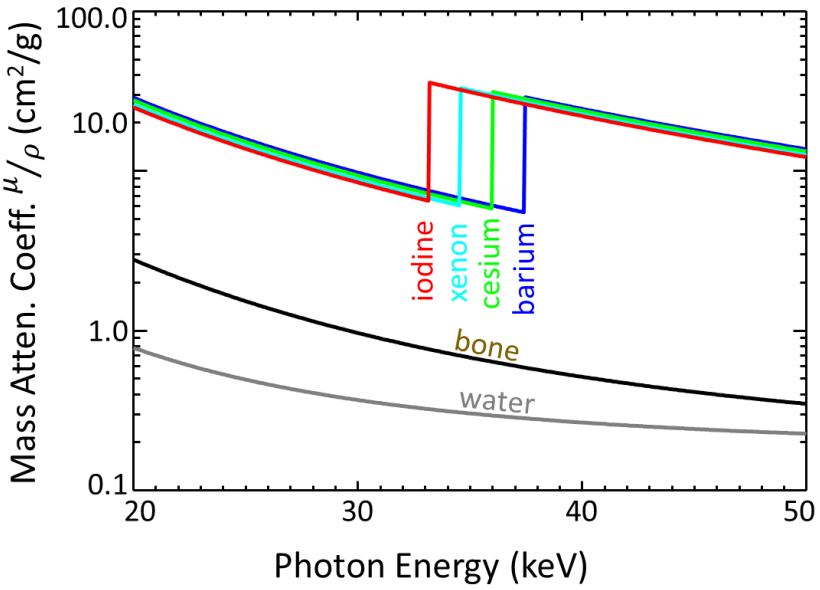

Figure 2.3: Total mass attenuation coefficients as a function of energy for iodine, xenon, cesium, barium, bone, and water. The source of the data used for the plot is Ref. [121].

(b) ***Elastic (Coherent) scattering:*** Involves the interaction of an incident x-ray photon with the electron cloud of an atom of a material as a whole but not with individual electrons. The atom becomes excited and subsequently releases the photon energy it

acquired by emitting an x-ray photon with the same energy but in a slightly different direction. Thus, there is no energy loss by the incident x-ray photon and ejection of electron. It also implies that there is no transfer of energy by the incident photon to the material. In the diagnostic energy range, elastic scattering has a low probability of occurring, and occurs mostly at very low x-ray photon energy such as that used in mammography (15 to 30 keV). As a photon loss mechanism in un-structured materials, such as crystals, the role of elastic scattering of x-rays is small compared to photoelectric absorption or Compton scattering. However, elastic scattering is the mechanism that gives rise to diffraction from ordered materials, again such as crystals. The interference phenomenon that occurs in ordered materials reinforces the scattering in to specific directions or Bragg peaks. This aspect of scattering is the basis of the operation of the monochromator which is discussed at length in later chapters of this thesis.

(c) ***Compton (Incoherent) Scattering:*** Also known as inelastic scattering is an interaction between an x-ray photon and electron in the atom of a material the photon is incident on. The interaction results in the transfer of part of the photon's energy to the electron, ejection of the electron (Compton electron), and a change on the part of the x-ray photon (Compton scattered photon). Note, the Compton scattered photon energy is less than that of the incident photon. Also, the sum of the Compton scattered photon energy and kinetic energy of the Compton electron is equal to the incident photon energy. Compared to Elastic scattering, Compton scattering is similar to photoelectric absorption in the following aspects: (1) the interaction is between an x-ray photon and electron though in Compton scattering the electron is a loosely bound electron (or free electron) while in photoelectric absorption the electron is tightly bound; and (2) the electron the x-ray photons interact with is ejected. A loosely bound or free electron is an electron with a binding energy that is very small in comparison with the x-ay photon energy. The probability that an incident x-ray photon will be Compton scattered is nearly independent of the material's atomic number Z and weakly dependent on the incident photon energy.

There are other x-ray interactions such as pair production and photonuclear effects but these are not important in the diagnostic energy range. The energy range of photons used in this

research is 20 to 50 keV, which falls within the diagnostic energy range. The above described possible interactions of photon with materials contribute to x-ray photon attenuation by materials, for photons with energies within the diagnostic energy range [1, 2, 33]. Thus, the mass (μ/ρ) attenuation coefficients will be

$$\mu/\rho = (\mu/\rho)_{Photoelectric} + (\mu/\rho)_{Elastic} + (\mu/\rho)_{Compton} \quad (2.10)$$

2.3 Diffraction of X rays by Perfect Crystals

At synchrotron facilities, different types of optical devices such as monochromators, mirrors, and refractive lenses have been developed for reflecting, monochromatizing, and focusing of SR. But in the x-ray region of SR, effective reflection, monochromatization and focusing can only be achieved by diffraction with crystals or artificial multilayer structures [34, 35]. The optical device used in this research is a crystal, hence the reason for considering diffraction of x-rays by crystals. A crystal is any two- or three- dimensional solid made up of atoms, ions or molecules that are arranged in a periodic pattern. Solids without this periodic arrangement are called non-crystalline (amorphous) solids [27, 31, 36]. The term "perfect" crystal is used if the periodicity is maintained in both the x and y or x, y and z directions for a two- or three- dimensional crystal, respectively [27]. Otherwise, the crystal is said to be imperfect or mosaic [37]. Perfect crystals are used in x-ray imaging primarily as a result of advances in preparing materials for the semiconductor industry. They [33]: (1) act as very narrow windows and preserve the coherence of x-ray beam; (2) can be used for separation of the scattering components of x-ray beam; and (3) for analysis of the propagation direction and phase distribution of the transmitted x-ray beam. Perfect crystals became available in the late 1950s. The maturity of perfect-crystal x-ray optics and crystal-growth technology is said to have been influenced by the birth of x-ray SR sources [37].

The diffraction of x-rays by crystals was discovered as far back as 1912, and it was this discovery that enabled the atomic structures of crystalline materials to be determined [28, 37, 38]. The rationale behind the use of x-rays in analyzing the structures of crystals is that the wavelengths of x-rays are on the same order of magnitude as the atomic spacings (lattice constants) of crystals [28, 31]. Thus, crystals are used as fine gratings for diffraction of x-rays. In describing diffraction of x-rays by a crystal, two terms associated with the crystal are commonly used, the crystal planes involved and their spacing. Crystal planes are denoted by (hkl) and their

corresponding spacing by d_{khl}, where hkl are integers called Miller indices. All equivalent (i.e., same orientation) and parallel planes are represented by the same set of Miller indices. A diffracted x-ray beam is due to scattering by the atoms from a number of equivalent parallel planes [31]. For a crystal to diffract x-rays, the Bragg's condition- a condition for constructive interference of the x-ray scattered by the crystal's atoms, must be satisfied [31]:

$$n\lambda = 2dsin\,\theta \tag{2.11a}$$

$$\lambda = 2\frac{d}{n}sin\,\theta \tag{2.11b}$$

$$\lambda = 2d_{hkl}sin\,\theta \tag{2.11c}$$

where λ is the wavelength of the x-ray, θ is the angle of incidence of the x-ray to the lattice planes with spacing, *d*, of the crystal, d_{hkl} is the distance between the crystal planes (hkl) or reflection planes from which the diffraction (reflection) occur, and n is an integer referred to as the order of diffraction (reflection). Equation (2.11) is also known as the Bragg's Law. Equation (2.11a) shows for a single d spacing the effect of diffraction orders, n, from that spacing. Equation (2.11b) is the same as eqn. (2.11a), but shows that higher orders (n>1) can be thought of as diffraction from fractions of the original d-spacing. Equation (2.11c) is a generalization of Bragg's Law that accounts for the three-dimensional periodicity of a crystal and also includes the "diffraction order" dependence. For example Silicon $d_{440} = \frac{1}{2}d_{220}$. When a white beam ("white radiation"), i.e., x-rays that have a range of different wavelengths, is incident on a crystal, many different diffractions (reflections) are observed.

There are two theories that have been formulated to describe the diffraction of x-rays by crystals, the kinematical and dynamical theories [25]. The kinematic theory (simplified theory and applicable to imperfect crystals) assumes that the incident x-ray wave suffers no change when it enters the crystal medium whereas in the dynamical theory (general theory and applicable to perfect crystals), normal absorption as well as the interaction between incident and scattered radiation in the crystal medium are taken into account [39].

CHAPTER 3

BENT LAUE CRYSTAL OPTICS

Crystals are widely used as x-ray optical elements mostly as monochromators. The three commercially available materials for crystal x-ray monochromators are primarily diamond, silicon (Si) and germanium [37]. At high x-ray energies used for biomedical and medical imaging, Si is commonly used because of its favourable properties: good thermal and mechanical properties [37, 40, 41], and its availability as a perfect or dislocation free crystal of large size. This is due to, in large part, the drive for the semiconductor industry to develop better materials for electronic chips and sensors. The term Laue crystal (Laue case crystal or Laue diffraction geometry) is used when the diffracted x-ray beam exits the crystal from a surface opposite to that which the x-ray beam is incident upon. If the diffracted beam exits the crystal from the same surface that beam is incident upon, the term Bragg crystal (Bragg case crystal or Bragg diffraction geometry) is used [37]. A Laue or Bragg crystal can be bent or flat. Compared to flat crystals, elastically bent perfect crystals have high reflectivities, behave uniformly over large surface areas, and their energy bandpass can be adjusted [42]. The use of bent crystal optics has been attributed to the many breakthroughs in research with high energy synchrotron radiation [43]. For the diffraction of x-rays with a single bent Laue crystal, the two possible geometries that can be used are the non-dispersive (Cauchois) and dispersive (polychromatic) geometries [44]. As shown in figure 3.1 for a cylindrically bent crystal, in the focusing geometry, the convex side of the bent crystal faces the x-ray source whereas in the non-focusing geometry, the concave side faces the source. A two or more bent Laue crystal system involves a combination of these two geometries. Depending on the type of application, bent Laue crystals have certain advantages over bent Bragg crystals. Some of these advantages are [43, 45-47]: high diffraction efficiency; enhanced reflectivity width; effects of geometrical aberrations are smaller; thickness and asymmetric cut of crystal can be optimized for flux and energy resolution; and when a thin crystal is used, the absorption due to transmission in the crystals is minimized because the incidence angle of the x-rays is almost normal.

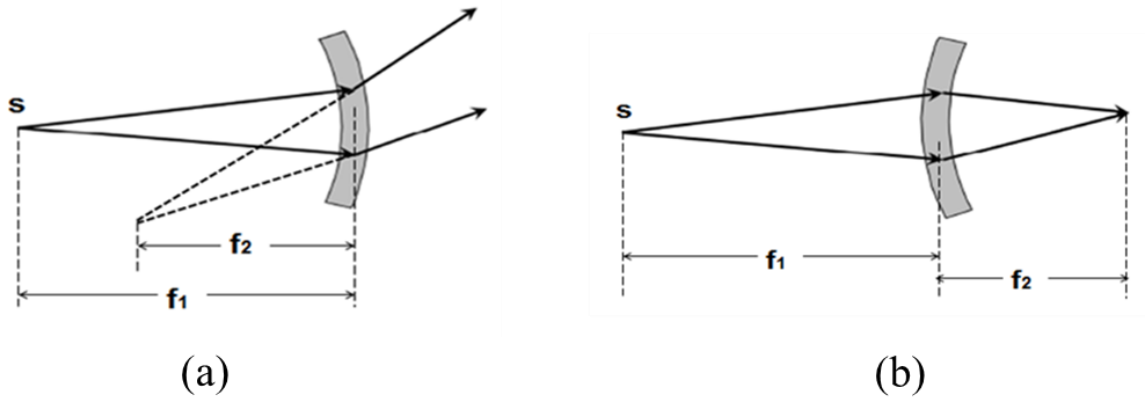

Figure 3.1: A cylindrically bent Laue crystal in (a) Cauchois, and (b) polychromatic geometries. S is the radiation source; f_1 and f_2 are the distances from the crystal to source and focus, respectively. **Source**: Ref. [165].

Different methods of bending crystals have been developed. These methods can be grouped into mechanical and non-mechanical. The mechanical methods involve the use of external devices: some examples are four-bar bender, four-point bender, frame bender, and leaf-spring bender. A four-bar bender has four parallel bars (two inner bars and two outer bars) that are used for bending crystals. The crystal to be bent is usually in the form of a wafer, and can be circular or rectangular in shape. A picture of a four-bar bender with a circular Si crystal wafer is shown in figure 3.2. The ends of the four bars are held by a compression spring that can be controlled manually with a micrometer screw or a piezo-driven micrometer head. Bending of a crystal is achieved by displacing the two inner bars while the two outer bars are kept fixed [48, 49].

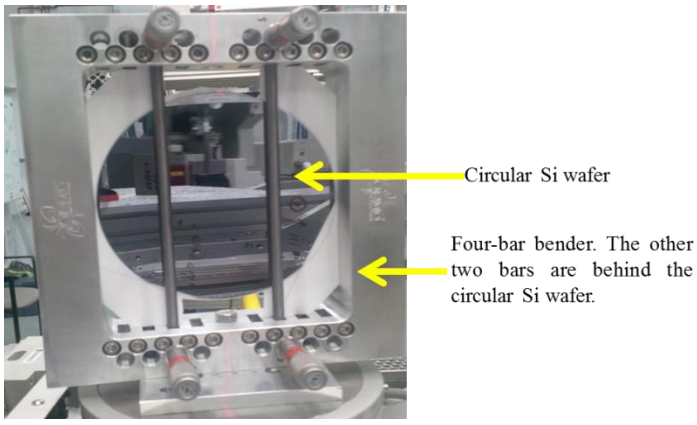

Figure 3.2: A four-bar bender with a circular Si wafer in it. **Source**: Ref. [177].

With a four-bar bender, the radius of the bent crystal can be varied. A main advantage of a four-bar bender is that a symmetric bend can be created [49]. Unlike a four-bar bender, bending in a four-point bender (figure 3.3) is achieved when the outer flanges of a crystal are pressed against the crystal face by means of two separate screws [50]. A frame bender (figure 3.4) is simply a metal frame that has been machined to the required bending radius with an opening to allow the passage of x-rays. A crystal wafer attached to the frame acquires the bending radius of the frame bender. The metal frame commonly used is aluminum because of its good thermal conductivity, light weight, ease of machinability and low cost. The disadvantage of a frame bender is that the bending radius is fixed. Thus, if three bending radii, for example, are needed, three separate frames will be required, which increases cost. But once a crystal is mounted and performs well, there should never be a need to touch it again, this improves repeatability. In a leaf-spring bender (figure 3.5), the force required to bend the crystal is applied to the leaf-spring. There are variations in the design of a leaf-spring bender [41, 49]. The bend produced by a leaf-spring is said to be asymmetric since force is applied to only one side of a crystal [49]. The leaf-spring can be made of steel [51].

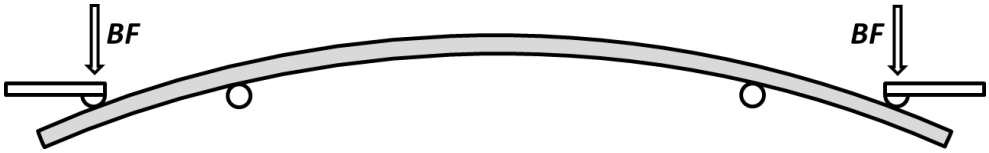

Figure 3.3: Schematic top view of a four-point bender. Bending forces (BF) are applied at the points shown. **Source:** Ref. [50], reproduced with permission of the International Union of Crystallography.

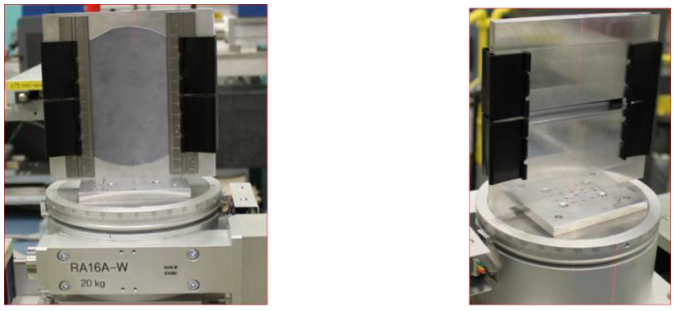

Figure 3.4: A frame bender (bent radius 1.0 m) showing a Si crystal wafer bonded to it (a) upstream view with respect to the x-ray source and (b) downstream view showing the opening through which the x-ray passes.

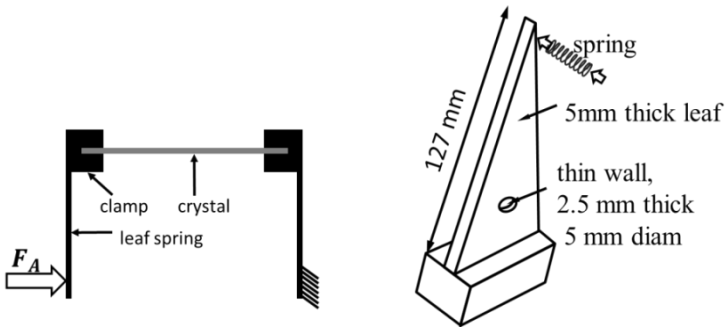

Figure 3.5: Different designs of a leaf-spring bender: (a) Crystal clamped at both sides. Though both sides of the crystal are mounted on the leaf spring, to bend the crystal, force, F_A, is applied to only one leaf spring while the other remained fixed; (b) Crystal clamped at one side-the base while leaf springs are attached to its upper part. The pushing of the free ends of the springs introduces a bending moment that causes the thin central part of the crystal to curve to cylindrical shape. **Sources:** (a) Ref [49], reproduced with permission of IOP Science, (b) Ref. [41], reproduced with permission of the International Union of Crystallography.

Superficial indentations, use of mixed crystals with a composition gradient, application of a thermal gradient, and carbon fiber deposition are some of the methods of bending a crystal non-mechanically. The method of superficial indentations is claimed to have been discovered in 70-GeV channeling experiments, [52] and has been proven to be a good method of bending crystal without the need for an external device [52-54]. Bending of crystal by superficial indentations (figure 3.6) involves the use of a semiconductor dicer to groove the surface of a crystal, resulting in an irreversible compression of the material between the grooves (i.e., beneath and beside the indentations); the grooves act like a tensile film causing the whole crystal to bend [53, 54].

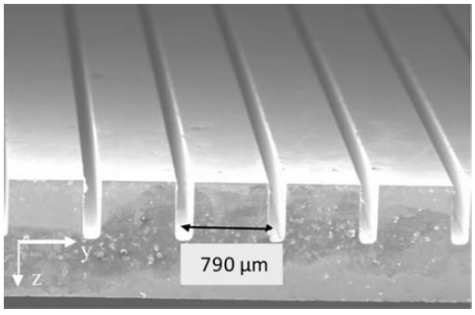

Figure 3.6: Side view of a Si wafer with a series of indentations as taken by a scanning microscope. The black arrow indicates the pitch of the grooves; depth of grooves is 500 µm and bending radii from the y and x- profile measurements are 77.50 m and 330 m, respectively. **Source:** Ref. [54].

The bending of crystals via mixed crystals with a composition gradient involves a two-component crystal, usually Si-Ge, grown such that the relative concentration of the two components changes as the crystal is grown [55]. The curvature induced is caused by a change in the spacing between the crystal planes as the percentage of Ge changes with position in the crystal [55, 56]. Among the known techniques for growing $Si_{-x}Ge_x$ single crystals, the Czochralski (CZ) technique is considered the most convenient for growing single crystals of large diameters [57]. Bending of a crystal by the application of a thermal gradient, as implied by the name, involves applying different amount of heat to the surfaces of a crystal. For an example, the application of thermal gradients (figure 3.7) perpendicular to the crystalline planes of a 1-cm cube Si crystal used in a diffraction process, and varied between 0.0 and 114°C/cm, resulted in radii of curvature from infinity down to 40 m [56]. The curvature of the planes is reversed depending on the hotness of the top of the cube relative to the bottom. The radius R of curvature of the crystal planes induced, and the amount ($\Delta\theta$) of curvature of the crystal planes seen by the x-ray beam are given by eqns. 3.1 and 3.2, respectively [56].

$$R\ (cm) = \frac{1}{\alpha \Delta T}, \tag{3.1}$$

where α is the coefficient of thermal expansion, and ΔT is the thermal gradient in units of °C/cm.

$$\Delta\theta\ (arc\ sec) = \left(\frac{L}{R}\right)(2.06\ \times 10^5), \tag{3.2}$$

where L is the length of the crystal in the direction of the incident x-ray and the numerical constant 2.06 x 10^5 is the number of arc sec in a radian.

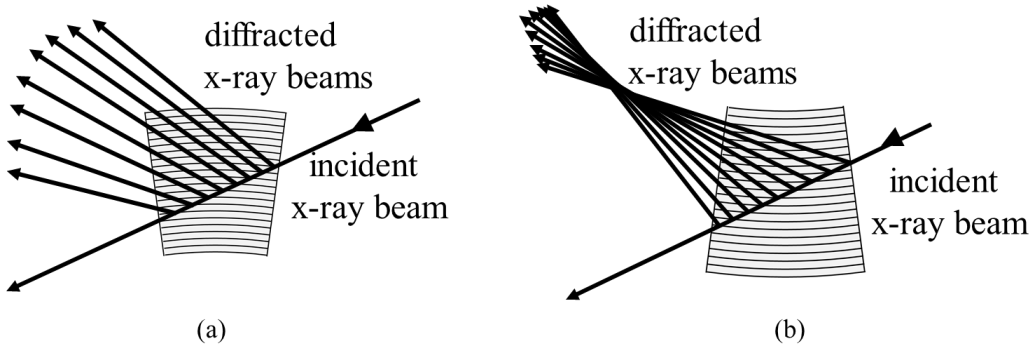

Figure 3.7: Thermal gradient crystals, showing curved crystal planes and diffracted x-rays for the (a) "hot top" case and (b) "cold top" case, exaggerated to emphasize the effect. **Source:** Ref. [56].

Carbon fiber deposition is an innovative method proposed by Riccardo et al. for the production of thick self-standing bent crystals[58]. By using this method, which involves depositing a thick film of commercially available carbon fibers on a crystal, they were able to produce self-standing 5 mm thick bent Si crystals with a radius of 30 m. According to them, this method is expected to work for other types of crystals like germanium, gallium arsenide, and copper.

With respect to crystals that are bent, mostly mechanically, the issue of "beam smiling" has been raised-an effect considered to be an intrinsic characteristic of a bent Laue crystal due to anticlastic bending [44]. "Beam smiling", which occurs when a wide fan-shaped beam is diffracted by a bent crystal, means that the profile of the diffracted beam does not appear as a straight line, but as a line with its both ends curved up or down [44]. Some of the solutions to beam-smiling problem are: (1) the crystal width should be much larger than the beam width; (2) the crystal height should be comparable to the crystal width; (3) the bending mechanism should allow differential bending and twist removal in order to compensate for the non-uniform surface slope of the crystal; and use of ribbed crystals [44]. Another reported effect that results when a crystal is bent by applying external forces is the 'quasi-mosaic' effect-the generation of a secondary curvature (quasi-mosaic curvature) within the crystal, and is attributed to the anisotropic nature of crystals [59-62]. Crystals that exhibit the 'quasi-mosaic' effect are called quasi-mosaic (QM) crystals, that is, bent crystals that have two curvatures of two orthogonal crystallographic planes [62].

Crystals, mostly in the form of wafers, have been bent into various shapes-cylinder, sphere, cone, ellipsoid, and log spiral, the most common being cylinder. An interesting fact about a logarithmic spiral shaped bent Laue crystal is that the crystal presents the same angle of incidence to the beam emanating from a point source, and as a result the Bragg condition is satisfied over a large angle [63]. The logarithmic spiral shape is given in polar coordinates by eqn. 3.3 [64, 65], and its diagram shown in figure 3.8.

$$r = \rho_0 cos\,(\chi - \theta_B) exp[tan\,(\chi - \theta_B)\theta], \tag{3.3}$$

where ρ_0 is average bending defined as bending radius at the center of the crystal ($\theta = 0$), θ_B is the Bragg angle, and χ is the crystal asymmetry angle.

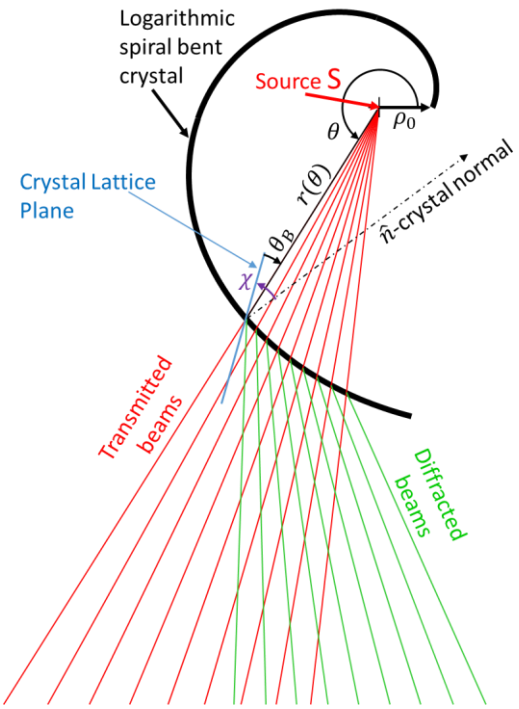

Figure 3.8: Logarithmic spiral bent Laue crystal. The source point is marked S and is the origin of the radius, r, in equation 3.3. The lattice plane is marked in blue and the asymmetry angle χ of the lattice planes are measured from the crystal surface normal. The rays from the source make the same angle, θ_B, to the lattice planes in the crystal. The diffracted and transmitted beams are shown in green and red, respectively.

Generally, two main types of bending can be distinguished-meridional and sagittal bending. A crystal is said to be bent meridionally if the bending plane is the same as the diffraction plane while for a sagittally bent crystal, the bending plane is perpendicular to the plane of diffraction [66]. A sagittally bent Laue crystal is accompanied by anticlastic bending in the meridional plane [67]. Although anticlastic bending in a bent crystal is disadvantageous, Zhong et al. [66, 68] took advantage of it in a sagittal bent Laue crystal (used in the focusing mode) to realize the inverse-Cauchois geometry in the meridional plane. This resulted in a better energy resolution and a higher photon flux compared to that achievable from a sagittal focusing Bragg crystal.

3.1 Bent Crystal Theories

A bent (curved) crystal is considered distorted and the propagation of x-rays in it is treated differently, depending on the level of its distortion. In this section, some of the theories and models on bent crystal are presented, with emphasis on bent Laue crystals.

3.1.1 Propagation of x rays in bent crystals

Several studies have been undertaken on the propagation (diffraction) of x-rays in bent crystals. Some of the theories that have been developed to describe the propagation of x-rays in bent crystals are: (1) Penning and Polder geometric optics theory; (2) Kato geometric optics theory; and (3) the wave-optical theory of Takagi [35, 69]. The propagation of x-rays in distorted crystals has been shown to be dependent on the level of distortion of reflecting planes in crystals, and is characterized by the parameter, β, the strain gradient [69, 70]. The β parameter, introduced by Penning and Polder and Kato in their geometrical optics theories, is defined as [69]

$$\beta = \left[\frac{\Lambda_L}{cos^2(\theta_B)}\right]\left[\frac{\partial^2(\boldsymbol{h}.\boldsymbol{u})}{\partial s_0 \partial s_h}\right], \tag{3.4}$$

where **u** is the displacement vector of the atom from its ideal position, **h** the reciprocal-lattice vector, s_0 and s_h the coordinates along the directions of the incident and the reflected beam, respectively, θ_B the Bragg angle and Λ_L the inverse of the diameter of the dispersion surface. For the symmetrical Laue case, Λ_L is equal to the extinction length:

$$\Lambda_L = \frac{\pi V cos(\theta_B)}{r_e \lambda |C| \sqrt{(F_h F_{\bar{h}})}} \tag{3.5}$$

V is the volume of the crystal unit cell, F_h and $F_{\bar{h}}$ are the structure factors for reflections *h* and – *h* (or $\bar{h}$), C represents the polarization factor, λ the wavelength of the x-rays, and r_e the classical electron radius.

It has been shown that the geometric optics theory only holds for weakly bent crystals [70] where

$$\beta \ll \frac{1}{\Lambda_L} \; or \; \beta \Lambda_L \ll 1 \, . \tag{3.6}$$

In weakly bent crystals, the variation of the angle of incidence on the reflecting planes due to the distortion over a distance equal to the extinction length Λ_L is said to be much smaller than the width of the reflection profile (Darwin width). But the opposite is the case for strongly bent crystals, and thus, $\beta\Lambda_L >> 1$. This led to the introduction of the concept of creation of new wavefields in the crystals; a concept accounted for in the wave-optical theory but not in the geometric optics theory [35, 70]. Numerical simulations based on the wave-optical theory show that when $|\beta| > \pi/2\Lambda_L$, a new wave field is created in the region of the crystal where the Poynting vector is parallel to the reflecting planes; the creation of new wavefields reduces the

reflected intensity [69]. Also, when the changes in the orientation of the Bragg planes over the extinction length equals or is more than the Darwin width of the reflection, the crystal starts behaving like an imperfect crystal obeying the kinematical diffraction theory [71, 72].

3.1.2 Intensity and reflectivity of x rays by bent crystals

The ratio of the diffracted beam intensity to the incident beam intensity by a crystal is termed its reflectivity [73]. The dynamical and kinematical theories of x-ray diffraction are the theories generally used to account for intensities observed in x-ray diffraction studies. The dynamical theory considers the interaction of the x-rays in the crystal while the kinematical theory does not [74]. For weakly and strongly bent symmetric Laue crystal onto which a quasi-plane wave is incident, Malgrange [70] showed that the reflected and transmitted intensities, I_R and I_T, respectively, are

$$for\ \beta\lambda_L \ll 1:$$

$$I_R = I_0[\exp(-\mu t)]\left[1 - \exp[-\left(\frac{\pi^2}{\beta\Lambda_L}\right)]\right], \quad I_T = I_0\,[\exp(-\mu t)]\exp[-\left(\frac{\pi^2}{\beta\Lambda_L}\right)], \tag{3.7}$$

$$for\ \beta\lambda_L \gg 1:$$

$$I_R = I_0\,[\exp(-\mu t)]\left(\frac{\pi^2}{\beta\Lambda_L}\right),\ I_T = I_0\,[\exp(-\mu t)]\left(1 - \frac{\pi^2}{\beta\Lambda_L}\right). \tag{3.8}$$

I_0 is the incident intensity, μ the absorption coefficient and t the thickness of the crystal. For each of the above two cases, the integrated reflected (diffracted) intensity I_R^{int} is given by

$$I_R^{int} = I_R\omega, \tag{3.9}$$

where ω, the width of the rocking curve, is related to t, β, and δ (Darwin width) by

$$\omega = \frac{\beta t\delta}{2}. \tag{3.10}$$

The x-ray reflectivity of bent crystals can be calculated using approximate models; two such models are the multi-lamella (lamellar) and the Penning and Polder models [75, 76]. Both models are based on the dynamical theory of diffraction [77, 78]. The lamellar model was introduced by J.E White [79] and is used for calculating the reflectivity curves of x-rays in synchrotron radiation applications [43]. In the lamellar model, a curved crystal is approximated by a set of perfect-crystal lamellae which have a gradually increasing tilt angle corresponding to the bend of the crystal. The reflectivity of the crystal is the sum of partial reflections in the

lamellae. The Darwin width of the reflection under investigation is commonly used as the thickness between two successive lamellae [79]. The Penning Polder model assumes that a distorted crystal can be divided into smaller regions where the propagation of wavefields can be described locally in terms of the dynamical theory of perfect crystals. In the model, propagation of x-ray wave fields in a distorted crystal is in analogy to the propagation of a beam of light in an inhomogeneous medium using the concept of geometrical optics [80]. Based on the lamellar and the Penning and Polder models, several computer programs have been developed and used for reflectivity curves calculations [76]. For the calculation of Laue crystal reflective curves, only the Penning and Polder model can be applied, the computer programs PEPO [80] and XCRYSTAL [76] can be used for this purpose because they are developed from the Penning and Polder model. One major difference between PEPO and XCRYSTAL is that PEPO is used for meridionally bent cylindrical crystals while XCRYSTAL can be used for crystal bent in both sagittal and meridional planes. Zhong et al. [78] developed a lamella model for calculating the reflectivity curves of sagittally bent Laue crystal because the lamella model for calculating meridionally bent crystals cannot be used for sagittally bent Laue crystals. From calculations and measurements, the reflective curve of a bent Laue crystal: is almost flat-topped; has a large width, the maximum reflectivity may be close to unity; and can be controlled by the choice of thickness, asymmetry angle, and bent radius [41, 43, 44, 46, 56, 78, 79].

3.1.3 Focusing of x rays by bent crystals

Focusing of x-rays by a bent crystal is based on a change in the Bragg plane orientation [35]. A bent crystal acts a monochromator when the x-ray source and focus (image) are located on the Rowland circle, and as a polychromator when the source is outside the Rowland circle [81]. The Rowland circle is the focusing circle, its diameter is the bending radius of the crystal [75]. A bent Laue crystal has two foci-the geometric (monochromatic) and single-ray (polychromatic) foci. The single-ray focus, which can be real or virtual, does not generally coincide with the geometric focus, resulting in an effect called ‘crystal depth broadening’- the broadening of the focus obtained [35, 40]. The focus broadening, caused by the intrinsic Darwin width and the spread of the beam in the Borrmann triangle (fan) is considered as the main limitation of the Laue geometry for achieving a small focus size [47, 82]. It has been established that focus broadening can be reduced by an appropriate choice of the crystal asymmetry angle, thickness, and bending

radius [35, 47, 82, 83]. Meridional focusing (vertically or horizontally) and sagittal focusing of x-rays have been achieved with bent Laue crystals. An example of focusing of x-rays in the meridional plane using a cylindrically bent Laue crystal is shown in figure 3.9 [84]. In this case, the x-ray source is located on the convex side of the crystal at a distance F_1 from the crystal while the diffracted beam is focused at a distance F_2 from the crystal on the concave side. The finite opening angle of the incident radiation is h_1/F_1; h_1 is the beam height. The focal distance F_2, of the geometrical focus is given by

$$F_2 = \frac{F_1 \rho \cos(\chi - \theta)}{2F_1 + \rho \cos(\chi + \theta)}, \tag{3.11}$$

where θ is the angle of diffraction, r the bent radius, and χ the asymmetry angle. The single-ray focus, F, is given by [84, 85]

$$F = \frac{\rho \sin(2\theta)}{2 \sin(\chi + \theta)}. \tag{3.12}$$

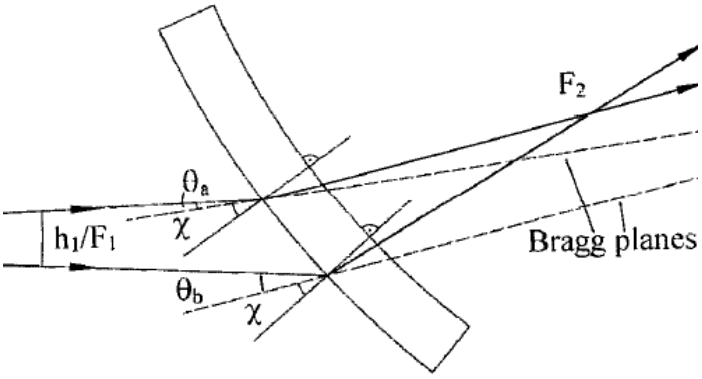

(a)

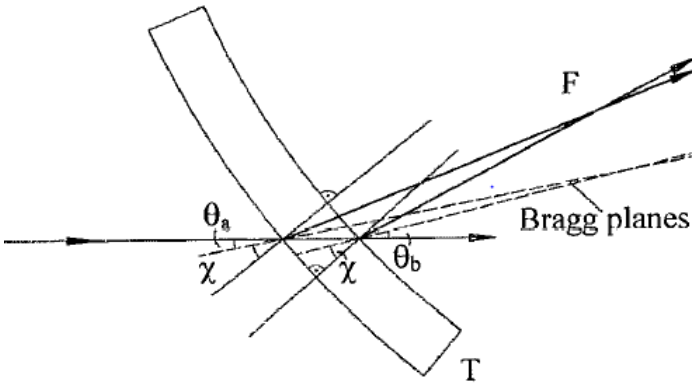

(b)

Figure 3.9: (a) Geometric focusing of x-rays and (b) single ray focusing by bent Laue crystal. **Source:** Ref. [84].

The corresponding energy bandwidth of the diffracted beam, that is, the energy dispersion of the beam diffracted in the bent Laue crystal is:

$$\frac{\Delta E}{E} = \cot(\theta) h_1 \left[\frac{1}{F_1} + \frac{1}{\rho \cos(\chi + \theta)}\right] \tag{3.13}$$

If the divergence, i.e., full-width-half-maximum (FWHM) of the incident beam on the bent Laue crystal, is ε, the energy bandwidth of the diffracted beam can also be computed using [82]:

$$\frac{\Delta E}{E} = \varepsilon \cot\theta \left[\frac{1+ F_1}{\rho \cos(\chi + \theta)}\right] \tag{3.14}$$

Assuming the crystal of thickness T is elastically isotropic with a Poisson ratio,ν, the change in the Bragg angle due to bending, δθ, is [86]:

$$\delta\theta = \frac{T}{\rho}\left[tan(\chi + \theta) + \frac{1}{2}(1 + \nu)\sin 2\chi - \tan\theta(cos^2\chi - \nu sin^2\chi)\right] \tag{3.15}$$

where the bending radius ρ is given by:

$$\rho = \frac{2F_1F_2}{F_1 cos(\chi - \theta) - F_2 cos(\chi + \theta)} \tag{3.16}$$

Mercedes et al. [87] argued that the single-ray focus, F, as given by eqn. 3.12 does not take into consideration the curvature of the diffraction planes induced by the elastic deformity of the crystal. To account for this, they derived the single-ray focus equation as

$$F = \pm\frac{R\, sin\, 2\theta_B}{2\, sin(\chi \pm \theta_B) + (1+\nu)\, sin\, 2\chi\, cos(\chi \pm \theta_B)} \tag{3.17}$$

where θ_B is the angle of diffraction (Bragg angle) and F takes either positive or negative sign if real or virtual, respectively. Also ($\chi+\theta_B$), i.e., "upper case" is used when the x-ray beam does not lie between the crystal's surface normal and the Bragg plane as in figure 3.9, and ($\chi-\theta_B$), the "lower case" used if otherwise. Equation 3.17 agrees with the equation earlier derived by Sutter et al. [88] for the "lower case".

By using the anticlastic bending in a sagittally asymmetric bent Laue crystal, Zhong et al. [67] developed a novel method for sagittal focusing of x-rays horizontally. Based on their method as shown in figure 3.10, the distance from the x-ray source to the crystal (F_1), the distance from the crystal to the focal point (F_2), the Bragg angle (θ_B) of the reflection, asymmetry angle (χ), and the radius of the sagittal bending are related by

$$\frac{1}{F_1} + \frac{1}{F_2} = \frac{2\, sin\theta_B\, sin\chi}{R_S} \tag{3.18}$$

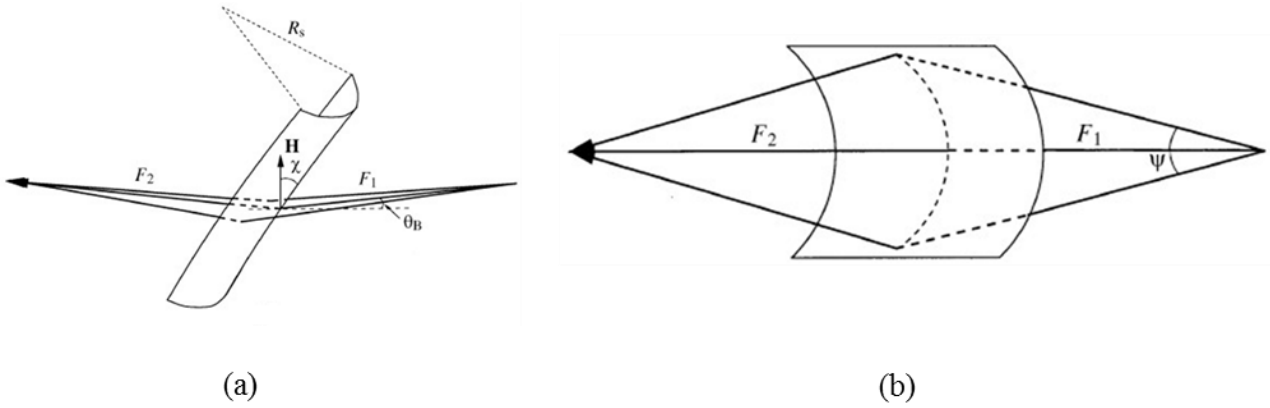

(a) (b)

Figure 3.10: Sagittal focusing of a diverging horizontal fan-shaped beam from a synchrotron x-ray source by a single crystal sagittally bent Laue crystal. F_1 and F_2 are the distances from the source to crystal and crystal to focal point, respectively, (a) Side view, and (b) Top view. **Source:** Ref. [67], reproduced with permission of the International Union of Crystallography.

The sagittal focal length (F_s) is:

$$F_s = \frac{\pm R_s}{2\, sin\theta_B\, sin\chi} \tag{3.19}$$

where F_s is positive (upper sign) if the diffraction vector (**H**) is on the same side of the crystal as the center of the sagittal bending, that is, **H** is on the concave side of the sagittal bent crystal. If **H** is on the convex side of the crystal, causing further divergence of the horizontal x-rays, as in the case shown in figure 3.10, F_s is negative (lower sign). From eqn. 3.19 above, F_s is infinite when χ is zero, implying that a symmetrical Laue crystal cannot focus sagittally. The energy bandwidth of the diffracted x-rays is

$$\frac{\Delta E}{E} = \frac{\left[\Delta\theta^2 + \omega_0^2 + \left(\frac{\sigma_S}{F_1}\right)^2\right]^{\frac{1}{2}}}{\tan\theta_B} \tag{3.20}$$

where $\Delta\theta$ is the variation of the angle of incidence along the surface of the crystal due to the different vertical parts of the beam meeting the crystal at different angles, ω_0 intrinsic angular acceptance of the crystal, and σ_s/F_1 is the angular aperture of the source size, $\sigma_{s,}$ in the vertical plane.

$$\Delta\theta = \varphi_v\left[1 - \frac{F_1}{R_m} cos(\chi \pm \theta_B)\right] \tag{3.21}$$

where φ_v is the vertical divergence of the incident white beam and R_m is the anticlastic bending radius in the meridional plane.

3.2 Applications of Bent Laue Crystals

Due to the unique properties of bent Laue crystals, different techniques involving the use of bent Laue crystals have led to the development of new systems, and improvement of existing systems for various applications. Some of examples of these applications are presented in this section; the focus is on applications with respect to synchrotron sources.

3.2.1 K-edge subtraction imaging

K-edge subtraction (KES) imaging is a medical imaging modality that has been significantly improved because of the use of bent Laue crystals. The development of KES imaging dates back to the work of Bertil in 1953 on the possibility of using monochromatic x-rays (then called roentgen rays) to increase the contrast obtained in a radiograph [89]. Bertil used the term 'dichromatic absorption radiography' (abbreviated Dichromography) which meant "the technique of using the differences of absorption of two or several monochromatic roentgen rays or rays of different wave-length distributions for the production of a picture showing differences in absorption or for showing the distribution and/or the concentration of an element in an object." One of the ways of implementing the technique that Bertil considered was 'Edge dichromography', which involved determining the concentration of an element by measuring the difference in absorption of two wavelengths lying close to but on opposite sides of the absorption edge of the element. It is interesting to note that one of the means of producing monochromatic radiation considered then was the diffraction of a polychromatic spectrum by a crystal. Edge dichromography is what is known today as KES imaging. In KES imaging, two images of a subject are taken above and below the K-edge of an element that has been administered to the subject; the logarithmic subtraction of these two images suppresses all absorbing structures in the subject excepting structures filled with the element thereby enhancing the contrast of such structures [84, 90].

At synchrotron facilities, KES imaging systems employing a single or double bent Laue crystal monochromator in the focusing geometry have been used for coronary angiography, [84-86, 91-94] mammography, [95] and bronchial imaging [96]. These monochromators provide the two x-ray energies needed for KES imaging, which eliminates motion artifacts in the image because the beam energies (above and below the K-edge) used are prepared simultaneously. At the National Synchrotron Light Source (NSLS) biomedical beamline and the European

Synchrotron Radiation Facility (ESRF) ID 17 beamline, a single bent Laue crystal Si (111) monochromator and a splitter are used to prepare the two x-ray beams [85, 97]. The conventional (dual-energy or dual-beam) KES imaging setup applied to lung imaging at the European Synchrotron Radiation Facility (ESRF) ID 17 beamline is shown in figure 3.11 [97].

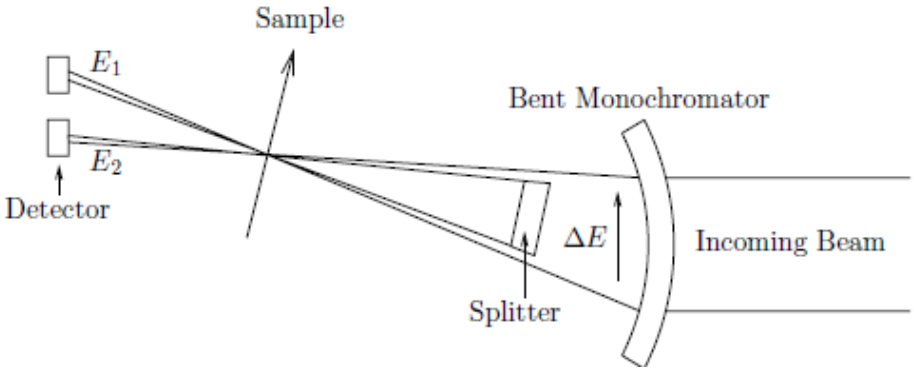

Figure 3.11: A schematic picture of the monochromator and detector setup in dual-beam KES imaging at ESRF ID 17 beamline. **Source:** Ref. [97].

Zhu et al. [90] developed a novel and 'simple' method of performing KES imaging at the BMIT-BM beamline, called spectral-KES. The Spectral-KES system also uses a single bent crystal (Si) wafer in the Laue geometry but without a beam splitter, and has several advantages over the conventional KES. One aspect of this approach is the choice of asymmetry angle in the monochromator which dramatically improves the energy dispersive properties. The part of the diffracted beam (angular part or spatial part at the detector) which is at or near the edge is quite small, this makes the use of a splitter practically impossible and thus, unnecessary. The photon flux available for use in spectral-KES system is higher compared to dual-energy KES system because a splitter is not used to divide the beam. Spectral-KES can be performed in both projection and CT modes [90, 98]. A schematic diagram of the spectral-KES system is shown in figure 3.12.

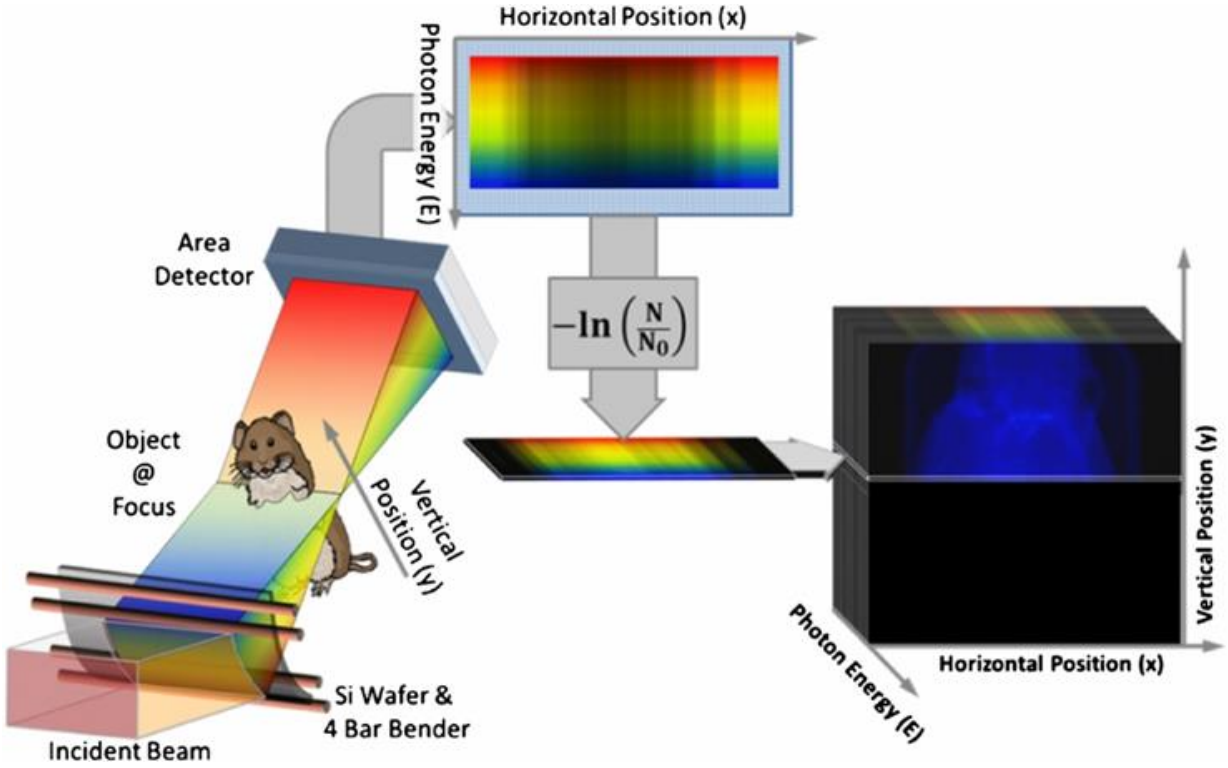

Figure 3.12: A schematic diagram of spectral-KES system. **Source:** Ref. [90].

3.2.2 X-ray computed tomography

X-ray computed tomography (CT) is a widely used method of obtaining cross sectional views of objects, and with SR sources, x-ray CT systems can be used to produce CT images more rapidly with better spatial resolution and reduced beam artifacts [99]. Ren et al. [48] developed a two-crystal bent Laue-Laue monochromator for multiple energy CT (MECT). The two crystals were Czochralski-grown Si <1,1,1>, thicknesses 0.7 and 1.4 mm with thick ribs on their upper and lower ends, and cylindrically bent with the axis of the cylinder parallel to a fan-shaped synchrotron x-ray beam. The two bent Laue crystals were used in the non-dispersive geometry. Before the development of this monochromator, a two-crystal flat Laue-Laue monochromator for their MECT program was used. A test they conducted with the two-crystal bent Laue-Laue monochromator at 42 and 108 keV showed about a 10-fold larger beam flux, about 5 times better stability, 10-fold less harmonic contamination, and a smaller bandwidth compared to their two-crystal flat Laue-Laue monochromator. Suortti et al. [81] also developed a two-crystal bent Laue-Laue monochromator in the non-dispersive geometry for CT studies but theirs operated at energy range of 18 to 90 keV.

3.2.3 X-ray absorption spectroscopy

X-ray absorption spectroscopy (XAS) is a tool commonly used for the investigation of local electronic and atomic structure in a sample [100]. Bent Laue crystals have been widely used, mostly as bent Laue analyzers (BLA), in various types of XAS including: x-ray absorption fine-structure (XAFS); extended x-ray absorption fine structure (EXAFS); and x-ray absorption near edge spectroscopy (XANES) [101-103]. An example of a BLA used in XAS is that designed by Zhong et al. [64, 65, 101, 103, 104] for XAFS of dilute samples in the 12-25 keV range. The BLA is made of a thin bent Laue crystal of logarithmic spiral shape held in a machined frame. The crystal is 200 microns thick, has an active area of 35 mm by 120 mm, covers a solid angle of 0.1 sr, and is used in the non-dispersing geometry. When used for measurements, Soller slits made of tin (Sn) foils are placed after the BLA to separate the diffracted and transmitted beams; the transmitted beam contains elastic scatter that can contaminate the data collected.

3.2.4 Harmonics selection and rejection

X-rays reflected by double crystal monochromators used at SR beamlines are contaminated with higher order reflections, that is higher energy x-rays, called harmonics. Since harmonics can be useful for experiments at higher energies like x-ray absorption fluorescence spectroscopy, Karanfil et al. [105] developed a 'beam cleaner' capable of selecting and rejecting harmonics. The first design of 'beam cleaner' developed was made of a cylindrically bent single Si (1, 1, 1) Laue crystal, and was used as a post-monochromator. The crystal was triangular in shape (0.2 mm thickness, 25 mm base and 70 mm height) and was bent using a leaf-spring bender. The beam cleaner was effectively used to reject the 2^{nd} harmonic (3x the fundamental energy) from a Si (1,1,1) monochromator, and could also reject the fundamental and other harmonics up to Si (9,9,9). The problem they had with the single crystal design was that the diffracted beam was deflected from the line of sight for most measurements. This led to the development of a double-crystal bent (cylindrically) Laue post-monochromator 'beam cleaner', which solved the problem; the double bent Laue crystal design also improved XAFS data quality under high harmonic conditions [46].

Apart from the above discussed applications, bent Laue crystals have been used in various other applications: high-energy phase contrast imaging [82]; Rayleigh-to-Compton CT

[106]; x-ray spectrometer for Compton profile measurements [107, 108]; focusing of high-energy x-rays [49]; and x-ray beam expander for biomedical imaging [87, 109].

CHAPTER 4

MULTIPLE ENERGY X-RAY IMAGING

X-ray imaging is a well-known method used for characterizing materials either quantitatively or qualitatively [110]. At different x-ray energies, there are distinctions in the attenuation of x-rays by materials, which help in materials characterization [5, 111]. But there is also the possibility that different materials can have the same attenuation property at a given x-ray energy [112]. In this case one cannot discriminate such materials unless multiple x-ray energies are used. For example: bone and iodine have the same linear attenuation coefficients when single-energy x-rays of about 100 keV are used [113]; iodine and barium have similar attenuation curves [4]; and the attenuation of a single-energy x-ray alone cannot distinguish between iron and calcium [114]. With the use of a single-energy x-ray beam, the ability to quantitatively differentiate soft tissues from other tissues without the administration of a contrast agent is a problem. This problem can be solved by using a multiple energy x-ray beam. Contrast agents are simply high atomic number elements used in imaging to enhance the differences among body tissues on diagnostic images based on variations in anatomy or physiopathology; they make one structure more visible than adjacent tissues [115]. Elements between iodine and bismuth on the periodic table of elements are generally considered as contrast agents [116]. As earlier stated in Chapter 1 of this thesis, multiple energy x-ray imaging (MEI), also referred to as spectral x-ray imaging, is the use of two (dual-energy) or more x-ray photon energies for imaging. In MEI systems, multiple energies can be achieved either at the source or detector level. MEI has found applications not only in the medical field but also in other fields as well. Some examples of the non-medical applications of MEI [8, 9, 112, 117] are: inspection of luggage and cargo for explosives and other contraband; and non-destructive testing - quality control of industrial products, radioactive materials control, and inspection of welded joints and connections of building construction, pipelines, etc. In the medical field, MEI has made it possible to: quantify the mass density of two or three materials in a mixture with known elemental composition [113]; quantify calcium, fat and water components with soft tissues [118]; remove tissue or bone signals from an image [119, 120]; eliminate or suppress beam-hardening artifacts [121, 122]; visualize and characterize vasculature in areas where the vessels traverse

soft tissue and are surrounded by bone [123]; and improves the detection of cancerous and pre-cancerous lesions [124].

A conventional x-ray source such as an x-ray tube used in the laboratory or in medical applications produces polychromatic or polyenergetic x-rays [125, 126]. The x-ray's energy spectrum is dependent on the applied voltage usually quoted in kVp, and the x-ray tube anode material [127]. For an applied kVp, the effective (average) energy is considered to be approximately one-third to one-half of the applied kVp [3, 111], and hence the use of the term 'single' energy [5, 128-130]**.** The effective energy of a polyenergetic x-ray beam gives an estimate of the x-ray beam penetration power as if it were a monoenergetic (monochromatic) beam [3]. Synchrotron sources also produce polychromatic x-rays, which can be easily monochromatized (made monoenergetic) using appropriate x-ray optics. As earlier stated, there is a long standing interest in multiple energy imaging using both conventional and synchrotron x-ray sources [12].

4.1 Multiple Energy Imaging Methods

4.1.1 Conventional x-ray source based methods

One area in which MEI has been significantly implemented using a conventional x-ray source is in the development of clinical dual-energy computed tomography (DECT) imaging systems. DECT is a medical imaging method that uses two data sets (low and high energy data sets) from the same anatomic location of a subject; the two data sets are usually acquired with two different kVp (80/100 and 140 kVp) [127]. Currently there are three main methods for achieving MEI (dual-energy) in commercially available clinical DECT systems, each unique to a particular vendor in the health industry. The methods are: rapid kVp switching (GE Healthcare, Milwaukee, WI, USA); use of energy sensitive double-layered detector (Philips Medical Systems, Cleveland, OH, USA); and dual x-ray source (Siemens Healthcare, Forchheim, Germany) [5, 127, 131]. In the 1980's Siemen Healthcare also had a fast kVp switching DECT system (Siemens SOMATOM DRH) in the market [132]. All the above mentioned methods depend on the detected energy spectrum to be adequately separated [131] . The dual x-ray source and rapid kVp switching methods may be referred to as source-based MEI because the spectral separation is done at the source, and the double-layered detector method, a detector-based MEI [116]. The rapid kVp switching and energy sensitive double-layered detector systems are

classified as single source DECT systems [133]. A DECT comparison study showed that dual source DECT had the best performance, followed by the rapid kVp switching and double-layered detector methods [132]. Brief descriptions of these three DECT methods are as follows.

***Rapid kVp switching*:** Also referred to as "Fast" kV or tube voltage switching, it involves the acquisition of low and high energy projections data by rapidly switching the kVp of the x-ray tube between nominally 80 kVp and 140 kVp from projection to projection [132, 134]. In the GE Healthcare DECT system (Discovery CT 750HD), schematic drawing shown in figure 4.1, the kVp switching is done in about 0.4 ms time interval, in the same gantry rotation [127].

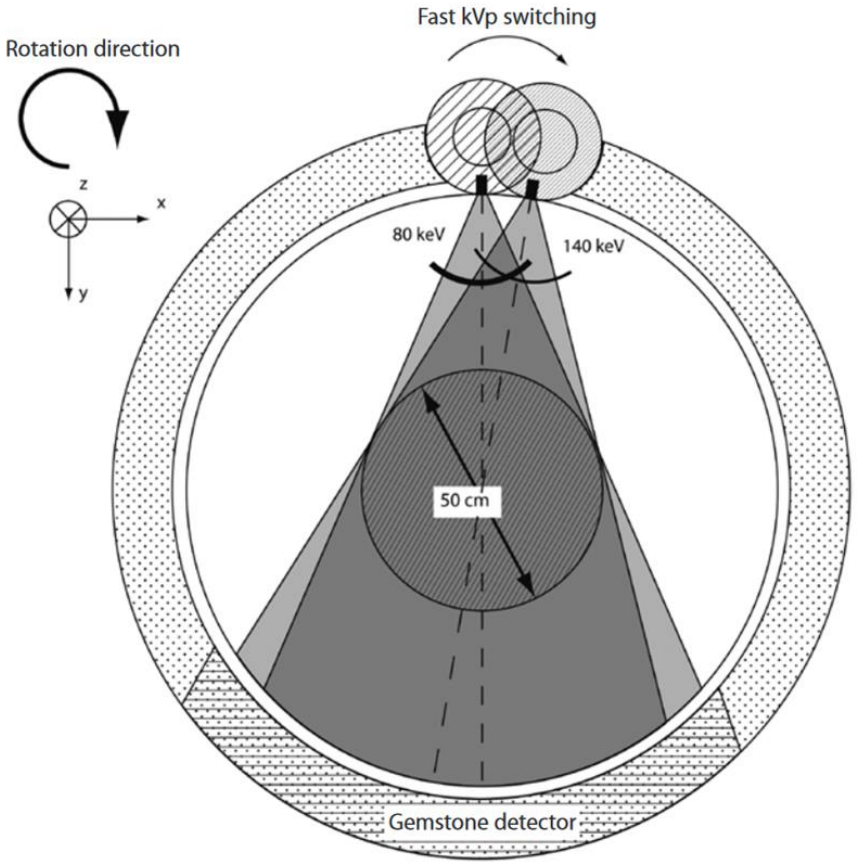

Figure 4.1: A schematic drawing of GE Healthcare fast kVp switching DECT scanner (Discovery 750HD). **Source:** Ref. [127].

The reported advantages of this method include [134, 135]:

(1) efficient in terms of energy separation though motion of the subject imaged is assumed negligible because of the quick succession at which the two data sets are acquired;

(2) can be implemented with a 2D detector which allows an acquisition rate that is dependent on the detector speed;
(3) material decomposition can be performed with the acquired raw data, which provides a decomposition that is free of beam hardening effects; and
(4) less sensitive to patient motion.

This method also has some disadvantages [5, 131-133, 135-137]:

(1) the maximum field of view that can be achieved is 30 x 40 cm;
(2) for the data obtained to be sufficient for image reconstruction, the number of projections per rotations acquired has to be doubled;
(3) misregistration between high and low energy data;
(4) the low energy spectrum is restricted to 80 kVp, which can be a problem with large patients- currently only patients that are less than 260 pounds (118 kg) can be imaged;
(5) challenges in matching the noise between the low and high energy spectral data because current CT systems cannot modulate the tube current at the same rate as the tube potential; and
(6) in the GE Healthcare DECT system (Discovery CT 750HD), there can be an increase the radiation dose to a patient because the use of tube current modulation is not supported.

Use of energy sensitive double-layered detector: In this method of implementing DECT, the projection data are acquired using a single x-ray source while the separation into high- and low- energy image data sets is done by the double-layered ("sandwich") detector [133, 136]. As the name implies, the detector is made of two detectors composed of different materials and thicknesses, one placed on top of the other, and is sensitive to different energy x-rays as a function of depth. The low- and high- energy x-rays are mostly absorbed by the top and bottom layers of the detector, respectively, and from which images are reconstructed separately [5, 113, 137]. Figure 4.2 shows a schematic drawing of Philips Healthcare CT scanner (Brilliance 64) that employs this method; the x-ray tube peak voltage commonly used is 120 kVp or 140 kVp [127]. Two advantages of this method are [113, 137]: (1) dual-energy analysis can be performed on every data set acquired because the low- and high- energy data sets are acquired simultaneously, and the data from both layers of the detector are recorded at all times; and (2) it offers perfect temporal registration and spatial resolution between the low- and high- energy projection data. The disadvantages associated with it, which are mostly attributed to the complex

detector design, include [113, 132, 137]: (1) the detector has a limited energy resolving capabilities because of the large amount of overlap between the low-and high- energy data; (2) there may be difference in noise level between the low- and high- energy images.

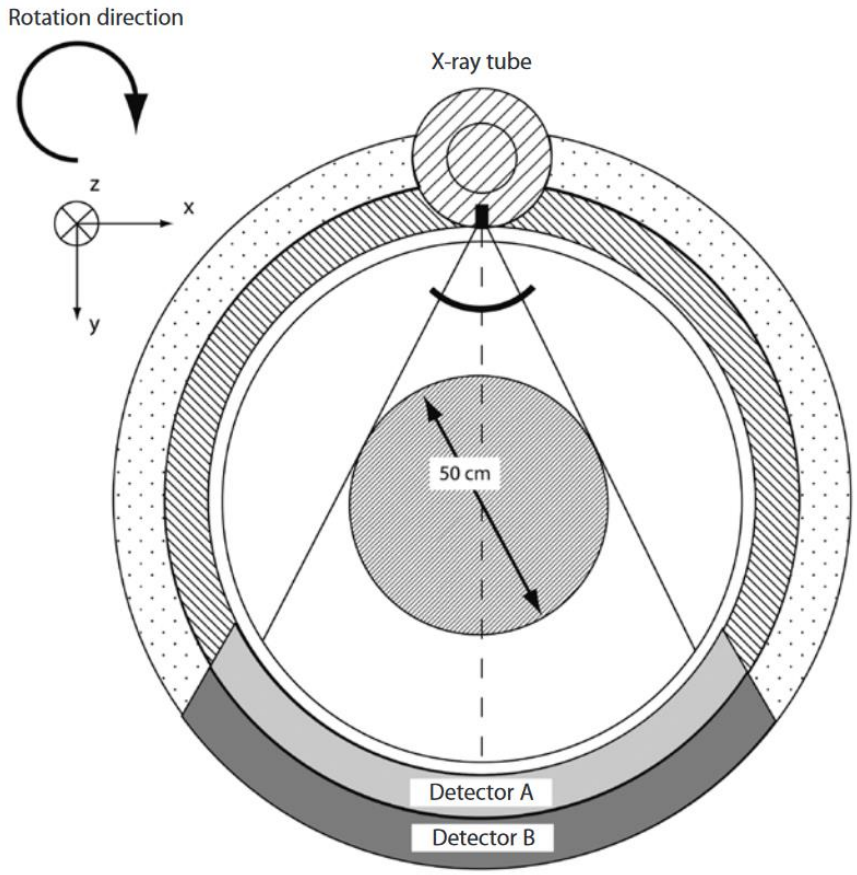

Figure 4.2: A schematic drawing of Philips Healthcare double-layered detector DECT scanner (Brilliance 64). **Source:** Ref [127].

***Dual x-ray source*:** The dual x-ray source method involves the use of two x-ray sources and two detectors mounted at right angles on the same rotating gantry with the x-ray sources operated at different peak tube voltages, usually 80 and 140 kVp [113, 116]. Thus, the low and high energy spectra projection data sets are acquired concurrently, and during a single gantry rotation[137]. Siemens Healthcare DECT scanner (SOMATOM definition) is based on this method, a schematic drawing of it is shown in figure 4.3 [127].

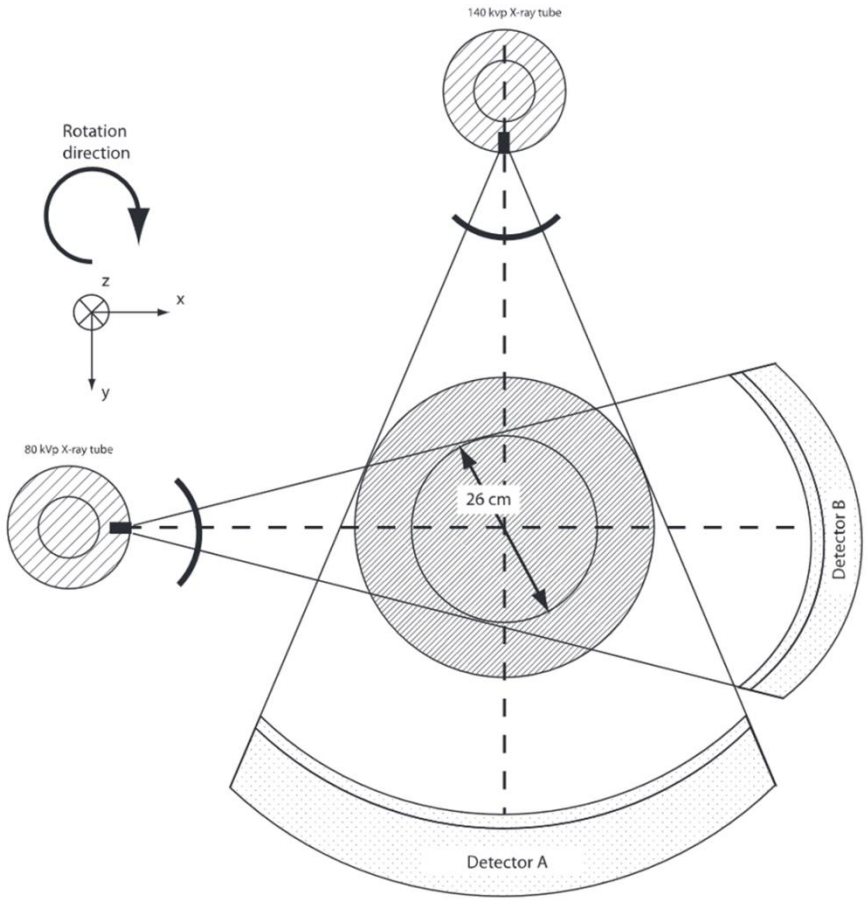

Figure 4.3: A schematic drawing of Siemens Healthcare dual x-ray source DECT scanner (SOMATOM definition). **Source:** Ref [127].

One major advantage of this method over the other two methods of DECT described above is the ability to optimize independently the spectral filtration for each tube-detector pair. This increases the spectral separation and signal-to-noise ratio in the material-specific images[113]. In addition, the adjustment of the x-ray tube current for each kVp level is done separately, which results in a comparable noise levels and radiation dose for the two acquired data sets [138]. This method also has disadvantages [113, 132, 133]: (1) there is a slight difference in the time that the two data sets are acquired, this limits temporal registration; (2) the field of view for the low x-ray energy source is reduced, this can hinder the evaluation of some body parts of obese patients; (3) there may be cross-scatter of x-rays between the two source-detector pairs which may in turn degrade the spectral separation unless a suitable scatter-correction algorithm is used.

Apart from the above three methods of DECT that have been implemented in commercially available CT systems, other methods have also been developed for research. For

example, a multi-energy CT system developed for small animals; a picture of it is shown in figure 4.4 [139]. One of the major components of this CT system is a Highly-Oriented Pyrolytic Graphite (HOPG) Bragg monochromator that is coupled to an x-ray tube, and is the source for the quasi-monochromatic x-ray beams (energy range: 20 to 70 keV) used in multi-energy applications.

Figure 4.4: A picture of a multi-energy x-ray system for small animals. **Source**: Ref. [139].

Another example is a triple-energy x-ray system developed by Baek and Kim [140, 141]. Their system involved an x-ray tube, three K-edge filters (iodine, barium and gadolinium) and a direct conversion detector. For the generation of the triple-energy x-ray beams, they used three different tube voltages with the three K-edge filters: iodine filter at 50 kVp; barium filter at 60 kVp; and gadolinium filter at 70 kVp. They had the K-edge filters built on the exit window of the x-ray tube to allow the three x-ray beams to exit.

4.1.2 Synchrotron x-ray source based methods

Synchrotron x-ray source based MEI systems that have been developed at various beamlines across synchrotron facilities, are mostly centered on KES imaging methods. These systems, some of which have been discussed in the Section 3.2.1 of this thesis, include: multiple energy CT (MECT) for imaging of the human head and neck [48, 121, 142]; Dual-energy imaging systems for various types of angiography including human coronary angiography [17, 85, 92, 93, 143], contrast enhanced digital mammography [144]; dual-beam KES imaging system at the Swiss Light Source TOMCAT beamline [145]; and a spectral-KES system developed for biomedical imaging applications at the CLS biomedical imaging and therapy (BMIT-BM) beamline [90]. The Dual-beam KES imaging system at the TOMCAT beamline is quite different from other KES systems here stated in that it uses a Laue-Bragg splitting scheme (figure 4.5). One unique fact about synchrotron based MEI systems is that the separation of the synchrotron x-rays energies is commonly done by the monochromator that constitutes a part of the imaging system. Also the use of a monochromator, even if bent, to increase the efficiency or bandwidth, has a narrow range of energies compared to x-ray tube based systems that rely on kVp and filtration to set the imaging energies.

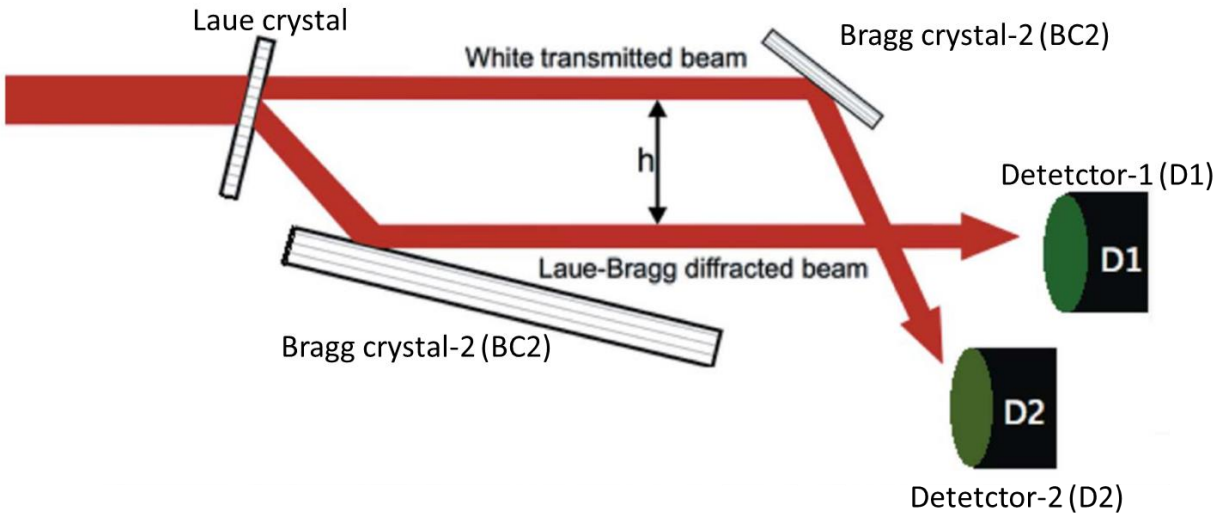

Figure 4.5: Dual-beam KES setup at TOMCAT beamline, Swiss Light Source. **Source:** Ref. [145].

4.2 Detectors

An integral part of any MEI system is the x-ray detector. From the three established methods of MEI in clinical DECT systems described in Section 4.1.1 of this Chapter, one of them (double-layered detector) is attributed to the detector type used. It is interesting to note that the development in digital x-ray detecting technology has greatly impacted the development of MEI systems [119, 120, 124, 146, 147]. Energy-integrating detectors (EIDs) as well as photon-counting x-ray detectors (PCDs) have been used in MEI systems. A detector array that combines the energy-integration and photon-counting of x-rays has been proposed for spectral CT [125]. In EIDs the total electric current produced from detected photons, which are summed and measured, provide information about the energy of the photons. But in PCDs the energy information is provided for each photon [148].

New generation PCDs with the ability to discriminate photon energies based on pulse height analysis have been developed [116, 149]. These new generation PCDs are equipped with multithresholding circuits and are able to simultaneously count, discriminate, and bin photons of different energies based on the chosen thresholds [116, 150]. Medipix chip based PCDs - Medipix1, Medipix2 and Medipix3 [151] are examples of PCDs that count and discriminate the photons energies. Other examples are as listed in the publication by Katsuyuki and Jan [149]. The introduction of these PCDs to the field of medical applications is said to have opened up new possibilities in the field, and offer a number of advantages when used for MECT: (1) no registration issues between different x-ray energies because the energies are all acquired simultaneously; (2) no overlap in the x-ray energy ranges; (3) many energy levels can be recorded depending on the detector's electronics; and (4) energy ranges can be set arbitrarily to optimise the image analysis software in order to discover the imaging problem [132]. Examples of some of the new possibilities are as follows. Schlomka et al. [122] demonstrated experimentally the feasibility of quantitative K-edge CT imaging in a pre-clinical system that uses a single-line photon-counting CdTe array capable of discriminating more than two energy bins. In an experimental study by Polad [152], a photon counting spectroscopic CT (PCS-CT) technology that could be used for breast CT was presented. The spectroscopic CT system was based on CdZnTe PCD that can split the x-ray energy spectrum into five energy bins, and can acquire 5 multi-energy (spectroscopic) CT images in a single CT scan. Ronaldson et al. [118] showed that spectral CT with Medipix3 PCD has the potential to independently decompose

calcium, fat, and water in soft tissues. This they did in soft tissues within small animal models and surgical specimens of diseases such as fatty liver (metabolic syndrome) and unstable atherosclerosis. In both simulations and physical experiments, Wang et al. [153] concluded that " x-ray CT with an energy resolved photon-counting detector with more than two energy windows allows the separation of more than two types of materials, e.g., soft-tissue-like, bone-tissue-like, and one more or materials with K-edges in the energy range of interest".

The advances in flat panel detectors (FPDs), which are EIDs, have also offered new possibilities for MEI applications [154]. Xu et al. [120] developed a dual-energy imaging technique with dynamic filtration using a CsI-based FPD. They stated that the imaging method can potentially be used as a low dose technique for quantifying coronary arterial calcium. In their imaging technique, the x-ray beam was switched at 15 Hz between 60 kVp and 120 kVp; the 120 kVp beam had an additional 0.8 mm silver filter. Han et al. [155] described a single-shot (single kVp) dual-energy imaging method (for preclinical imaging) that uses a prototype multilayer ("sandwich") - detector system consisting of two x-ray imaging FPDs. Each of the two sandwiched FPD consisted of a commercially available terbium-doped gadolinium oxysulfide (Gd_2O_2S:Tb) scintillator optically coupled to a complementary metal-oxide semiconductor (CMOS) matrix-addressed photodiode array. The spectral separation between the two detectors was increased by using an intermediate copper filter. This improved the image contrast though at the expense of image noise. For the single kVp, the x-ray tube voltage was varied between 40 and 70 kVp. They demonstrated the potential of this method by acquiring dual-energy bone and soft-tissue images of a post-mortem mouse, and claimed that the method is insensitive to motion artifacts.

With respect to SR based x-ray imaging, the use of PCDs is a problem because of pulse pileup effect. Pulse pileup occurs when the arrival of two detected x-ray photons overlap in the time the detector takes to convert the photon's deposited energy into a signal. This deposited energy usually (or eventually) takes the form of charge released. When photons overlap or "pileup" the ability to determine their respective energies is destroyed and the two events are typically rejected resulting in count loss [149, 156-158]. Generally, the probability of pulse pileup occurring is dependent on the x-ray flux on the detector [159]. The issue of pulse pileup in PCD is more problematic when SR is used compared to when x-rays from x-ray tubes are used. This is due to the pulse nature of SR sources which produces pulsed time structured SR (few

microseconds between pulses) that is shorter than the resolving time of PCDs; X-ray tubes are steady sources of x-rays [159-162]. But the recent developments in PCDs technologies are improving their performance in SR applications [163].

4.3 Material Decomposition Algorithms

X-ray attenuation by matter is a well-known fact. The attenuation can be described by physical interactions between the x-rays and matter or analytically as a linear combination of basis functions representing a collection of absorbing materials [116]. In tissues with a contrast element three basis functions can be used to describe the attenuation. The two choices are: photoelectric effect, Compton scattering, and discontinuity at a K-edge of an element or mass attenuation coefficients of water, bone, and a contrast element [116, 149]. The discontinuity at a K-edge is only used if a material has a K-edge of an element in the energy range of interest [153]. This particular basis function contains information in the spectral dimension about the presence of an exogenous element, which enables the extraction of selective and quantitative information of a contrast agent carrying such elements if present [116]. The first concept of material decomposition using multiple energy (dual-energy) spectra, reported in the year 1976, was that put forward by Alvarez and Mascovski [9]. It was based on the use of photoelectric effect and Compton scattering as the basis functions. Since then, several methods for decomposition of spectral data have been developed, all centred on the above three stated basis functions [118, 131]. Material decomposition algorithms enable material-specific information such as mass density and effective atomic number to be obtained, and also the quantification of material concentration [113]. With an accurate material decomposition algorithm, the spatial distribution of basis functions can be quantified on a pixel basis [149]. It should be noted that in the diagnostic energy range (18 to 150 kVp), photoelectric absorption and Compton scattering are the two principal means materials attenuate x-ray and hence the two basis functions commonly used [116]. An example of a method used for material decomposition is described as follows [110, 135, 164, 165]**.**

Consider a subject for which the photon counts for incident, N_0, and transmitted, N, beam are measured at some energies, $E_i \leq i \leq n$. $N(E_i)$ and N_0 (Ei) can be normalized to form:

$$R_i = -\ln\left(\frac{N(E_i)}{N_0(E_i)}\right) \tag{4.1}$$

Based on Lambert-Beer's law, eqn. 4.1 can be related to the expected attenuation of the object by m materials for $1 \le j \le m$ and $1 \le i \le n$ as

$$r_i = \sum_{j=1}^{m}\left(\frac{\mu}{\rho}\right)_j (E_i)\rho_j t_j = \sum_{j=1}^{m}\left(\frac{\mu}{\rho}\right)_{ji} \rho_j t_j \text{ where the i index refers to } E_{i.} \tag{4.2}$$

That is,

$$r_i = -\ln\left(\frac{N(E_i)}{N_0(E_i)}\right) = \sum_{j=1}^{m}\left(\frac{\mu}{\rho}\right)_{ji} \rho_j t_j \tag{4.3}$$

Equation 4.3 is linear and its matrix form is

$$\begin{bmatrix} r_1 \\ . \\ . \\ r_i \\ . \\ . \\ r_n \end{bmatrix} = \begin{bmatrix} -\ln\left(\frac{N_1}{N_{01}}\right) \\ . \\ . \\ -\ln\left(\frac{N_i}{N_{0i}}\right) \\ . \\ . \\ -\ln\left(\frac{N_n}{N_{0n}}\right) \end{bmatrix} = \begin{bmatrix} \left(\frac{\mu}{\rho}\right)_{11}\rho_1 t_1 + .. + \left(\frac{\mu}{\rho}\right)_{j1}\rho_j t_j + .. + \left(\frac{\mu}{\rho}\right)_{m1}\rho_m t_m \\ .. \\ .. \\ \left(\frac{\mu}{\rho}\right)_{1i}\rho_1 t_1 + .. + \left(\frac{\mu}{\rho}\right)_{ji}\rho_j t_j + .. + \left(\frac{\mu}{\rho}\right)_{mi}\rho_m t_m \\ .. \\ .. \\ \left(\frac{\mu}{\rho}\right)_{1n}\rho_1 t_1 + .. + \left(\frac{\mu}{\rho}\right)_{jn}\rho_j t_j + .. + \left(\frac{\mu}{\rho}\right)_{mn}\rho_m t_m \end{bmatrix}$$

$$\begin{bmatrix} r_1 \\ . \\ . \\ r_i \\ . \\ . \\ r_n \end{bmatrix} = \begin{bmatrix} \left(\frac{\mu}{\rho}\right)_{11} + .. + \left(\frac{\mu}{\rho}\right)_{j1} + .. + \left(\frac{\mu}{\rho}\right)_{m1} \\ .. \\ .. \\ \left(\frac{\mu}{\rho}\right)_{1i} + .. + \left(\frac{\mu}{\rho}\right)_{ji} + .. + \left(\frac{\mu}{\rho}\right)_{mi} \\ .. \\ .. \\ \left(\frac{\mu}{\rho}\right)_{1n} + .. + \left(\frac{\mu}{\rho}\right)_{jn} + .. + \left(\frac{\mu}{\rho}\right)_{mn} \end{bmatrix} \times \begin{bmatrix} \rho_1 t_1 \\ . \\ . \\ \rho_j t_j \\ . \\ . \\ \rho_m t_m \end{bmatrix} \tag{4.4}$$

Equation 4.4 is an n x m matrix, where r_i (1≤ i ≤ n) are compared with R_i (the measurements made, i.e., the image data acquired) and $\rho_j t_j$ (1≤ j ≤ m) are the materials projected mass densities (projected mass concentrations) to be solved for, which can be done, for example by method of linear least squares (LLSQ) [164]. For equations of this type, the following conditions apply [11, 164]: if n = m, $\rho_j t_j$ can be determined; if n < m, $\rho_j t_j$ cannot be determined and; if n > m, $\rho_j t_j$ are overdetermined. The ability to solve for the "m" materials depends on inversion of the matrix in equation 4.4 which can lead to a singular matrix if the attenuation coefficients as a function of energy are linearly related to one another. For example, one would not be able to solve for water (H_2O), oxygen (O) and hydrogen (H) independently. Also, materials that are very close in energy dependence will present difficulties in solving for such as a soft tissue and plastic (for example, poly-methyl-methacrylate or PMMA, commonly known as acrylic).

Certain quantities or variables such as chemical concentrations, amount of materials, pixel intensities, frequency counts, and emission spectra, can never take negative values based on physical principles [166-168]. Problems in which these types of variables are to be solved for usually involve solving overdetermined linear systems (i.e., linear systems that have more equations than the variables to be solved for), and are termed LLSQ problems [169]. When solving LLSQ problems for quantities than can only take on non-negative values, if the measured data used are corrupted by noise, the quantities can take on negative values, which are physically meaningless [167, 170]. To ensure non-negative values, non-negative least squares (NNLS) methods or non-negative constrained least squares methods are used [12, 168, 170-172].

CHAPTER 5

A SYCHROTRON BASED MULTIPLE ENERGY BIOMEDICAL IMAGING SYSTEM

The BMIT facility at the CLS has a number of imaging methods. Being one of the eight known SR biomedical imaging facilities existing in the world, and in order for it to be more attractive to users (researchers), there is the need at BMIT to develop new imaging methods and improve upon the existing ones. Spectral-KES, a new MEI method developed at BMIT, has already been put into use and some positive research results published [98, 173, 174]. With the growing interest in the development of MEI methods, which is not limited only to the use of conventional x-ray sources but also SR, the decision to develop yet another new and novel MEI at BMIT was considered a good one. Details of the novel MEI is presented in this chapter. The novel aspects of this MEI system are: (1) large spectral energy range of the horizontally focused beam achieved, up to 15 keV with a middle energy around 30 keV; (2) spectral energy range of the focused beam covers the K-edges of four elements [iodine (33.17 keV), xenon (34.56 keV), cesium (35.99 keV), and barium (37.44 keV)], three of which are commonly used as contrast agents in x-ray imaging (iodine, xenon and barium); and (3) ability to extract up to six materials from the spectral energy data. Again it is emphasized that unlike spectral-KES that can be done in either planar or CT mode, imaging with the novel MEI can only be done in planar mode.

5.1 Components of the MEI System

The MEI system is made up of a cylindrically bent Laue single silicon (Si) crystal (wafer) monochromator, scanning and positioning stages for subjects to be imaged, a 100 μm pixel size FPD, and a data acquisition and control system. The FPD, an EID, is C9252DK-14 (Hamamatsu Photonics K. K., Japan), a detector commonly used in some clinical dental x-ray machines [175]. A crystal whether flat or bent can be used either in the reflection (Bragg crystal) or transmission (Laue crystal) geometry. The MEI system bent Laue monochromator is used in the focusing geometry. The thickness of the bent Si crystal (5, 1, 1) is 750 microns and for the diffraction of

synchrotron x-rays, the (3, 1, 1) type diffraction (reflection) plane having an asymmetry angle of 3.3° is used. The asymmetry angle is measured in the diffraction plane between the crystal surface normal and the diffraction planes. Figure 5.1 is an illustration showing the orientation of the crystal and lattice planes used for the MEI system. It should be noted that in figure 5.1, the planes are not bent. Also, commas have been used to separate the integers and 'minus sign' instead of a 'bar' on the integers just for the purpose of clarity. The crystal was bent using a frame bender. This was achieved by mounting the crystal onto an aluminium frame machined to the required bending radius of 1 m (figure 3.4). An aluminum frame was used because of its good thermal conductivity, light weight, ease of machinability and low cost. At the early stage of the MEI system development, bending of the Si crystal wafer was done using a four-bar bender (figure 3.2), which allowed for the variation of the crystal's bending radius. A Si (5, 1, 1) was still used but its thickness was 600 μm, and the reflection type (1, 1, 1) with an asymmetry angle of 19.5°. The (3, 1, 1) type reflection from a Si (5, 1, 1) crystal wafer of 750 μm thickness was opted for because of its excellent energy dispersive properties for spectral K-edge subtracting imaging [90]. Generally, in bent crystals there is an increase in the angular and energy acceptance of the x-rays incident on them compared to flat crystals, and hence an increase in the x-ray flux available for usage [88]. Even though the reflectivity of the crystal drops, this is overcome by the increased angular and energy acceptance. The crystal when bent moves away from dynamical type behaviour to kinematical behaviour where the overall integrated reflectivity is much higher. The bending of the crystal causes a change in the angle and d-spacing of the lattice planes as the beam traverses the crystal, which results in an increment in the energy bandwidth. The enhancement of the energy bandwidth due to bending is approximately 100 times the unbent values [79]**.** Also the reflectivity and diffraction efficiency of bent crystals can be close to 100 % [176].

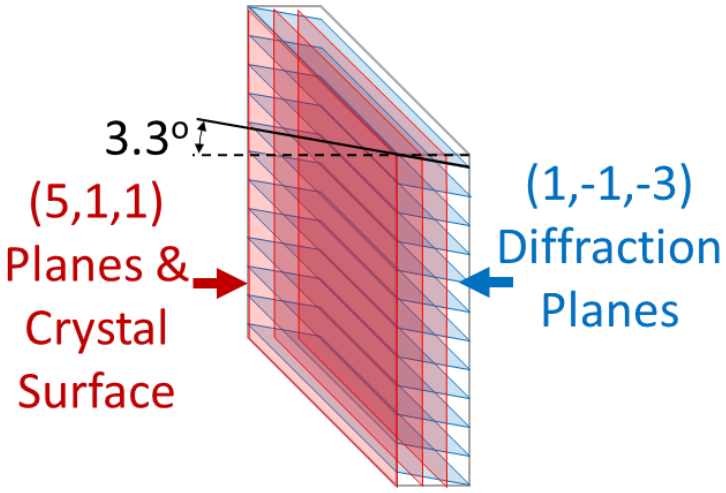

Figure 5.1: An illustration showing the orientation of the crystal and lattice planes used for the MEI system. The crystal surface is parallel to the (5, 1, 1) planes. The planes used for diffraction through the crystal are the (1,-1,-3) which are inclined at 3.3^{o} relative to the surface as shown. The planes in the figure are not bent for clarity. **Source**: Ref. [178].

A filtered synchrotron white (polychromatic) beam of energy range 20 to 50 keV is used. The bent Laue Si crystal focuses in the horizontal plane, thus when the filtered synchrotron white beam is incident on the bent Si crystal, a horizontally focused polychromatic synchrotron x-ray beam is prepared. Filtering of the white beam is done using a 0.1 mm thick aluminum (one of the BMIT-BM filters) and 105 mm thick water filter. The thin aluminum filter serves two purposes: (1) it removes most of the low energy part of the spectrum that can create ozone in the experimental hutch, which can be a health hazard and also oxidizes equipment, and (2) the reduction of the beam power will prevent the beam from melting the tank containing the water filter. Water, a low atomic number material, is used as a filter to evenly attenuate the large energy range spectrum since the attenuation is dominated by Compton scattering, which is largely energy independent. Though the water filter does scatter the white beam, this has no negative effect on the MEI system because it is located upstream of the MEI system (~5 m) in the BMIT-BM experimental hutch. A subject to be imaged will be placed at the beam's focal point; the focused beam on passing through the subject diverges onto the FPD where the energy range collected is spatially dispersed. At the subject location where the beam focuses, the beam has a horizontal width along x and the range of angles through the focus (angles around the x direction) represents a range of x-ray energies. At the detector location downstream, the range of

angles spatially disperses the x-rays as a function of energy across the horizontal dimension of the detector. The horizontal or x dimension is preserved from the object location. To create an image of a subject, the subject is scanned horizontally through the focused beam, creating a 2 spatial dimensional image: height (y) - vertical beam size; width (x) - horizontal scan length; and a third axis representing the transmission through the object at the x-y location as a function of energy, which can be as large as 17 keV. Thus, each x-y pixel in the detector represents the x-ray transmission through the subject at a horizontal location (x) and the vertical location (y), the transmission through the subject at an energy. A schematic representation and geometry of the MEI system are shown in figure 5.2, and its experimental setup shown in figure 5.3.

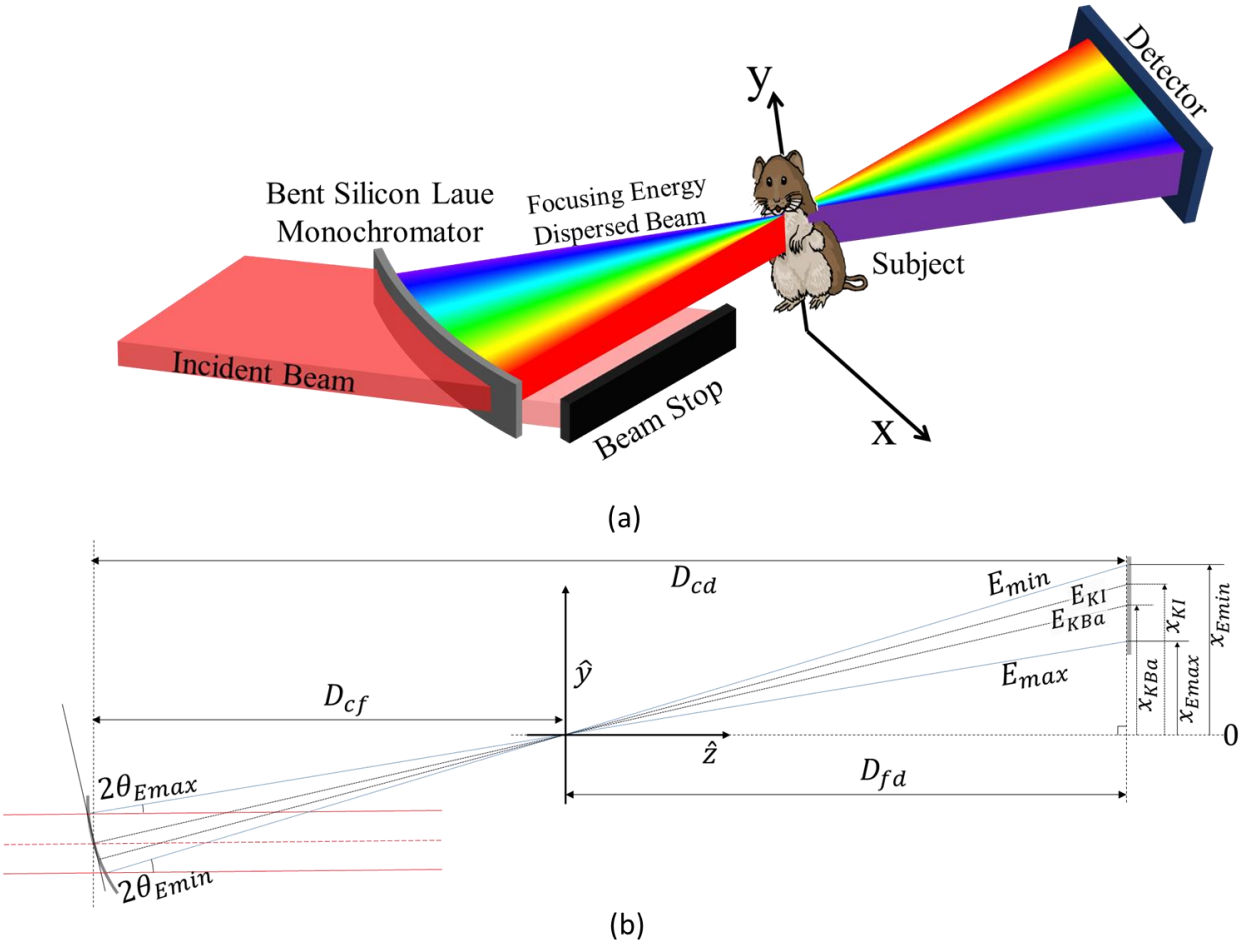

Figure 5.2: (a) Schematic representation of the MEI system (**Source**: Ref. [178]), and (b) the MEI Geometry. The frame bender used for bending the Si crystal wafer is not shown in the figure. The detector is perpendicular to incident beam direction, z. D_{cd}, D_{cf}, and D_{fd} are the distance from crystal to detector, crystal to beam's focal point, and beam's focal point to detector, respectively.

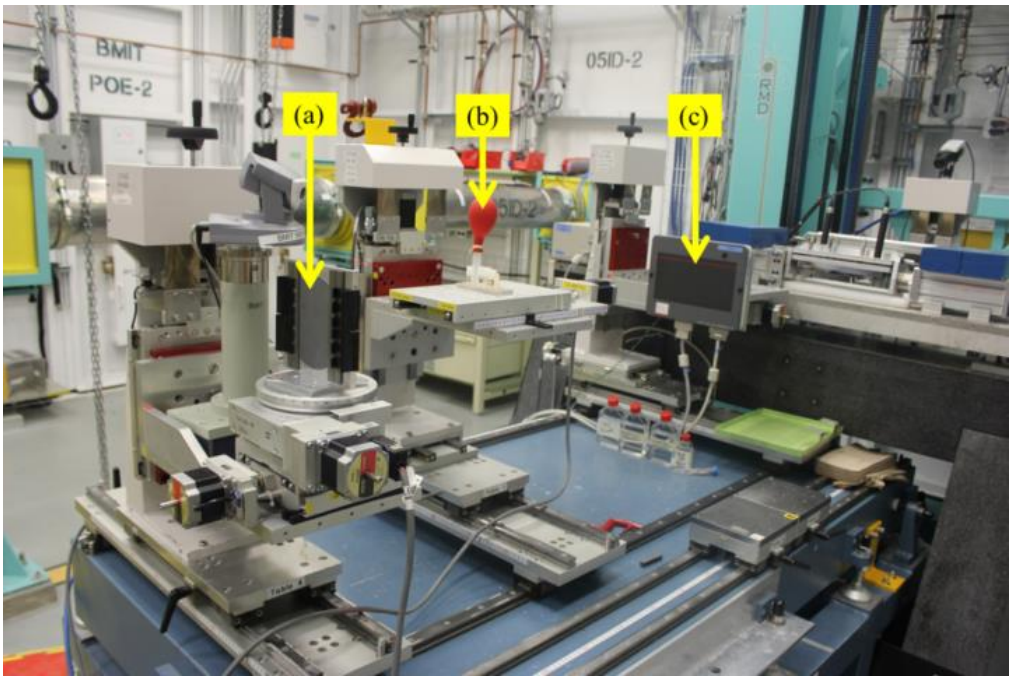

Figure 5.3: Experimental setup of the MEI system: (a) Si crystal wafer mounted on a frame bender, (b) subject to be imaged placed at the position the beam focuses and, (c) Hamamatsu flat panel detector. **Source**: Ref. [178].

5.2 Focal Properties Study

Again, the MEI system focuses the synchrotron white x-ray beam to be used for imaging in the horizontal plane. A study of the focal properties of the MEI system was done by measuring the focus size of the focused beam (imaging beam) prepared by the bent Laue Si crystal monochromator. This was done in two ways, and for various beam sizes incident on the Si crystal monochromator. One set of measurements involved scanning a knife edge horizontally through the focused beam at various distances near the focal point to establish its location. For the second set of measurements, experimental setup shown in figure 5.4, a 13 μm pixel size detector, Hamamatsu AA-60 x-ray converter coupled to a C9300-124 camera (Hamamatsu Photonics K. K., Japan), was used to directly image the beam near the focal region. The C9252DK-14 (Hamamatsu Photonics K. K., Japan) FPD which constitutes a part of the MEI system was not used for this study due to its susceptibility to radiation damage. In the AA-60 x-ray converter, the lens and charge-coupled device are out of the x-ray beam and thus radiation damage is not a problem. The focal properties obviously depend on the bend radius which is

fixed, but also on the Laue diffraction conditions-specifically the reflection plane used, x-ray energy and asymmetry angle. With a focusing bent Laue geometry, there are two foci, the polychromatic and geometric. And it is only when these two foci coincide that the smallest possible focus size can be achieved.

From geometry, with the Si crystal wafer bent to a radius of 1 m, the expected focal point should be at approximately 0.5 m from the Si crystal. But due to the fact that geometric and polychromatic foci do not generally match over the energy range of the experiment, a point or source size limited focus cannot be achieved, and at the expected focal point. Scanning the region close to the expected focal point using the Hamamatsu AA-60 detector enabled the smallest possible focal size, and its position from the Si crystal to be determined. The experimental setup and geometry for beam's focal size measurements using the Hamamatsu AA-60 detector is shown in figure 5.4. The results of the scans around the focal region, for different beam sizes incident on the bent crystal are shown in figure 5.5. It should be noted that the scan direction of the AA-60 detector is along the incident beam path. The data in figure 5.5 have been resampled to follow the overall beam trajectory to better show the focal properties of the beam.

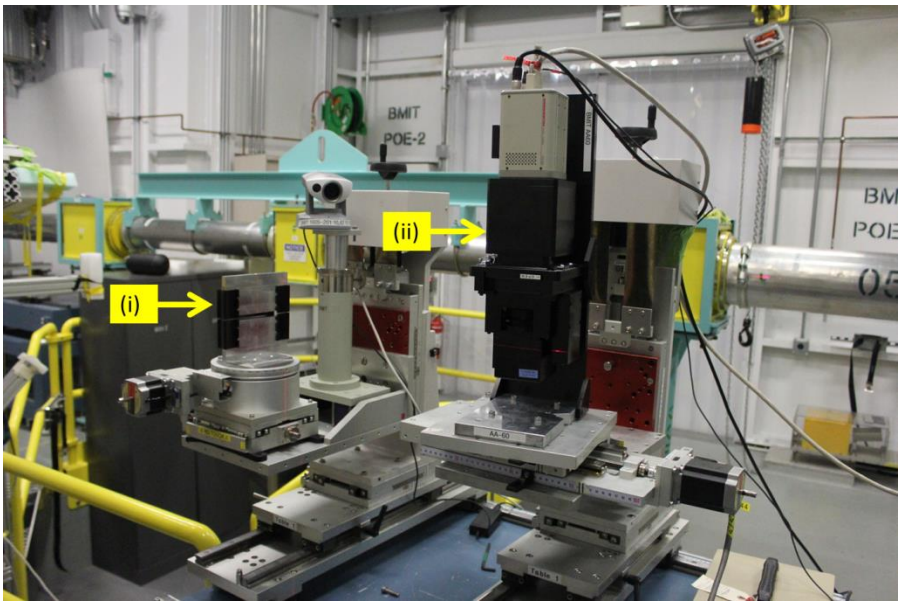

(a)

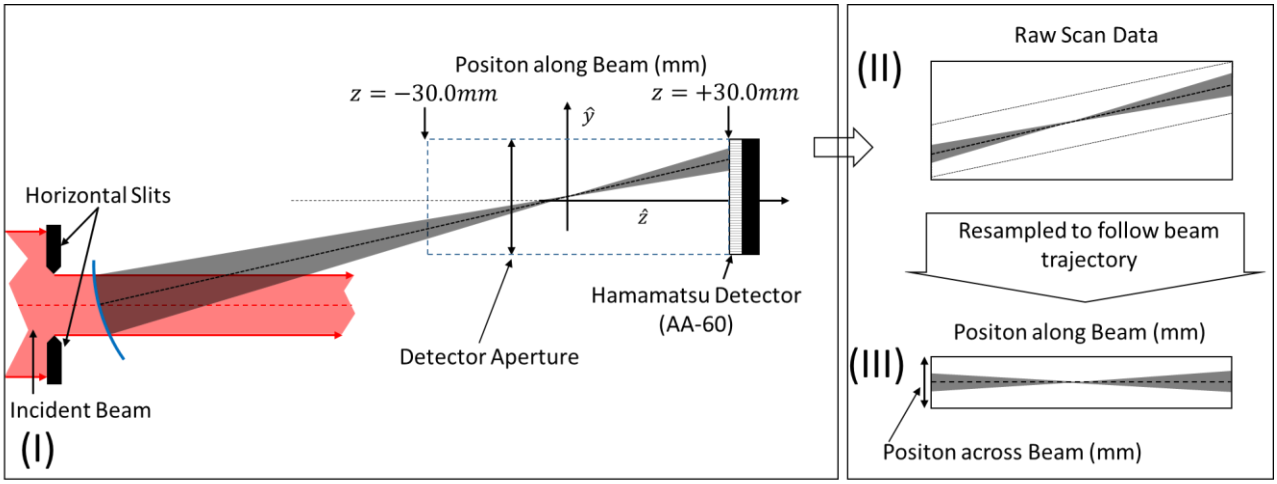

(b)

Figure 5.4: (a) A picture of the experimental setup and (b) geometry for beam's focal size measurements using Hamamatsu AA-60 detector. (a) (i) Si crystal wafer mounted on a frame bender,(a) (ii) Hamamatsu AA-60 x-ray converter coupled to a C9300-124 camera. In (b) (I) the detector is scanned ±30mm along the z direction (parallel to incident beam direction) in 1mm steps around the focal point. The incident beam width is adjusted using beamline horizontal slits. The data acquired have the beam at an angle across the raw data as shown in (b) (II). These data are then resampled from the dotted region in (b) (II) to the rectangular region in (b) (III). The resampled data are shown in figure 5.5.

From figure 5.5, the 0 mm position along the beam (vertical axis) is the expected geometric focal point, 0.5 m from the crystal while the scan was performed from the -30 mm position (upstream) to the +30 mm position (downstream). Based on the scans, the smallest focal size achieved was 0.2 mm, and was between -1 mm and 4 mm from the 0 mm position. For the focus size measurements by scanning a knife edge horizontally through the beam, the smallest focus size measured was 0.3 mm. The image for each of the beam dimensions shown in figure 5.5 was created from a number of images taken of the beam as the 13 μm pixel size Hamamatsu AA-60 detector translated along the beam path. Efforts were made to get the trajectory of the detector to match the overall path of the beam, but there was some residual error which resulted in a slight inclination of the beam relative to the x-y axes (~0.7degrees).

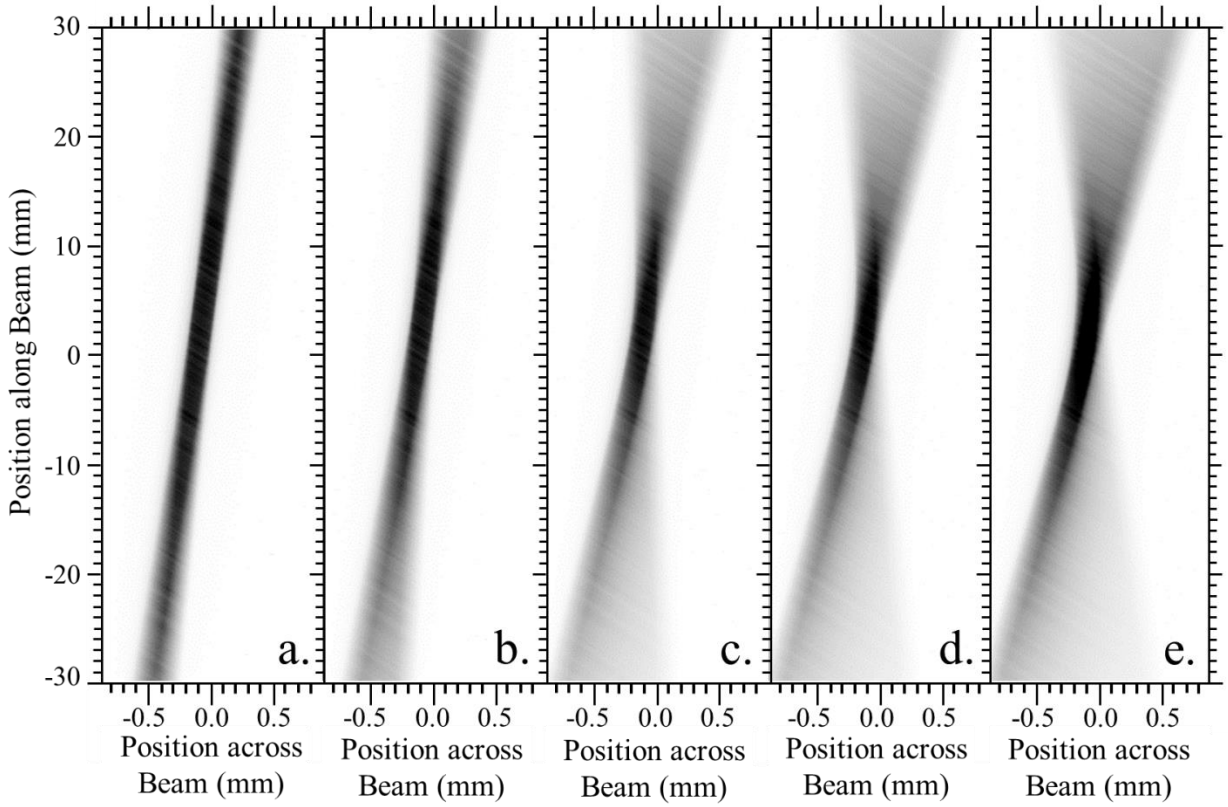

Figure 5.5: Results of scans about the focal point using the 13 μm pixel size Hamamatsu AA-60 detector. Vertical beam size incident on the bent Laue Si crystal monochromator was 6 mm while the horizontal beam size was varied: (a) 5 mm, (b) 10 mm, (c) 20 mm, (d) 25 mm, and (e) 30 mm. **Source**: Ref. [178].

5.3 Image Data Acquisition and Materials Decomposition

The data and order acquired are: Darks, Flats, Edges and Tomos.

- Darks(N_D):shutter closed, no beam unto detector
- Flats(N_0): shutter opened, no phantom (sample) in beam path
- Edges (N_E): shutter opened, a mixture of NaI (iodine) and $BaCl_2$(barium) solution in the beam path, used for calibrating x-ray energy on the detector
- Tomos (N): shutter opened, phantom (sample) in beam path

Shutter is a device that when opened, allows beam into the experimental hutch. The Tomos and Edges data are then normalized as shown in eqn. 5.1, and represents the image data. For the Edges data, N in eqn. 5.1 is replaced with N_E.

$$R_i = -\ln\left(\frac{N(E_i) - N_D}{N_0(E_i) - N_D}\right) \tag{5.1}$$

where $1 \leq i \leq n$ are the x-ray energies at which the measurements are made.

In order to be able to decompose m number of materials, the number, n, of x-ray energies in the spectral data should be $n \geq m$. In our case, the maximum number of materials we solved for was six (i.e. m = 6) while the number of x-ray energies (keV) in the spectral data was up to 358 (i.e. n = 358). Recalling eqn. 4.4 shown below, for our case the $\rho_j t_j$ are overdetermined because n > m.

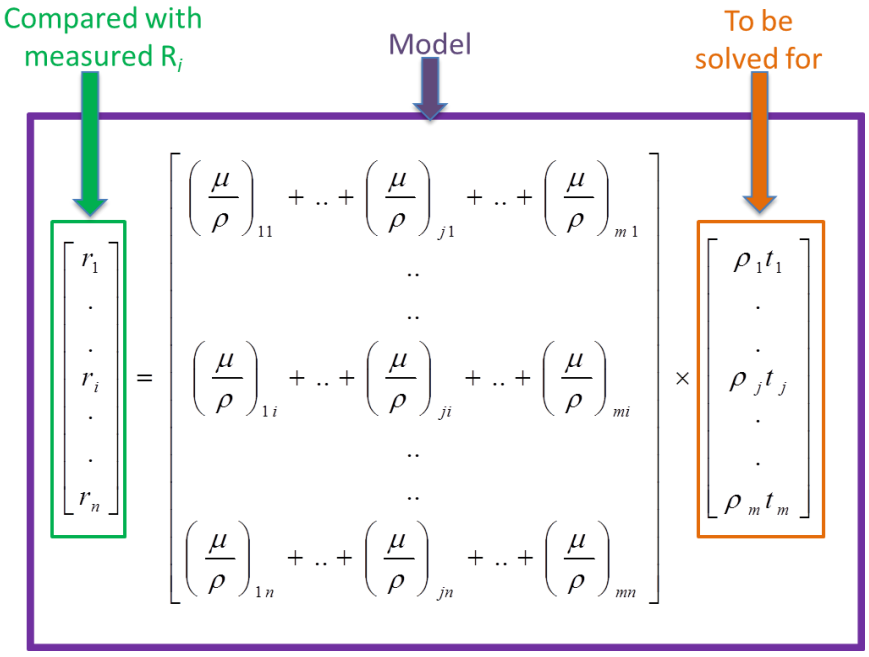

Due to n > m, the materials were decomposed using the method of Linear Least Squares (LLSQ), which gives approximate values of $\rho_j t_j$; the projected mass density (projected mass concentrations). The LLSQ algorithm used inverts the matrix in eqn. 4.4 and then performs a minimization process, minimizing the error, **e**, between R_i and r_i:

$$\mathbf{e} = \sum_{i=1}^{n} \left(R_i - r_i\right)^2$$

$$\mathbf{e} = \sum_{i=1}^{n} \left(R_i - \sum_{j=1}^{m} \left(\frac{\mu}{\rho}\right)_{ji} \rho_j t_j \right)^2 \tag{5.2}$$

where $\rho_j t_j$ are the parameters adjusted in the model to minimize the error.

The LLSQ algorithm did not provide uncertainty estimates. However, the SNR were evaluated in the same way as explained in section 5.5.

With reference to the MEI geometry shown in figure 5.2(b), the steps involved in the calibration of the x-ray energy scale on the detector are as follows.

- The distance between the reflection planes (d spacing) of the Si crystal is computed using:
$$d_{hkl} = \frac{a_0}{\sqrt{h^2 + k^2 + l^2}}$$
- With the known values of the K-edges of iodine (E_{KI} = 33.169 keV) and barium (E_{KBa} = 37.441 keV), the corresponding wavelengths are computed using:
$$\lambda_{KI} = \frac{hc}{E_{KI}} \quad \text{and} \quad \lambda_{KBa} = \frac{hc}{E_{KBa}}$$
- With the computed d_{hkl}, λ_{KI}, and λ_{KBa}, the Bragg angles are then computed using:
$$\theta_{KI} = sin^{-1}\left(\frac{\lambda_{KI}}{2d_{hkl}}\right) \text{ and } \theta_{KBa} = sin^{-1}\left(\frac{\lambda_{KBa}}{2d_{hkl}}\right)$$
- The locations of the I and Ba K-edges on the detector are given by:
$$x_{KI} = D_{fd} tan(2\theta_{KI}) \; and \; x_{KBa} = D_{fd} tan(2\theta_{KBa})$$
- From the difference between x_{KI} and x_{KBa}, D_{fd} is computed:
$$x_{KI} - x_{KBa} = D_{fd}\left(tan(2\theta_{KI}) - tan(2\theta_{KBa})\right)$$
$$D_{fd} = \frac{x_{KI} - x_{KBa}}{tan(2\theta_{KI}) - tan(2\theta_{KBa})}$$

- Finally, the computed D_{fd} is used to calibrate the energy scale on the detector:

$$x_{Di} = D_{fd} tan(2\theta_{Di})$$

$$\theta_{Di} = \frac{1}{2} tan^{-1}\left(\frac{x_{Di}}{D_{fd}}\right)$$

$$x_{Di} = 2d_{hkl} sin\left(\frac{1}{2} tan^{-1}\left(\frac{x_{Di}}{D_{fd}}\right)\right)$$

$$E_{Di} = \frac{hc}{2d_{hkl} sin\left(\frac{1}{2} tan^{-1}\left(\frac{x_{Di}}{D_{fd}}\right)\right)}$$

x_{Di} is the location of the *ith* x-ray energy on the detector while θ_{Di} and E_{Di} are its corresponding Bragg angle and energy, respectively.

The energy range (20 keV to 50 keV) of the filtered synchrotron white beam incident on the bent Laue Si crystal monochromator covers the K-edges of the following elements: indium (27.940 keV); tin (29.200 keV); antimony (30.491 keV); tellurium (31.814 keV); **iodine (33.169 keV)**; **xenon (34.561 keV)**; cesium (35.985 keV); **barium (37.441 keV)**; and lanthanum (38.925 keV). The elements in bold are commonly used as clinical/biomedical contrast agents. It was found out that the spectral energy range of the focused beam (imaging beam) prepared varied depending on the Si crystal's bent radius, reflection type, and the horizontal beam width of the incident filtered white beam used. This is shown in table 5.1. The spectral energy range was found by using the energy calibration from the NaI and $BaCl_2$ solutions and extrapolated to the low and high energy limits of the imaging beam. At the focus, the spatial width of the beam was determined by a knife-edge scan and is the full width of the beam at that location. Figure 5.6a shows the images of the K-edges of all the elements covered (barium, Ba; cesium, Cs; xenon, Xe; and iodine, I) for the bold case with reference to table 5.1 while figure 5.6b shows the transmission through a mixture of NaI and $BaCl_2$ solution (segmentation of I and Ba K-edges from a mixture of NaI and $BaCl_2$ solution) used for energy scale calibration.

Table 5.1. Spectral energy range of the focused beam prepared by the MEI system.

Si (5,1, 1) crystal wafer's reflection used and thickness	Bend radius of Si crystal (cm)	Width of incident filtered white beam (mm)*	Width of focused beam (mm)	Spectral energy range of focused beam (keV)
FBB: (1,-1,-1)**, 600 μm	108	22.5	0.9	12.0
FBB: (3,1,1)***, 750 μm	95	50.0	0.5	16.0
FBB: (3,1,1)***, 750 μm	100	25.0	0.5	6.9
FB: (3,1,1)*, 750 μm**	**100**	**50.0**	**1.0**	**15.0**
FB: (3,1,1)***, 750 μm	100	25.0	0.5	9.3

FBB: Four-Bar Bender, FB: Frame Bender, * Vertical height of the beam was 6 mm, ** 19.5° asymmetry angle, *** 3.3° asymmetry

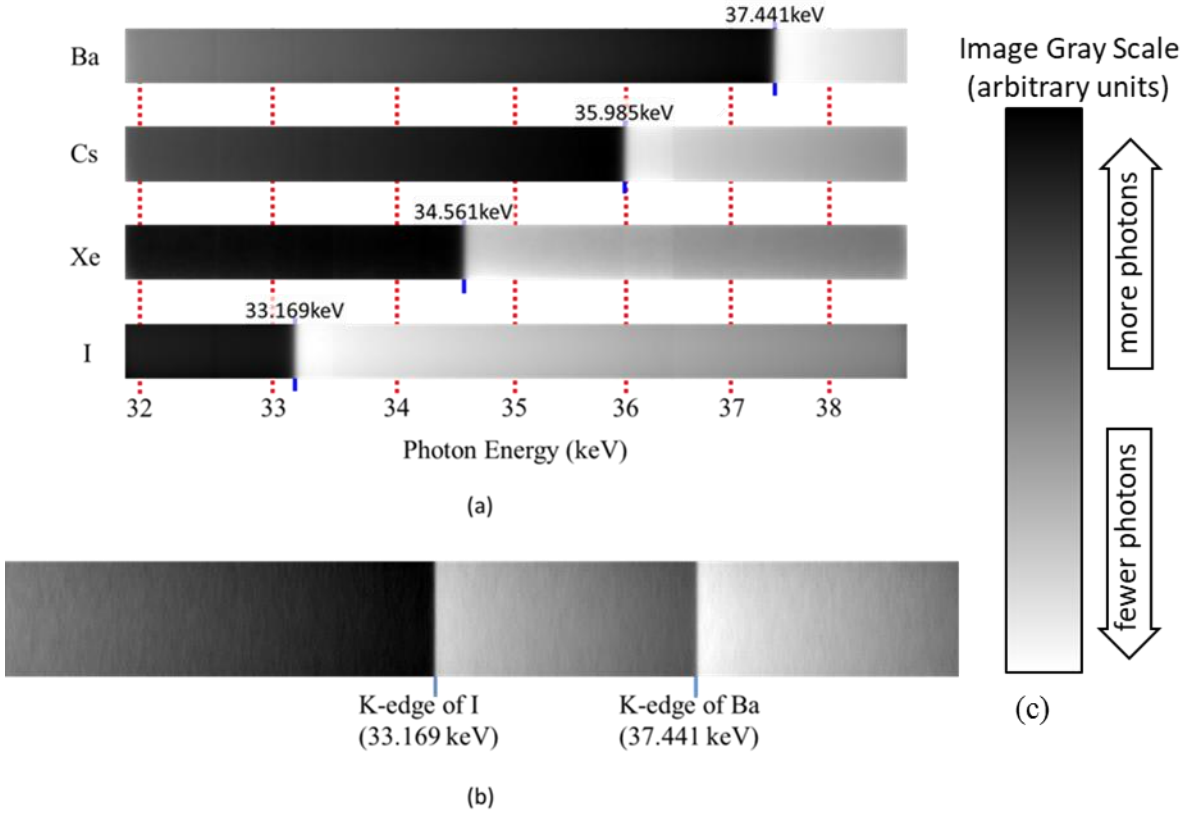

Figure 5.6: (a) Images of the focused beam showing K-edges of all the elements covered for the bold case in table 5.1, and (b) transmission through a mixture of NaI and $BaCl_2$ solution used for energy scale calibration. All images are of solutions of the K-edge element with except for Xe which is a gas. The gray scale on the right (c) shows the relative photon flux detected. The K-edges are clearly visible and show high transmission just before the K-edge energy and the high attenuation just above the K-edge energy. The beam height is 6mm in (a) and (b). **Source**: Ref. [178].

Considering the spectral energy range of the prepared focused beam and the number of K-edges of elements covered, we were interested in seeing the number of materials that can be decomposed including these elements. In our preliminary results [177], we were able to successfully decompose four materials in terms of their projected mass densities (projected mass concentrations). This we achieved using the (1, 1, 1) type reflection, a 0.9 mm focused beam (12 keV energy range), and a 95 cm Si crystal bend radius; Si crystal was bent with a four-bar bender. Figure 5.7a shows the phantom that was imaged and figure 5.7b, the projected concentrations of the four materials decomposed. The phantom consisted of NaI (100 mM), a mixture of NaI and $BaCl_2$, and $BaCl_2$ solutions contained in three polypropylene tubes (Fisherbrand 1050025 cryogenic vials) and a simulated bone material, secured to a 5 mm thick acrylic plate. The measured inner and outer diameters of the polypropylene tubes were 9.6 mm and 11.5 mm, respectively. Some corrections to be noted: (a) in Ref. [178], the concentration of NaI and $BaCl_2$ was mistakenly stated as 0.5 mM each instead of 50 mM as stated in figure 5.7a; and (b) the bent radius of the Si crystal was mistakenly stated as 108 cm instead of 95 cm in Ref. [179].

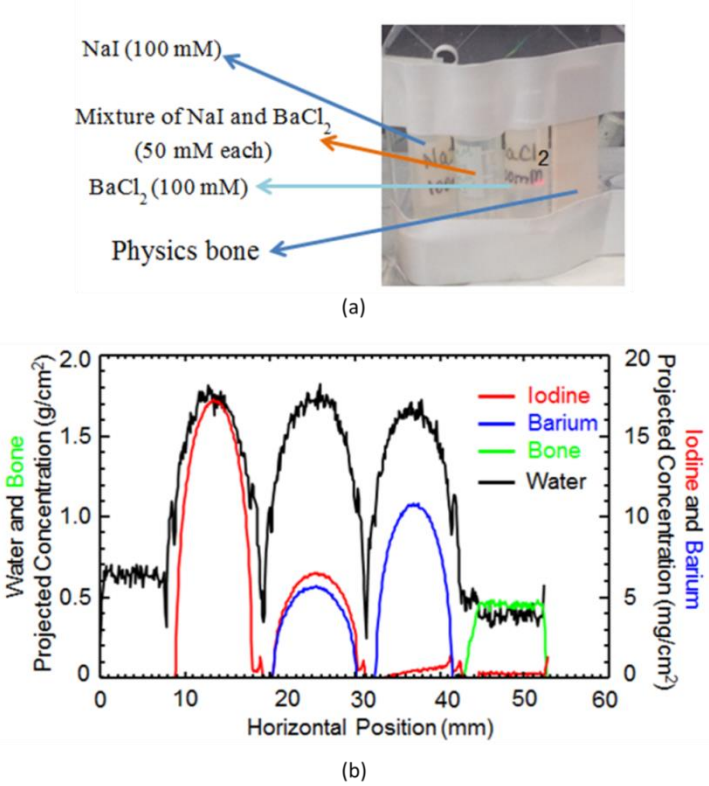

Figure 5.7: (a) Phantom imaged constituting four materials and (b) decomposition of the four materials in terms of their projected concentrations. **Source:** Ref. [177].

Since the K-edges of Xe and Cs were also covered in the spectral energy range of the focused beam, we included Xe and Cs as part of the phantoms imaged in our subsequent experiments. Figure 5.8 shows one of the phantoms imaged that included Xe and Cs. The phantom is made up of six materials: sodium iodide (NaI) solution (15.0 mg/ml or 100 mM); Xe gas (99.999% pure from Praxair Inc. USA); cesium chloride (CsCl) solution (8.4 mg/ml or 50 mM); a mixture of NaI and barium chloride ($BaCl_2$) solutions (15 mg/ml and 20.8 mg/ml or 100 mM each); $BaCl_2$ solution (10.4 mg/ml or 50 mM); and 'physics bone'-simulated bone (hydroxyapatite in an acrylic matrix). For imaging of the phantom shown in figure 5.8, the horizontal scan length was 180 mm at 0.1 mm step, beam dimension incident on the bent Laue Si crystal monochromator was 25 mm (horizontal) by 6 mm (vertical), and the energy range of focused beam was 6.9 keV. We were also successful in decomposing the six materials of the phantom shown in figure 5.8. The result, that is the decomposition of these six materials, is shown in figure 5.9 [178].

Figure 5.8: Phantom imaged constituting of six materials: starting from left to right: NaI, Xe, CsCl, a mixture of $BaCl_2$ and NaI, $BaCl_2$, and 'physics bone'-simulated bone (hydroxyapatite in a plastic matrix). **Source**: Ref. [178].

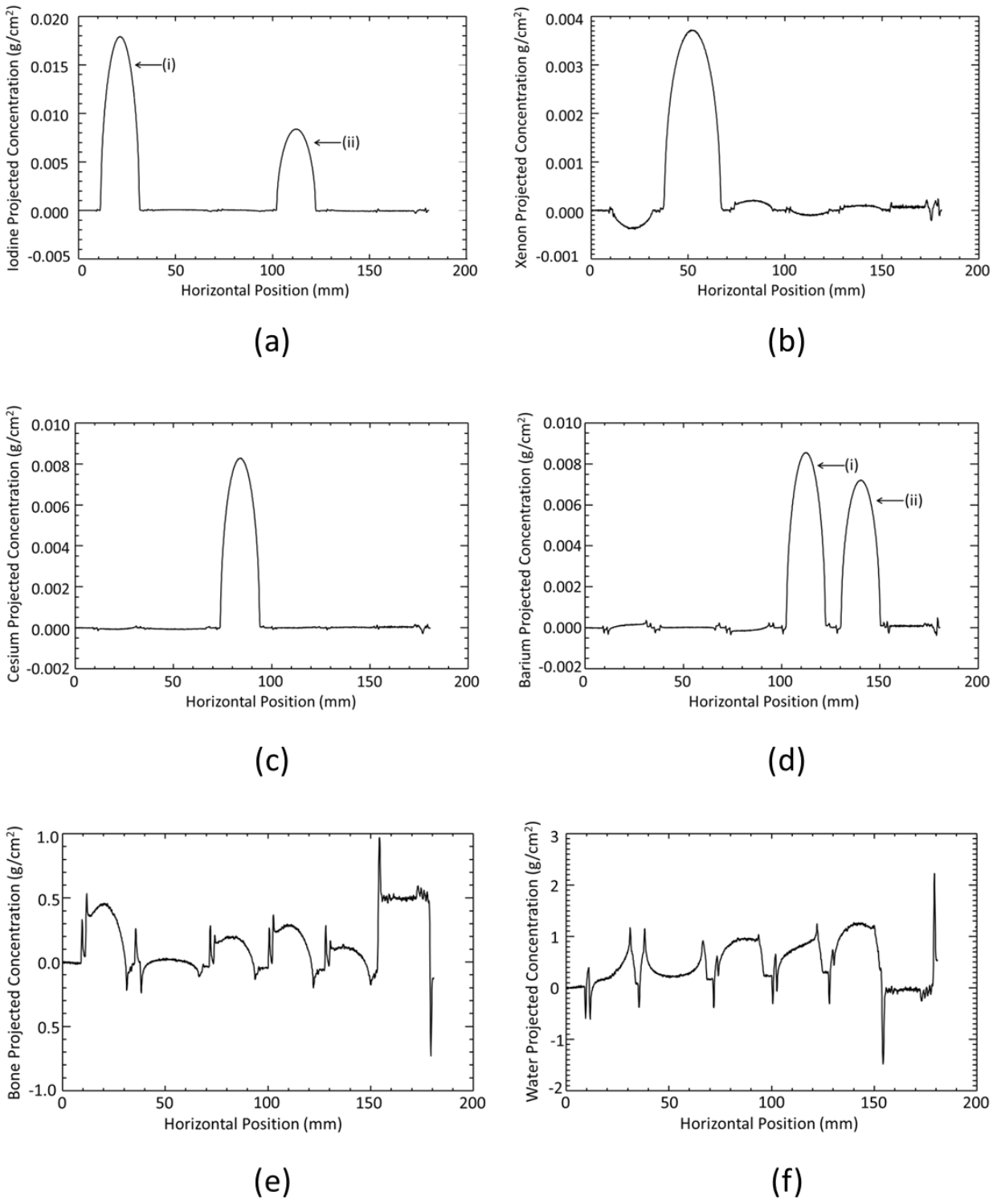

Figure 5.9: Projected concentration (g/cm^2) of six materials decomposed: (a) Iodine from (i) NaI solution, (ii) a mixture of $BaCl_2$ and NaI solutions, (b) Xenon, (c) Cesium, (d) Barium from (i) $BaCl_2$ solution, (ii) a mixture of $BaCl_2$ and NaI solutions, (e) bone, (f) water. The phantom imaged constituting of the six materials is shown in figure 5.8. **Source**: Ref. [178].

The material decomposition algorithm (see Appendix B) used is written in IDL (Interactive Data Language, Exelis Visual Information Solutions, Inc., a subsidiary of Harris Corporation, Boulder CO, USA) and is based on the approach described in Section 4.3 of this thesis. It involves solving for the projected concentrations of the materials from an n x m matrix as given by eqn. 4.4 using the LLSQ method. In our case, the materials projected concentrations $\rho_j t_j$ (1≤ j ≤ m) values obtained are said to be overdetermined because, the number n of x-ray energies from which the r_i (1≤ i ≤ n) measurements are made is greater than the number m of materials projected concentrations solved for. That is, for n > m, $\rho_j t_j$ are overdetermined. Thus, the LLSQ method gives approximate values of the $\rho_j t_j$ [164]. For example, in the six materials decomposition shown in figure 5.9, the number of energies from which the r_i measurements were made was 358.

The arc-tangent features - spikes and slow/gradient background variations that are very pronounced in figures 5.9e and 5.9f are crossover artifacts similar to that which occur with the normal two-beam K-edge subtracting (KES) and Spectral KES imaging [90]. This artifact is addressed in Chapter 6 of this thesis.

5.4 Photon and Dose Rates

Measurements of the photon rate made available by the MEI system for imaging of subjects was done using an air filled ionization chamber (IC Plus 150, FMB Oxford Ltd, Oxford, UK: 150 mm plate length, 18 mm electrode gap, 50 mm plate width). The ionization chamber was placed at the photon beam focal point, and measurements made for different horizontal beam widths incident on the bent crystal Laue monochromator. Figure 5.10 shows the experimental setup. The relationship between the ionization chamber current (i_{ch}) measured and the photon rate ($\dot{N}_0$) is given by eqn. 5.3.

$$\dot{N}_0 = \frac{i_{ch}\varepsilon_{ei}}{q_e E_{ph}\left(\frac{\mu}{\rho}\right)_{EA\,Air}\rho_{ch}L_{ch}} \tag{5.3}$$

Here ϵ_{ei} is the average energy required to produce an electron-ion pair in air (33.4 eV), q_e is the

charge of an electron, E_{ph} is the photon's energy, ρ_{ch} is the density of air, L_{ch} is the ionization chamber's length, $\left(\frac{\mu}{\rho}\right)_{EA\,Air}$ is the energy absorption mass attenuation coefficient of air.

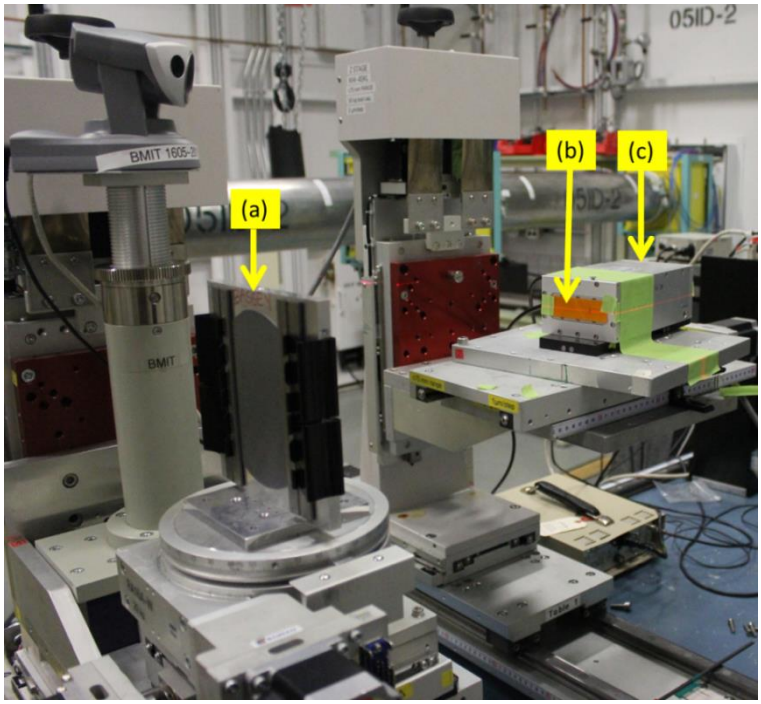

Figure 5.10: Experimental setup for photon rate measurements: (a) Si crystal wafer mounted on a frame bender, (b) a piece of GafChromic RTQA2 film attached to the entrance window of the ionization chamber, and (c) air-filled ionization chamber.

For any medical or biomedical imaging system, the dose delivered to subjects imaged using such a system is considered a serious issue [4, 179]. With the measured photon rate using the ionization chamber, surface dose rate, $\dot{D}_s$ to a subject imaged was estimated using eqn. 5.4.

$$\dot{D}_s = \frac{\dot{N}_0 E_{ph}\left(\frac{\mu}{\rho}\right)_{EATissue}}{A} \tag{5.4}$$

In eqn. 5.4, A is the area of the beam at the point measurement is made and $\left(\frac{\mu}{\rho}\right)_{EATissue}$ is the energy absorption mass attenuation coefficient of tissue. The tissue material is assumed to be water for simplicity. During the photon rate measurements, pieces of GafChromic RTQA2 film

(ISP Technologies Inc., New Jersey, USA) were exposed to the x-rays by placing them at the entrance window of the ionization chamber. The area of the beam (A) in eqn. 5.4 was obtained from the exposed pieces GafChromic RTQA2 film shown in figure 5.11.

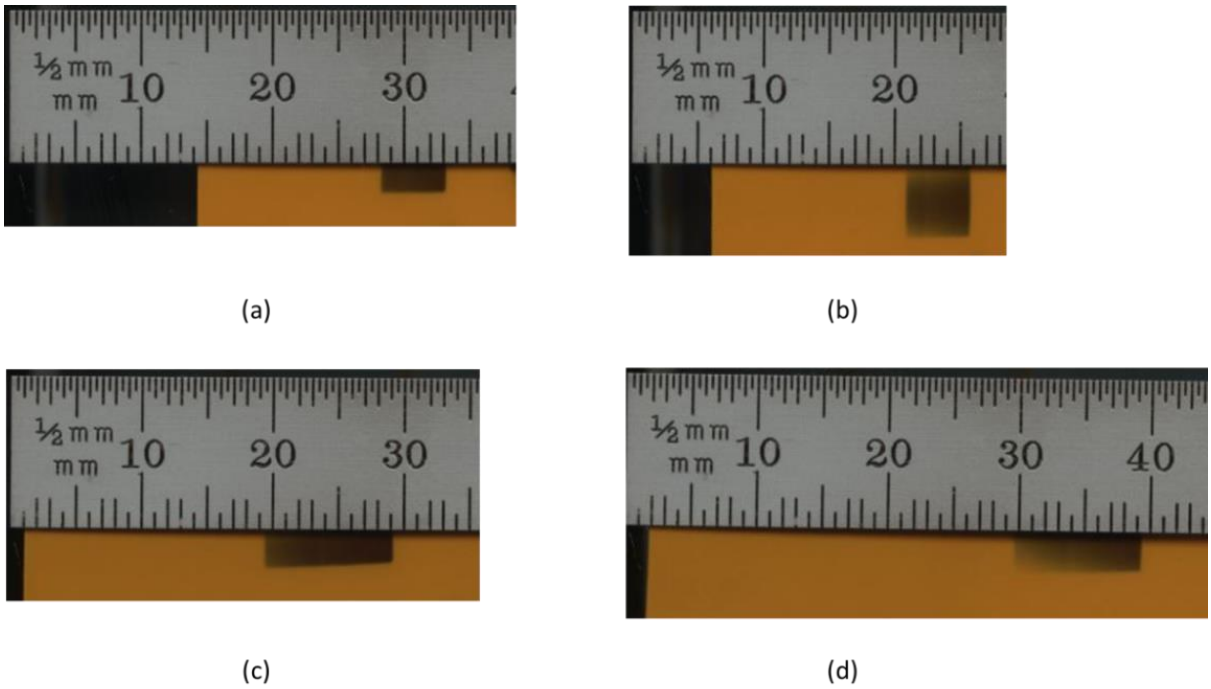

Figure 5.11: Images of the beam from the exposed pieces of GafChromic films that were attached to the ionization chamber entrance window. The corresponding beam size (horizontal x vertical in mm^2) incident on the bent Laue Si crystal was for: (a) 25.0 x 3.0; (b) 25.0 x 6.0; (c) 50.0 x 3.0; and (d) 50.0 x 6.0.

Table 5.2 shows the photon rates available for imaging subjects and the estimated surface dose rates to a subject when imaged using the MEI system. For the same photon rate measurement experimental setup but a flat instead of a bent crystal used, the photon rate for a 50.0 (H) x 6.0 (V) beam size incident on the flat crystal was 5.98 x 10^6 ph/s.

Table 5.2. Results of photon rate measurements and estimated surface dose rates. **Source**: Ref. [179].

Beam size incident on bent crystal H x V (mm^2)	Storage ring current, R_i (mA)	Ionization chamber current, i_{ch} (pA)	i_{ch} (pA) at a R_i of 200 mA	Beam size at focus H x V (mm^2)	Area of beam at focus, A (cm^2)	Photon rate (ph/s) at focus per 200 mA of R_i	Surface dose rate (mGy/s) at focus per 200 mA of R_i
25.0 x 3.0	177.9	950.0	1068.0	5.0 x 3.0	0.16	1.09×10^9	11.8
25.0 x 6.0	177.8	1315.0	1479.2	5.0 x 6.0	0.30	1.50×10^9	8.7
50.0 x 3.0	177.6	3580.0	4031.5	9.5 x 3.0	0.29	4.10×10^9	24.5
50.0 x 6.0	177.8	4800.0	5399.3	9.5 x 6.0	0.57	5.49×10^9	16.7

From Table 5.2, for a bent crystal and for the same beam size of 50.0 (H) x 6.0 (V), the photon rate is 10^3 order of magnitude higher than that of a flat crystal. Given surface dose rate($\dot{D}_s$), the cumulative surface dose D_s can be computed using

$$D_s = \dot{D}_s \frac{h}{v} \tag{5.5}$$

where v is the scan step of subject per exposure time and h is the width of the beam at focus (horizontal beam size) because the subject was scanned horizontally. For imaging of the subject shown in figure 5.8, the beam size, scan step, and image acquisition time (exposure time) for each scan step were 25 mm (H) by 6 mm (V), 0.1 mm, and 6.66 ms, respectively. By using the corresponding $\dot{D}_s$ for a 25 mm (H) by 6 mm (V) beam size from table 5.2, and noting that h is 5 mm, the computed cumulative dose (D_s) to the subject was 2.90 mGy. This dose estimate assumes that there is no time delay between images being acquired by the imaging system and each image was acquired in 6.66 ms intervals. The actual acquisition time between images was approximately 3 seconds, which greatly increased the dose to the subject (~1.3 Gy).

5.5 Sensitivity and Energy Resolution

One of the foreseen potential applications of the developed MEI system is multi-contrast K-edge imaging. Assuming the elements I, Cs, and Ba are to be used as contrast agents in subjects and that their K-edges have been covered, one may ask the question: what are the minimum detectable levels of concentrations of these elements by the MEI system? To answer this

question, phantoms constituting of different concentrations of NaI, CsCl, and $BaCl_2$ solutions, were imaged. The solutions were contained in 1.2 ml centrifuge tubes having an external diameter of 11.5 mm (Corning Incorporated, Corning, NY, USA). Table 5.3 shows the concentrations of these solutions in units of mg/ml and mM while the pictures of the phantoms are shown in figure 5.12. These concentrations were chosen based on what have been used as reported in the Literature [143, 148, 180, 181]. It is emphasised here that the K-edge of Xe is also covered in the spectral energy range of the focused beam prepared by the MEI system. But Xe was not included in the sensitivity study.

Table 5.3. Concentrations of solutions in the phantoms imaged for the sensitivity study.

Solutions	Concentrations			
	A: 0.5 mg/cm^3	**B**: 1.0 mg/cm^3	**C**: 5.0 mg/cm^3	**D**: 10.0 mg/cm^3
	mM	mM	mM	mM
1: NaI	3.3	6.7	33.4	66.7
2: CsCl	3.0	5.9	29.7	59.4
3: $Bacl_2$	2.4	4.8	24.0	48.0

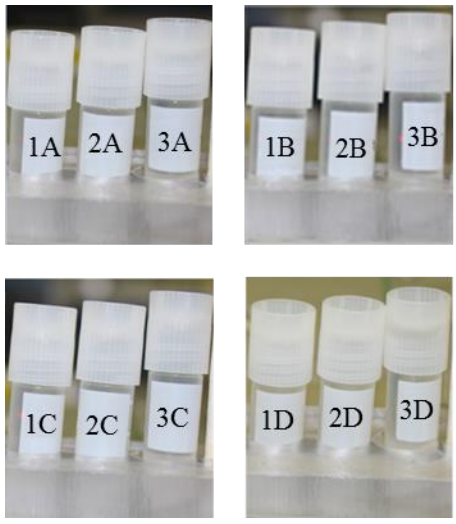

Figure 5.12: Phantom imaged for the sensitivity study: 1, 2 and 3 represent NaCl, CsCl, and $BaCl_2$ solutions, respectively while A, B, C, and D denotes the various concentrations of the solutions as shown in table 5.3.

The MEI sensitivity study results are shown in figures 5.13, 5.14 and 5.15 for iodine, cesium, and barium, respectively. The beam size (horizontal by vertical) incident on the bent

Laue Si crystal monochromator was 25 mm by 6 mm while the focused beam had a minimum energy of 31.57 keV and a maximum energy of 40.09 keV (i.e., a spectral energy range of 8.5 keV). From figures 5.13, 5.14 and 5.15, and as would be expected, the signal size of the MEI system increases with increase in concentration of the solutions imaged. The sensitivity of the MEI system to the detection of cesium is higher compared to iodine and barium. From the results, the minimum level of concentration that the MEI system can detect is 0.5 mg/ml for cesium, and 1.0 mg/ml for iodine and barium. The stated detectable limits were established visually based on the projected concentration plots (figures 5.13, 5.14 and 5.15). Since the flat panel detector associated with the MEI system is position sensitive, visual comparisons of the projected concentrations of each element, at each concentration level, to the background were made. In addition, the contrast-to-noise ratios (CNRs) per mg per cm^2 of projected contrast of these elements were evaluated based on photon counting statistics (Poisson statistics). The CNR in the K-edge image of a contrast agent is considered as one of the ways to quantify the sensitivity to selectively image it [116].

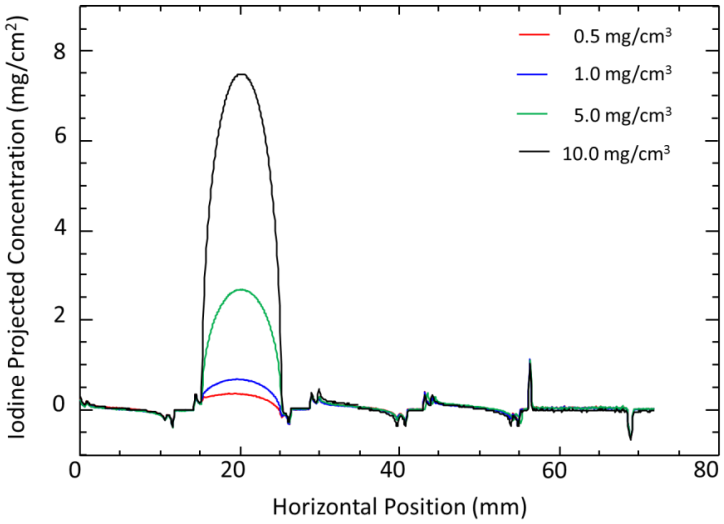

Figure 5.13: Projected concentrations (mg/cm^2) of iodine for different concentrations (mg/cm^3) of NaI solution imaged. **Source**: Ref. [178].

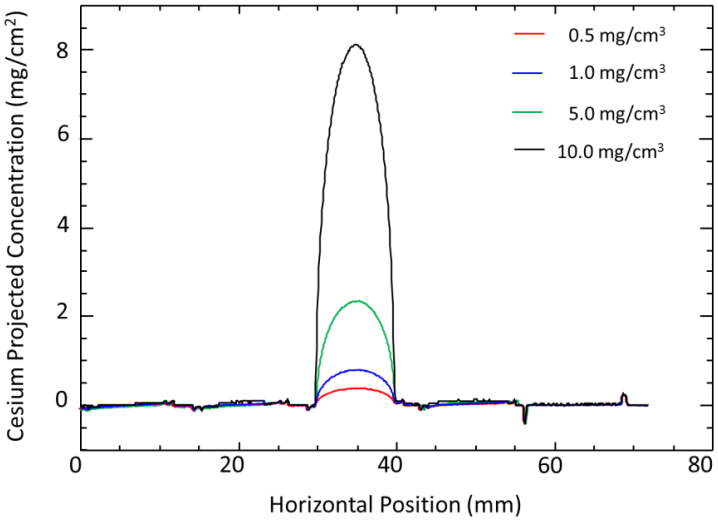

Figure 5.14: Projected concentrations (mg/cm^2) of cesium for different concentrations (mg/cm^3) of CsCl solution imaged. **Source**: Ref. [178].

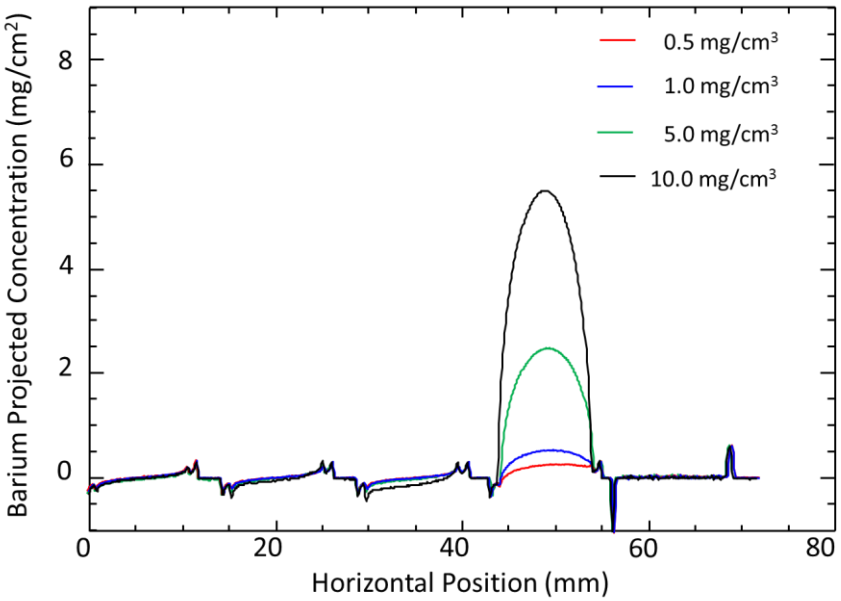

Figure 5.15: Projected concentrations (mg/cm^2) of barium for different concentrations (mg/cm^3) of $BaCl_2$ solution imaged. **Source**: Ref. [178].

The signal-to-noise ratio (SNR) is a measure of the contrast material signal ($\rho_c t_c$) in relation to the noise (measured or calculated) in the image. Therefore, $SNRc = \frac{\rho_c t_c}{\sigma_{\rho_c t_c}}$, which is dimensionless. The contrast-to-noise ratio (CNR) is a measure of the SNR per amount of contrast

material, i.e., $CNRc = \frac{SNRc}{\rho_c t_c} = \frac{1}{\sigma_{\rho_c t_c}}$ and has the units of inverse projected contrast $(g/cm^2)^{-1}$or cm^2/g. For the CNRc evaluations, a modified version of the SNRc (see Appendix C) by Ying Zhu was used [90, 165]. From our evaluations, the CNRs per mg per cm^2 of projected contrast of these elements were 24 for iodine and 23 for cesium and barium. With CNR for iodine being $24/mg/cm^2$, it means that it should be possible to "see" iodine contrast material at about a 0.042 mg/cm^2 projected value. Since we observe sensitivity of iodine at about 1 mg/cm^2 range we are about 24 X away from this possible detectable limit. By assuming Poisson statistics, the crossover artifacts that dominate the image noise and any noise in the detection system have been ignored. That is, the 0.042/mg/cm2 projected value for iodine would be the ultimate detectable limit for the dose we have delivered.

For the MEI system's energy resolution, the energy width was found by taking the K-edge image of the combined iodine and barium solution subject (figure 5.6b). This image was then normalized by the flat image. And the negative logarithm image was taken to linearize the image to represent the combined linear attenuation of the subject arising from the iodine, barium and water. The resulting image (figure 5.6b) clearly shows the absorption edges of the subject at I and Ba K-edges at each vertical pixel. A numerical derivative was taken of the negative logarithm image in the horizontal or energy direction. The sharp transitions of the measured two K-edges resulted in peaks at the two K-edges. A Gaussian fit to the K-edge derivatives for I and Ba was done, which gave a measure of their Gaussian widths (σ). From the measured Gaussian widths, the corresponding FWHM was calculated based on eqn. 5.6 [182].

$$FWHM = 2\sigma\sqrt{In4} = 2\sigma\sqrt{2In2} \tag{5.6}$$

The calculated FWHM at iodine K-edge (33.17 keV) was 48.8 eV and that at barium K-edge (37.44 keV), 36.9 eV. For Cs, its Gaussian width was found by the linear interpolation of I and Ba Gaussian widths, and from which the FWHM at Cs K-edge (35.99 keV) was calculated to be 41.0 eV.

CHAPTER 6

CROSSOVER ARTIFACTS

Images are the end product of any imaging system. Inherent to virtually all medical imaging modalities are image artifacts. An artifact is a feature that appears in an image of a subject but is not present in the subject [183]; it may mask or mimic a clinical feature [184]. Various types of image artifacts have been reported in the literature, the categorization of these artifacts differs for different medical imaging modalities. For example, in computed radiography, image artifacts are categorized into image acquisition artifacts and image-processing artifacts [185]; in digital mammography, the categories are detector-related, machine-related, patient related, processing, and storage-related artifacts [186]. The types of image artifacts that fall under the stated categories can be found in the cited references. Generally, and as observed by Willis et al., (2004), artifacts are classified based on the source (hardware, software or operator), and the mechanism of interference with image acquisition, processing or display. Artifacts in medical images are very undesirable: (1) some have the potential to mimic true disease [187, 188], (2) can reduce image quality, obscure abnormalities and cause interpretation errors [186, 189], (3) may interfere with the diagnostic process [190], and (4) may compromise accurate diagnosis [191, 192]. For some of the established imaging modalities, the types of image artifacts encountered, the causes and methods of reduction or elimination have been well documented. These include computed tomography (CT) [185, 187, 188, 190-192], positron emission tomography/CT [193-195], magnetic resonance imaging [183, 196-198], mammography [199-202], and ultrasonography [203-205].

Imaging systems that prepare focused x-ray beams used for imaging of subjects have a peculiar type of image artifact called “crossover artifact”. This artifact is caused by the crossing of the x-ray beams if the subject is not at the focus or is spatially extended around the focus. Images from the developed MEI system as well as SR-based dual-beam KES and spectral KES systems have this artifact. Generally, for these systems, the subject to be imaged is placed at the SR beam focus. For non-homogeneous samples with high structural features, including biomedical subjects, it is inevitable that some parts of a subject will be upstream, and some, downstream of the focus. The term crossover artifact is used because it occurs when the subject

is upstream or downstream of the beam's focus, hence out of focus. Crossover artifact may also be referred to as the bone artifact [33, 206] as it is prominent in vascular dual energy imaging, and is typically associated with highly absorbing objects, such as bone, traversing the imaging beams. In this chapter, we take a look at crossover artifact-its illustration, modelling, and suppression. Our approach is based on our understanding of this artifact with regards to KES and spectral KES, and thus, we shall start by considering crossover artifacts in these systems.

6.1 Illustrations of Crossover Artifacts

6.1.1. Dual-beam KES

The use of two monochromatic x-ray beams (dual-beam)**,** one with energy above and the other below the K-edge energy of contrast element of interest (dual-energy) to acquire two x-ray images of a target, is the original method developed for implementing KES imaging. Mathematically, measuring the x-ray transmission through the subject at the two energies gives the potential of solving for at least two materials. In the case of KES, it is the sharp absorption discontinuity at the K-edge that gives the sensitivity to the contrast material. A simplified version of the equation that gives the two materials' projected densities is:

$$\rho_C t_C = \frac{r_H - r_L}{\frac{\mu}{\rho}_{CH} - \frac{\mu}{\rho}_{CL}} \tag{6.1a}$$

$$\rho_M t_M = \frac{-\frac{\mu}{\rho}_{CL} r_H + \frac{\mu}{\rho}_{CH} r_L}{\frac{\mu}{\rho}_M \left(\frac{\mu}{\rho}_{CH} - \frac{\mu}{\rho}_{CL}\right)} \tag{6.1b}$$

where $\rho_C t_C$ and $\rho_M t_M$ are the projected mass densities of the contrast (C) and matrix (M) materials, respectively. For biological subjects, water is commonly chosen to be the matrix material. The r_H and r_L are the negative logarithm, incident beam normalized transmission values for the above edge (H) and below edge (L) beams defined by:

$$r_H = -ln\left(\frac{N_H}{N_{0H}}\right) \tag{6.2a}$$

$$r_L = -ln\left(\frac{N_L}{N_{0L}}\right) \tag{6.2b}$$

where the N_H, N_L are the detected transmitted beam through the subject and N_{0H}, N_{0L} are the corresponding incident beam values. Also, in eqns. 6.1a and 6.1b the mass attenuation coefficients for the contrast and matrix materials are present for the high and low energy beams

(contrast: $\frac{\mu}{\rho_{CH}}$, $\frac{\mu}{\rho_{CL}}$; matrix: $\frac{\mu}{\rho_{MH}}$, $\frac{\mu}{\rho_{ML}}$). Usually, the difference between the attenuation coefficients for the matrix material is very small for the closely spaced energies and, it is replaced by the average value, $\frac{\mu}{\rho_M}$. Inspection of eqn. 6.1a shows that there is a difference between the two measured beams at the two energies around the K-edge. Thus, any imbalance between them will result in a perceived presence of contrast material (positive projected contrast if $r_H > r_L$, and negative if $r_H < r_L$. This is the mathematical origin of the crossover artifact.

Dual-beam KES imaging systems vary at different SR facilities, and so does the means by which the two monochromatic x-ray beams are prepared. For the KES application to human coronary angiography at the Stanford Synchrotron Radiation Laboratory (SSRL) and initially at the National Synchrotron Light Source (NSLS), two asymmetrically cut silicon (Si) crystals, Si(1,1,1), are used to divide the SR beam into the two required x-ray beams [207]. The two beams are then adjusted to cross over at the position of the target to be imaged. At the NSLS biomedical beamline and the European Synchrotron Radiation Facility (ESRF) ID 17 beamline, a single bent Laue crystal Si (111) monochromator and a splitter are used to prepare the two x-ray beams [85, 97]. A KES imaging setup similar to that applied to lung imaging at ESRF ID 17 beamline is shown in figure 6.1 [97].

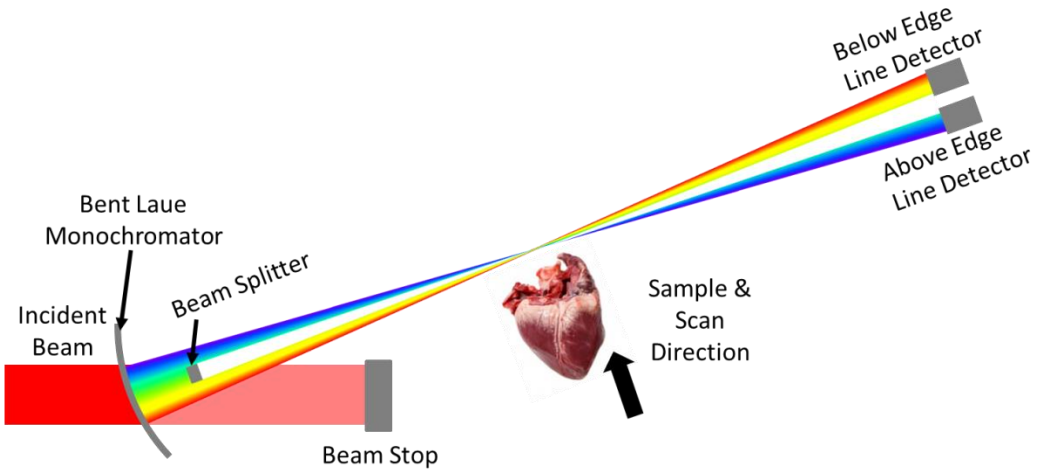

Figure 6.1: Dual-beam KES imaging setup similar to that applied to lung imaging at ESRF ID 17 beamline.

The physical cause of crossover artifact in dual-beam KES imaging is illustrated in figure 6.2. As with a number of SR imaging systems, the imaging of a target is done in line scan mode where the target is scanned vertically through the line beam, which is focused in the case of KES. In figure 6.2, as an absorbing subject traverses the two imaging beams vertically at a location away from the beam's focus, one beam will be eclipsed before the other. Due to the low energy beam being traversed before the high energy beam, there will be a reduction in the low energy beam values in the low energy image spatially displaced from the same location in the high energy image. This causes an imbalance between r_H and r_L as earlier stated. Even if the subject is not traversing the beam vertically but is stationary while being imaged, for example in the acquisition of a projection in computed tomography, the imbalance will still exist except at the beam's focus. During KES processing, the loss of low energy beam values where the high energy beam remains high will result in a calculated negative contrast value. Conversely, the loss of high energy beam when low energy beam remains high will result in a positive contrast value. Thus, a highly absorbing feature, such as a bone, traversing the two beams at a location other than the focus will result in a shadow type artifact where one side of the subject along the scan direction will have an artificial contrast value and the other side will have the opposite contrast value. This is what is being referred to as a "crossover artifact". Examples of dual-beam KES images are shown in figures 6.3 and 6.4 [96, 208]. The crossover artifacts in these images are indicated with black and white pointers.

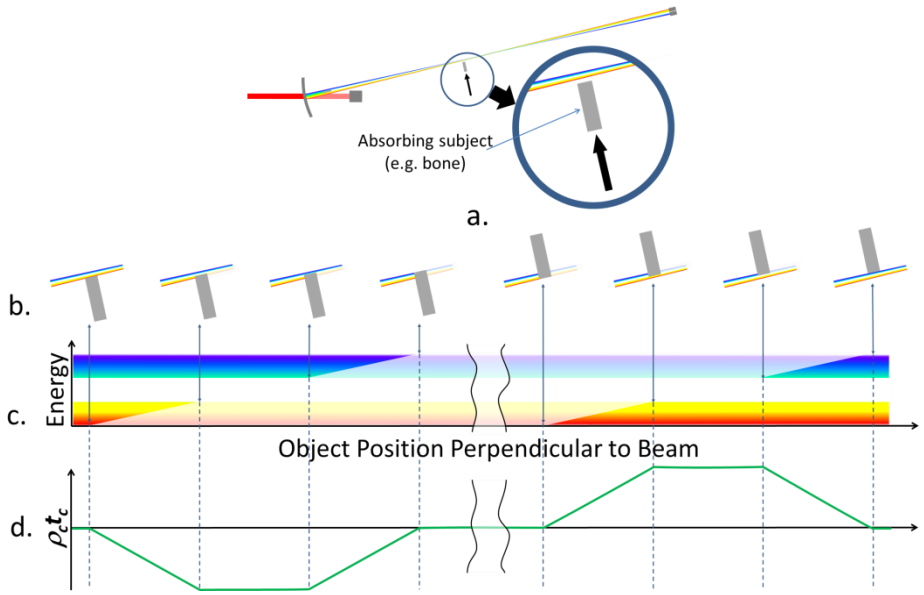

Figure 6.2: Illustration of the cause of crossover artifact in dual-beam KES: (a) an absorbing subject (i.e. bone) going through the beams from below before the beam's focus; (b) the subject progressively attenuates each beam as it moves up, the low energy beam being attenuated first before the focus; (c) as the subject leaves the high energy beam, the opposite occurs; (d) The attenuation of one beam (either the low or high energy beam) before the other by the subject gives the appearance of the contrast agent (e.g. iodine) as positive or negative depending on which beam is attenuated first. For the case shown, attenuating the low energy beam first creates negative projected iodine and then positive projected iodine later as the subject leaves the beam.

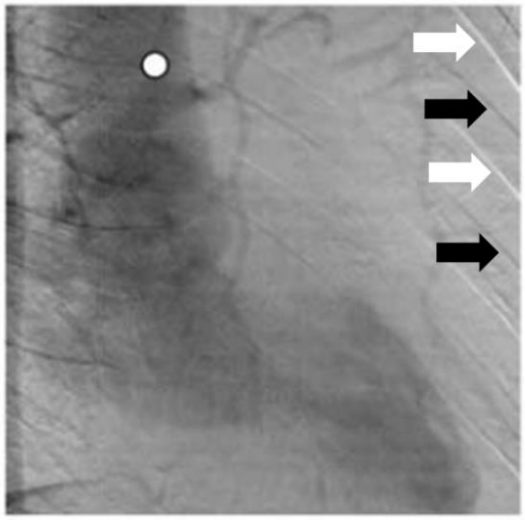

Figure 6.3: Dual-beam KES image of a human aorta acquired using iodine as the contrast agent. The black and white pointers indicate the positive and negative crossover artifacts, respectively in the image. **Source:** Ref. [208].

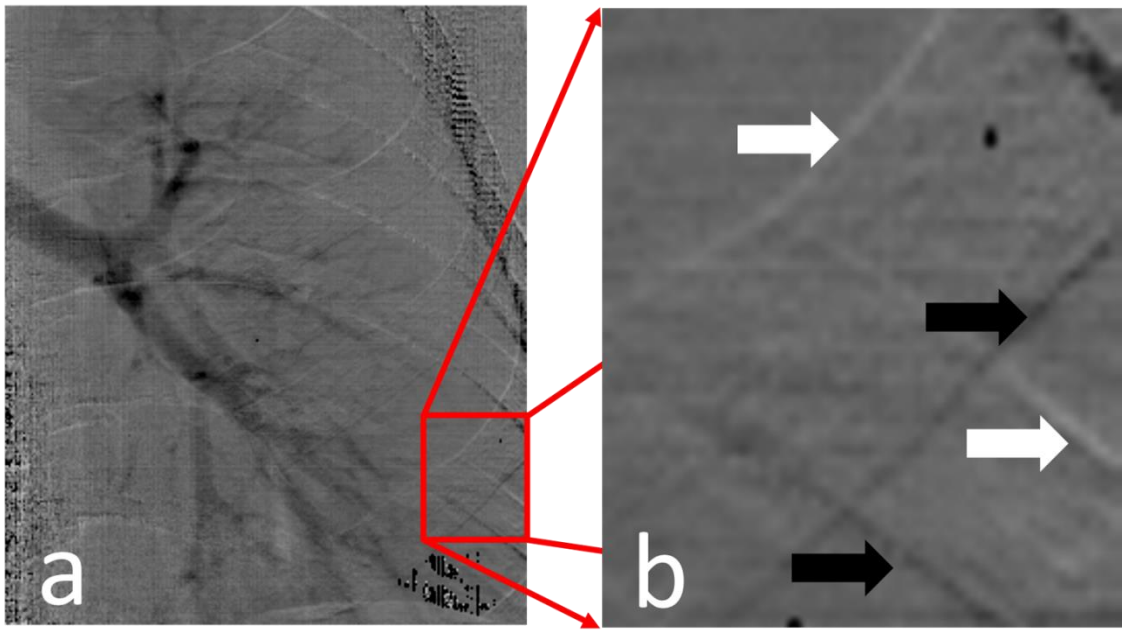

Figure 6.4: Dual-beam KES image of the right lung of a normal human subject acquired using xenon as the contrast agent (Xenon bronchogram). The black and white pointers indicate the positive and negative crossover artifacts, respectively in the image. **Source:** Ref. [96].

An absorbing subject traversing the two separated beams is the origin of the crossover artefact. The fact that the two beams are spatially displaced along the scan direction and that the contrast image is a difference type (subtraction) image gives rise to a derivative type artefact. To understand the scale of the artifact, let's assume that a flat plate of matrix material ($\frac{\mu}{\rho}_M, \rho_M,$ & t_M) with NO contrast material present is scanned through the imaging beams at a location away from the focus. Also, it is assumed that there is little or no difference between the high and low energy matrix attenuation coefficient ($\frac{\mu}{\rho}_{MH} = \frac{\mu}{\rho}_{ML} = \frac{\mu}{\rho}_M$). By inspection of the form of the contrast image equation, i.e. eqn. 6.1, the maximum contrast artifact or error will occur when one of the beams is attenuated by the plate before the other. Again, let's assume that the flat plate attenuates the high energy beam first. In that instance, the value of r_H and r_L can be calculated and the maximum contrast artifact assessed.

$$r_H = \frac{\mu}{\rho}_M \rho_M t_M \quad and \quad r_L = 0 \tag{6.3}$$

In eqn. 6.3, r_L is zero because the plate has not entered the low energy beam and thus the thickness is zero. The contrast error, $\rho_C' t_C'$, is then:

$$\rho_C' t_C' = \frac{r_H - r_L}{\frac{\mu}{\rho_{CH}} - \frac{\mu}{\rho_{CL}}} = \frac{\frac{\mu}{\rho_M}}{\Delta\frac{\mu}{\rho_C}} \rho_M t_M \tag{6.4}$$

Where the contrast material K-edge jump, $\frac{\mu}{\rho_{CH}} - \frac{\mu}{\rho_{CL}}$, has been replaced by $\Delta\frac{\mu}{\rho_C}$. It is a simple matter to show that if the plate enters the low energy beam first, then the contrast error is negative. Also, is should be clear as the plate enters the beams away from the focus that the error increases linearly to the maximum shown in eqn. 6.4. Once the plate is in between the two beams, it plateaus at the maximum value. Once it begins to enter the other beam, it will then linearly decrease to zero when both beams are passing through the plate. The shape of the artifact for other object profiles is somewhat more difficult to predict, but this can be easily modeled (see Section 6.3 of this thesis). Also, the shape will retain the derivative type behavior due to the difference in the equation between the two spatially displaced "*r*" values. A similar analysis can be applied to the matrix material images of eqn. 6.1b to arrive at the artifact for the $\rho_M' t_M'$ image. In this case, it matters which beam is being attenuated first (high energy beam first, then low energy beam- eqn. 6.5a; or low energy beam first, then high energy beam- eqn. 6.5b.

$$\rho_M' t_M'^{\,H\to L} = -\frac{\frac{\mu}{\rho_{CL}}}{\Delta\frac{\mu}{\rho_C}} \rho_M t_M \tag{6.5a}$$

$$\rho_M' t_M'^{\,L\to H} = \frac{\frac{\mu}{\rho_{CH}}}{\Delta\frac{\mu}{\rho_C}} \rho_M t_M \tag{6.5b}$$

6.1.2. Spectral-beam KES

Spectral-KES [90] is a novel and 'simple' method of performing KES developed at the BMIT BM beamline. This imaging method was discussed and its schematic diagram presented in the Section 3.2.1 of this thesis. Spectral-KES has been performed in both projection and CT modes using iodine, barium, and xenon as contrast elements [90, 98, 174]. A simplified version of the equation that can be used to extract the projected mass density value of the contrast material is given by eqn. 6.6.

$$\rho_C t_C = \frac{\frac{2}{N}\left(\Sigma_{i<\frac{N}{2}} r_i - \Sigma_{i>\frac{N}{2}} r_i\right)}{\frac{\mu}{\rho_{CH}} - \frac{\mu}{\rho_{CL}}} \tag{6.6}$$

where N is the number of energies measured across the incident beam spectrum. It is assumed that the K-edge occurs at the middle energy location (N/2) and the corresponding negative logarithm values are summed above (i<N/2) or below (i>N/2) that index (N/2) or K-edge value. Again, the mass attenuation coefficients, $\frac{\mu}{\rho_{CH}}$ and $\frac{\mu}{\rho_{CL}}$, are the average values for the above and below K-edge spectral energy ranges. As in eqn. 6.1a, the spectral KES contrast image is a logarithmic difference of images above and below the K-edge. However, it is complicated by the sums.

The crossover artifact in spectral-KES occurs in a manner like its occurrence in dual-beam KES. Let's assume that a flat plate enters the beam away from the focal point in a manner similar to the discussion for the crossover artifact in the KES section. Let's assume that the plate enters the high energy beam first ($i < \frac{N}{2}$), and is advanced to the K-edge location or beam index $i = \frac{N}{2}$. In that instance, the value of $r_{i<\frac{N}{2}}$ and $r_{i>\frac{N}{2}}$ are easily evaluated and the crossover artifact for the contrast material can be assessed.

$$r_i = \frac{\mu}{\rho_M}\rho_M t_M \; for \; i < \frac{N}{2} \;\; and \;\; r_i = 0 \; for \; i > \frac{N}{2} \tag{6.7}$$

In eqn. 6.3, r_L is zero because the plate has not entered any beam and thus the thickness is zero. The contrast error, $\acute{\rho_C}\acute{t_C}$, is then:

$$\acute{\rho_C}\acute{t_C} = \frac{\frac{2}{N}\left(\Sigma_{i<\frac{N}{2}} r_i - \Sigma_{i>\frac{N}{2}} r_i\right)}{\Delta\frac{\mu}{\rho_C}} = \frac{\frac{\mu}{\rho_M}}{\Delta\frac{\mu}{\rho_C}}\rho_M t_M \tag{6.8}$$

which is the same maximum error as in the case of KES. Also, as in KES, if the plate enters the low energy beam first, then the contrast error is negative. It is a simple matter to show that the matrix material artifact or error is the same as in the case of KES as given in eqns. 6.5a and 6.5b.

One subtle difference is that in the case of spectral KES, there is not a plateau of the error as the object moves across the region between the high and low energy beams. In spectral KES, as the object crosses the K-edge location, the error linearly decreases until it exits the full beam size. Thus, the artifact for the plate is triangular in shape rather than trapezoidal as is in the case for KES and is as illustrated in figure 6.5. The dashed lines represent dual-beam KES crossover artifact, it is shown so as to give a visual comparison of the magnitude of crossover artifact

between dual-beam KES and spectral KES. In figure 6.5, the width of the artifact for KES and spectral KES along the object scan direction is given by the size of the beam away from the focus location. This width is given by the angular divergence of the beam multiplied by the distance from the focus. This angle is typically a few milliradians, but depends on the imaging geometry (specifically the crystal bend radius and incident beam height). Assuming KES and spectral KES have the same geometry, then the width and the magnitude of the crossover artifact will be the same for the case of a flat plate. This is shown graphically in figure 6.5.

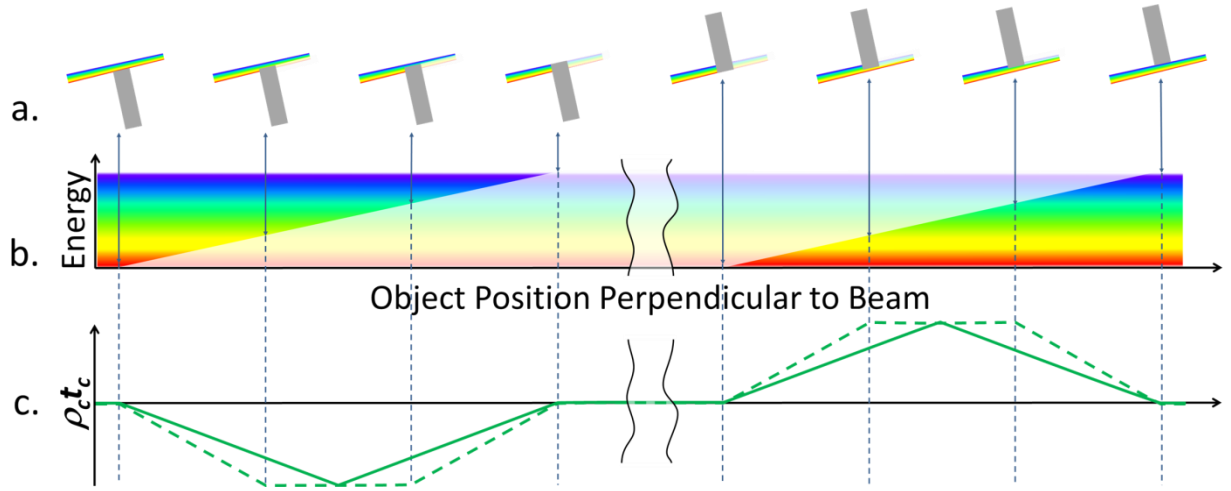

Figure 6.5: Illustration of cause of crossover artifact in Spectral-KES.

The Novel MEI system we have developed [178] can be used to perform multiple KES imaging. In both the MEI and spectral KES systems, a critical component is the bent Laue single Si crystal monochromator. But, in the spectral-KES system the monochromator focuses the beam in the vertical plane whereas in the MEI system, the beam is focused in the horizontal plane. Another major difference between these two systems is that imaging with the spectral-KES system can be performed in either projection or CT mode, but only in projection mode with the MEI system. Considering the plane (vertical or horizontal) that the beam is focused, the beam size of BMIT BM beamline (horizontal by vertical: 240 mm by 7 mm at a source-to-sample distance of 23 m) is partly responsible for the spectral energy range covered by the systems. For the spectral-KES system, the spectral energy range is about 550 eV, and up to 15 keV for the MEI system. The projected concentration plot of barium from a six-component phantom (figure 6.6a) imaged using the MEI system is shown in figure 6.6b. The phantom imaged, as shown in

figure 6.6b, is constituted of, starting from left to right: NaI solution (100 mM), Xe gas (99.999% pure), CsCl solution (50 mM), a mixture of NaI and $BaCl_2$ solutions (each 50 mM), $BaCl_2$ (50 mM), and 'Physics bone'. The NaI, CsCl, mixture of NaI and $BaCl_2$, and $BaCl_2$ solutions were each contained in a 5.0 mL tube with internal diameter (ID) of 9.6 mm and outer diameter (OD) of 11.9 mm. For the 15 mL tube that contained Xe gas, the ID and OD were 14.5 mm and 16.0 mm, respectively. The arc-tangent features in figure 6.6b are caused by crossover artifact.

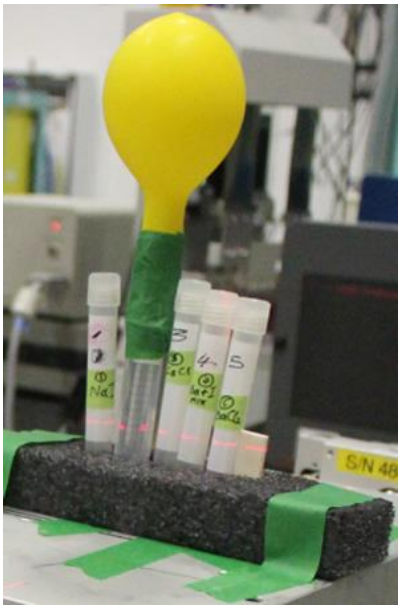

Figure 6.6a: A six-component phantom imaged using the MEI system.

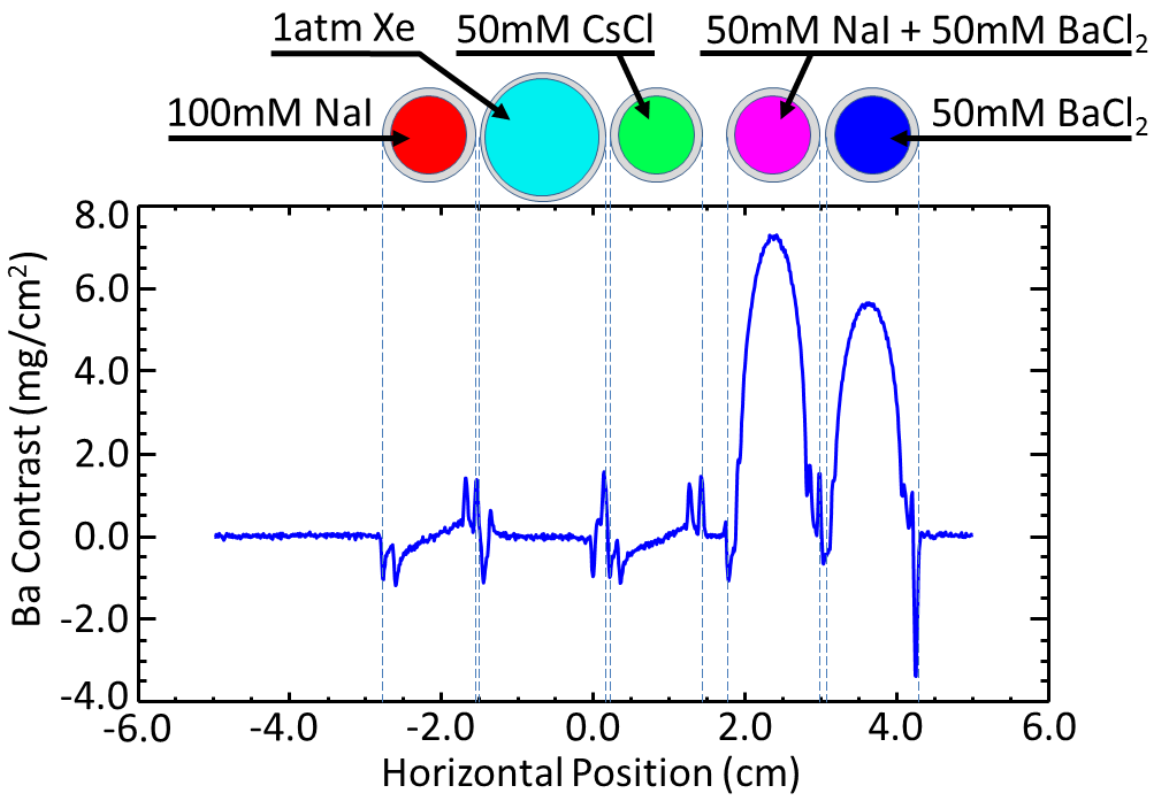

Figure 6.6b: Projected concentration plot of barium from a phantom imaged using the MEI system.

The very wide energy range of the MEI system presents an extreme version of the crossover artifact. This is because the wide energy range comes at the expense of a wide range of Bragg angles from the bent Laue crystal. Due to this wide energy range and the possible crossing of several K-edges, the mathematics are somewhat complex, but the same principles discussed on dual-beam KES above still apply. For this reason, the crossover artifact for spectral KES and MEI were modelled because the "simplified" mathematics is no longer helpful in understanding the behavior of the artifact observed.

6.2 Modelling of Crossover Artifacts

A computer model of various objects crossing focused x-ray beams before, at, and after the beam's focal point for KES, spectral KES and MEI was developed (see Appendix D). The objects modelled are a plate, a solid rod, and a tube with provisions made to accommodate things that may be inside the tube. The model accounts for the spectral energy range of the beams, the

energy dependence of the objects, various materials, and the trajectory that each beam takes in traversing the objects. One assumption is that the beam focuses completely at the focal point. For simplicity, it is also assumed that there are several unique energies represented by rays that span the energy range. In the real system, there would be a narrow bundle of rays through the object into each detector pixel. The narrow angular range of this bundle would have a matching small energy range which in the model would be represented by a single ray with an average energy for that bundle. As in the experimental situation, the object is scanned along the y direction (figure 3.11-spectral KES system) or x direction (figure 5.2-MEI system) in quantized increments through the beam resulting in a projection image of the object. The objects modeled (plate, rod, and tube) are assumed to have uniform behavior along the out of plane direction, i.e., x direction for spectral KES or y direction for MEI as shown in figures 3.11 and 5.2, respectively. The composition of the plate, rod, tube (both the shell and the contents) can be practically any element or combination of elements in the periodic table (Z = 1 to 100). Most of the modelling is done for water, some forms of plastic, contrast solutions, bone and soft tissue in order to represent real biological targets. All of the modelling was done using IDL software (Interactive Data Language, Exelis Visual Information Solutions, Inc., a subsidiary of Harris Corporation, Boulder CO, USA). Examples of the model are given in figures 6.7 and 6.8. Figure 6.7 shows a crossover artifact arising from a 1 mm thick flat Lucite plate traversing the imaging beam. The solid line in both figures 6.7a and 6.7b is for spectral KES and the dashed line (though not visible in figure 6.7a) for two beam KES. Figures 6.7a and 6.7b show that there is no crossover artifact when the plate is placed at the beam's focus. The crossover artifact is clearly visible and resembles what has been shown schematically in figures 6.2 and 6.5. The model shows the trapezoidal behavior of the crossover artifact as projected mass density ($\acute{\rho_C} \acute{t_C}$) in KES when the object enters the beam upstream of focus (as in figures 6.2d and 6.5c) and the triangular behavior in spectral KES (as in figure 6.5c). Again, it is interesting to note that the magnitude (maximum and minimum excursion) of the artifact is the same for KES and spectral KES; however, the width of the artifact for spectral KES is narrower because of the triangular behavior. This is the behavior predicted and graphically depicted earlier for in eqns. 6.4, 6.5a, 6.5b, 6.8, and figure 6.5. To confirm these equations and help validate the model, the scale of the artifact predicted by the model can be compared to the results from the above equations. For this

we need some estimated values for the attenuations coefficients of common contrast and matrix materials. These are given in Table 6.1.

Table 6.1. The K-edge energies of some contrast materials and their mass attenuation coefficients 0.1 keV below (E_L) and 0.1 keV above (E_H) the K-edges, K-edge attenuation jumps ($\Delta\mu/\rho_C$), and the average mass attenuation values for water (μ/ρ_W) and bone (μ/ρ_B) at the K-edge energies. The source of the values shown in the table is Ref. [121].

Contrast Material	E_K [keV]	$\mu/\rho_C(E_L)$ [cm^2/g]	$\mu/\rho_C(E_H)$ [cm^2/g]	$\Delta\mu/\rho_C$ [cm^2/g]	μ/ρ_W [cm^2/g]	μ/ρ_B [cm^2/g]
Iodine	33.169	6.553	35.563	29.010	0.324	0.764
Xenon	34.561	6.138	33.002	26.864	0.309	0.697
Cesium	35.985	5.888	31.109	25.221	0.295	0.639
Barium	37.441	5.520	28.890	23.369	0.284	0.587

Equation 6.4 can be used to estimate the artifact for the case of a flat plate shown in figure 6.7b. Using these equations and the attenuation coefficients for iodine and water from Table 6.1, the error is ± 1.12 mg/cm^2. From the modeling program that created figure 6.7b the calculated error was ± 1.10 mg/cm^2. Similarly, eqns. 6.5a and 6.5b can be used to estimate the error for figure 6.7d for the matrix or water material, which is comparable to that of the model (shown in parenthesis). The errors were found to be 23 mg/cm^2 (22 mg/cm^2) for the left side of the object (H->L) and -126 mg/cm^2 (-121 mg/cm^2) for the right side of the object (L->H). The modeling program can be used to predict the artifacts from wide energy range imaging, MEI. Figure 6.8 shows the MEI crossover artifact model of an iodine solution (15 mg/cm^3) contained in a tube placed at focus (figure 6.8a) and 5 cm upstream of focus (figure 6.8b). The images represent the projected iodine contrast. Note the derivative like behavior of the tube displaced from the focus, which is due to the imbalance between r_H and r_L. In the case of MEI, the simple equations used for KES and spectral KES are not as useful in predicting the scale of the error, however, similar behavior is found as has been expected.

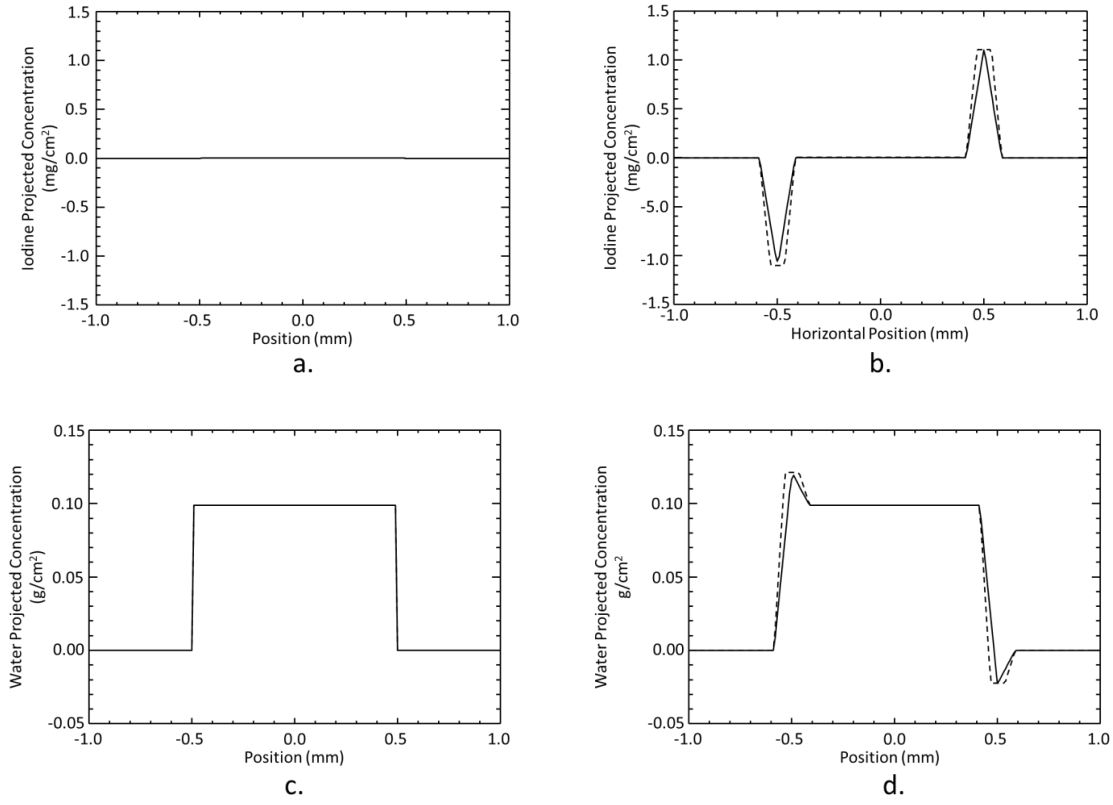

Figure 6.7: KES (broken lines) and Spectral-KES (solid line) crossover artifact models of a plate placed at (**a.**, **c**.) the beam's focus and (**b**., **d**.) 5.0 cm upstream of the beam's focus, that is, 0.0 cm and -5.0 cm offsets, respectively. As observed in **a.** and **c.**, there is no crossover artifact when the plate is placed at the beam's focus. The plate is made up of Lucite material, thickness and height of plate is 1.0 mm.

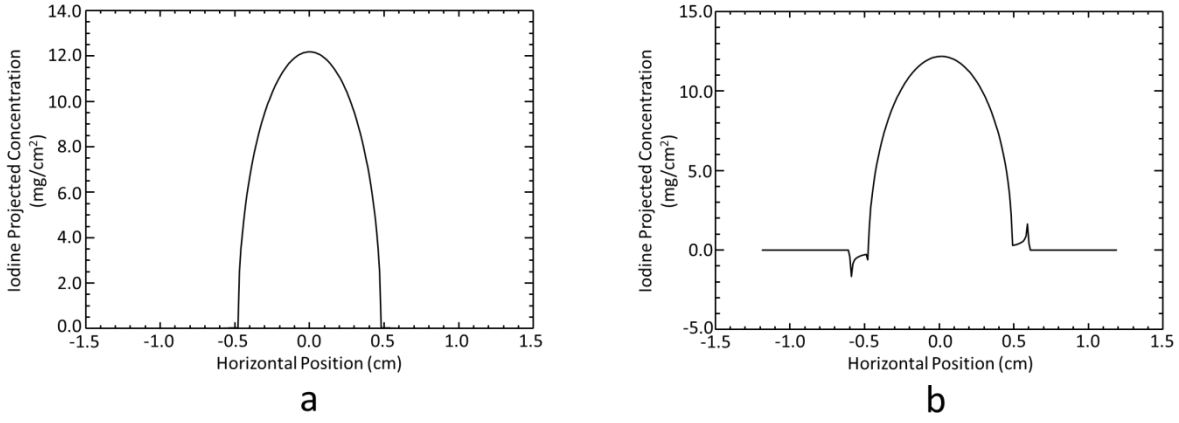

Figure 6.8. MEI crossover artifact model of a tube containing 15.0 mg/cm^3 of NaI solution and water: offset of 0.0 cm (a); offset of -5.0 cm (b). Tube material is Lucite, the inner and outer diameters of tube are 9.60 mm and 11.9 mm, respectively.

6.3 Suppression of Crossover Artifacts

The origin of the artifact is well understood both by modelling and mathematically. From inspection of figure 6.2, showing the case for KES, it can be easily seen that the high and low energy images are displaced by an amount along the scan direction (y, similar to that shown in figure 3.11 as the subject traverses the beam away from the focal point along the x-direction. The y displacement can be easily corrected in a computer to arrive at an image that visually reduces the artifact. This simple manipulation is normally done by all of the research groups that perform KES (whether acknowledged in publications or not) to minimize crossover artifact which in living subjects usually occurs with bone. Figure 6.9a shows the shifting of two images in KES relative to each other along with the energy content of the beam with the object traversing the beam upstream of focus. These have the effect of translating and aligning the two energy-position parallelepipeds over each other. Due to the finite extent of a target along the x direction, a complete crossover correction is impossible; a "minimum artifact" image was usually created. A mathematical solution to the crossover correction would remove the subjective aspect of manually adjusting the two images. Since the crossover artifact increases the derivative-like structure in the contrast image, an image with minimal structure is most likely the closest to a crossover artifact free image. The standard deviation of the contrast image is a metric of structure in the image. It should be noted that other solutions could be arrived at by using other matrices. Suppose a set of contrast images are created as a function of relative shift between the images, the standard deviation of each of these images can be determined and minimized to find the optimal shift value. This is what has been done in our study for KES and in a similar fashion for spectral KES and MEI. Figure 6.9b shows the effect of aligning all of the spectral content of the beam so that the subject appears to traverse the entire spectrum at one location. This has the effect of converting the energy - position parallelepiped into a rectangle.

As shown in the spectral KES figure (figure 6.5), the object eclipses each energy at successively different y values when the object is away from focus. Now, the situation is more complex where a correction using multiple shifts as a function of energy is needed across the full energy range of the beam. The situation is similar to a stack of playing cards that have been shifted transversely along the stacking direction. Mathematically, then the "fix" is to straighten the stack. This will make the data appear to be taken at the focus. In the program each X-E plane is shifted relative to a reference plane (usually the middle plane in the E direction) until the

standard deviation of the calculated contrast image between the two planes, using the KES algorithm, is minimized. This forces the alignment of the two planes. The alignment is then done to all planes in the X-E-Y data set. Once aligned, the spectral KES algorithm is then applied, and the result is a near "crossover artifact free" image of the contrast material(s) and matrix material(s).

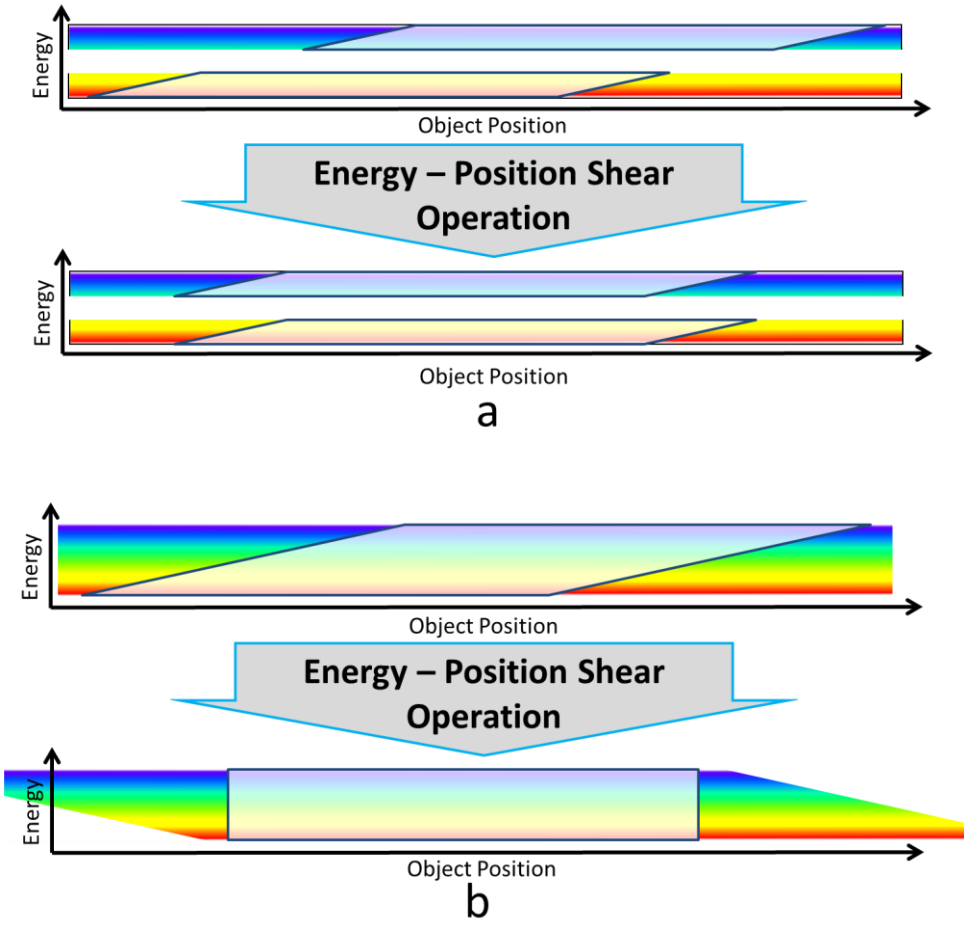

Figure 6.9: Illustration of crossover artifact reduction in (a) KES and (b) Spectral-KES.

From the above understanding, programs in IDL were written to reduce the crossover artifact (see Appendix E) for all the cases considered in this paper: KES, spectral-KES and MEI crossover artifact models for rod, plate and tube. The written programs were then applied to suppress modeled crossover artifact, and crossover artifact present in images from experimental data. In figure 6.10, the reduction of MEI modeled crossover artifact of a tube and rod is shown.

The ID and OD of the tube were 9.60 mm and 11.9 mm, respectively, and contained 15.0 mg/cm^3 of NaI solution. The rod had an outer diameter of 25.0 mm. Both the tube and rod were made of Lucite material. The modeled artifact was based on an offset of -5.0 cm, that is, the tube and the rod were each placed 5.0 cm upstream of the beam's focus. Figures 6.11a-ii, 6.11b-ii and 6.12a- to 6.12f-ii show the suppressions of crossover artifact in images and projected concentration plots from experimental data obtained using the spectral KES and MEI systems, respectively. The suppressions were done using the crossover artifact reduction algorithm shown in Appendix E.

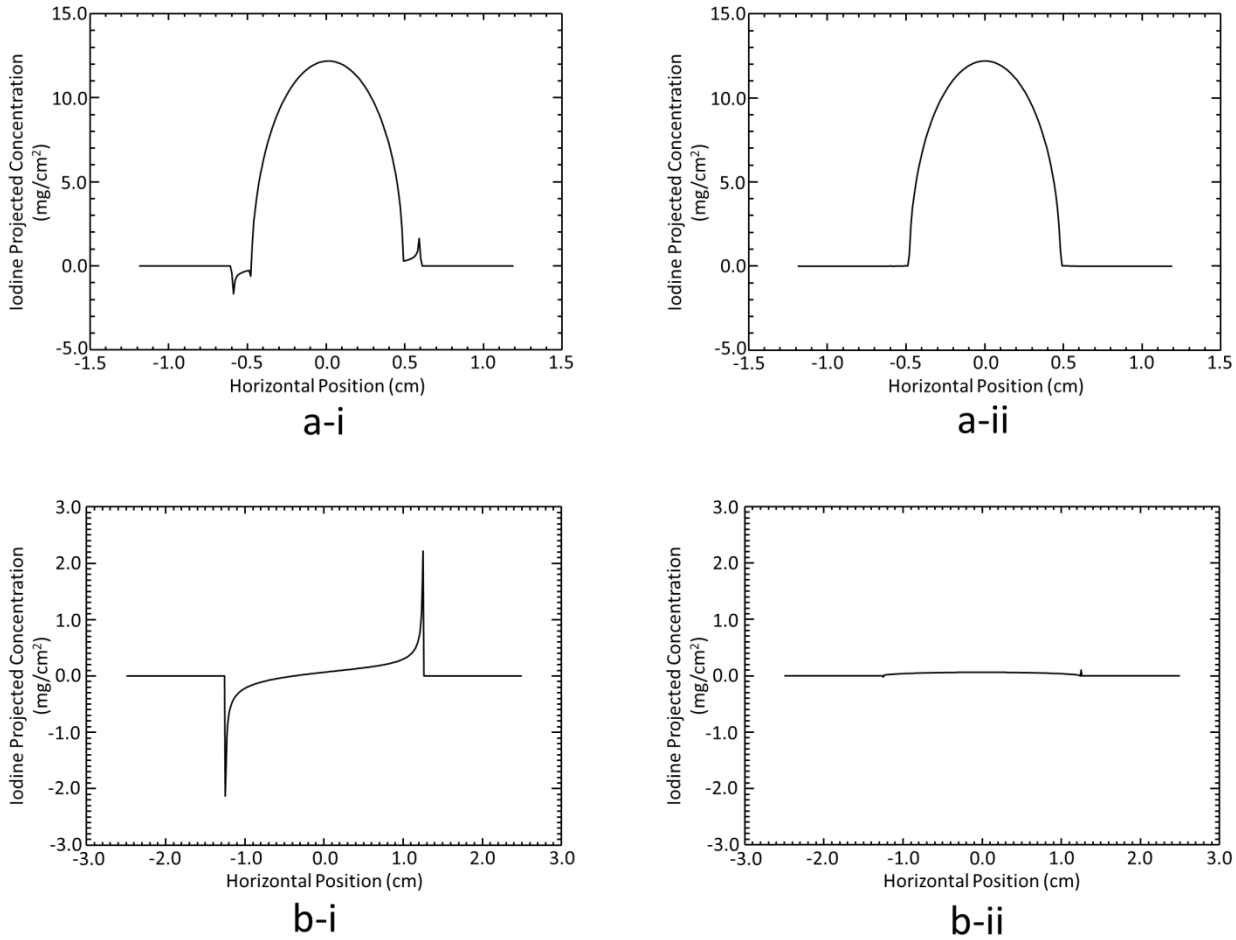

Figure 6.10: Reduction of modeled crossover artifact using program developed. MEI crossover artifact model of a tube (a-i) and a rod (b-i) due to an offset of -5.0 cm; (a-ii, and b-ii) show offset corrected, i.e., crossover artifact reduced.

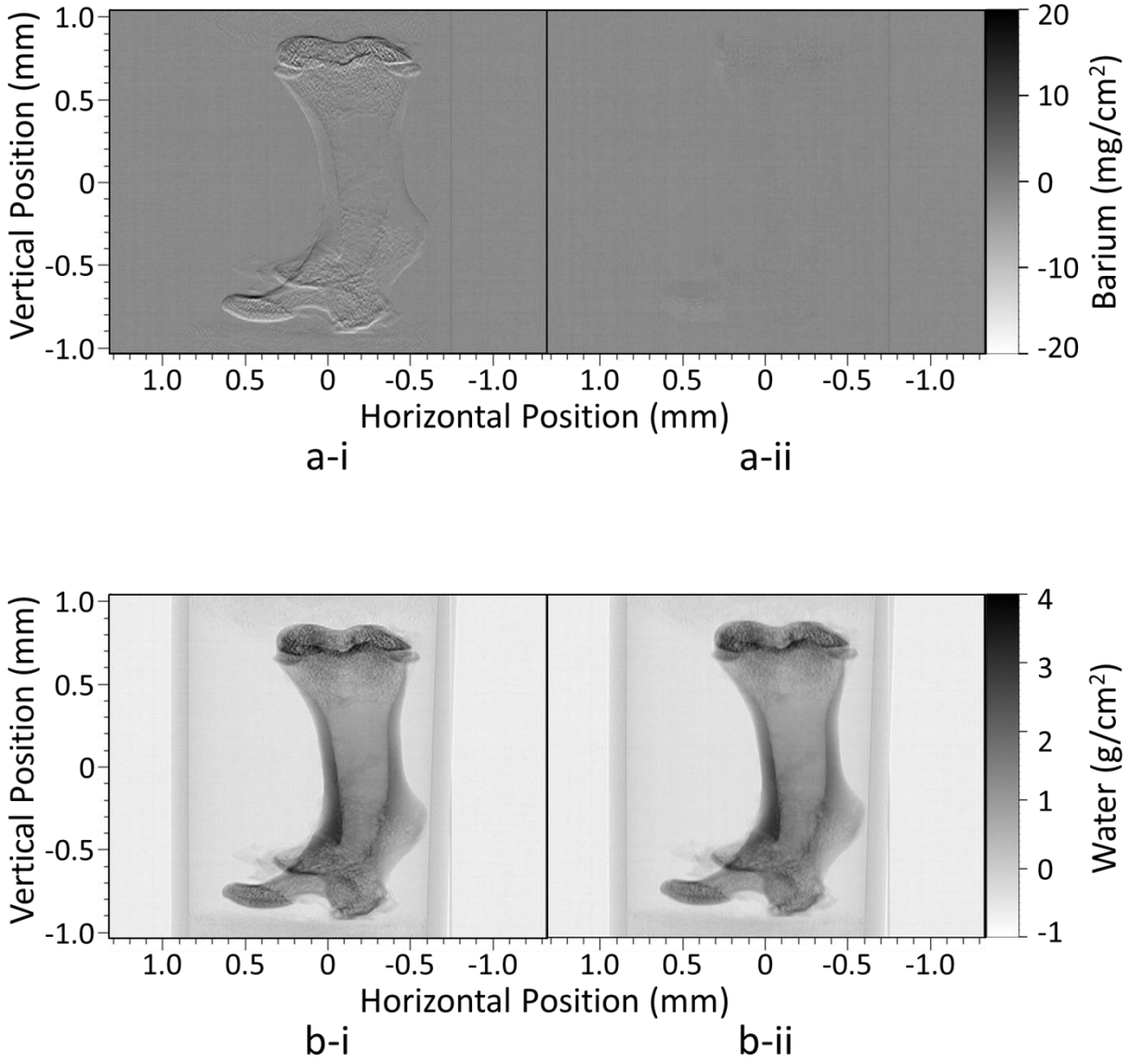

Figure 6.11: Reduction of crossover artifact in spectral-KES images: (a) barium and (b) water. Images on the left show before 'correction' algorithm applied, and on the right after crossover correction. The sample is a femur bone of a 1-month old (i.e. developing skeleton) rat receiving oral dose of 58.5 mg/kg/day $BaCl_2$ (equivalent to 33 mg/kg/day free Ba^{2+}) for 28 consecutive days.

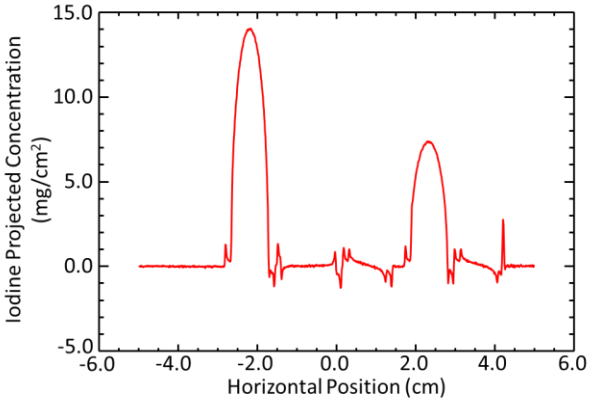

a-i

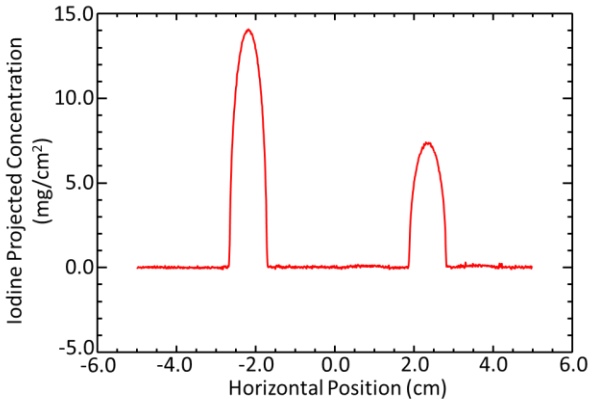

a-ii

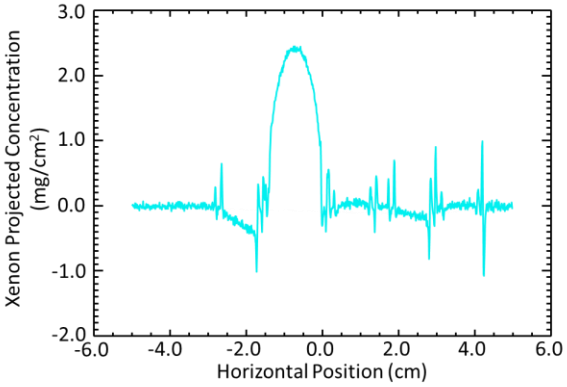

b-i

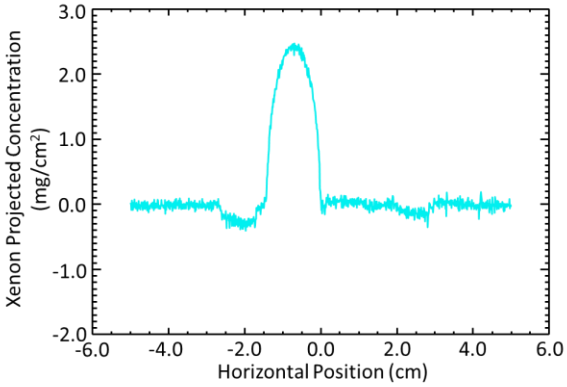

b-ii

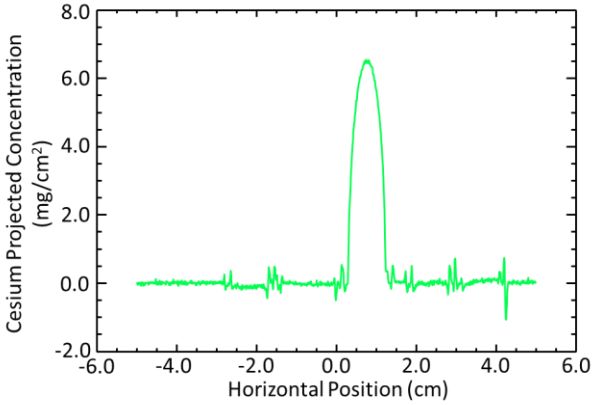

c-i

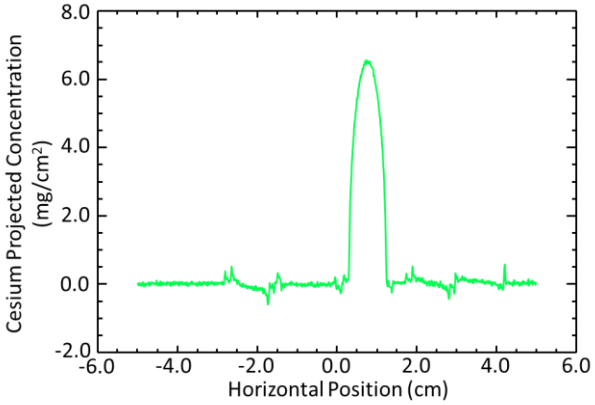

c-ii

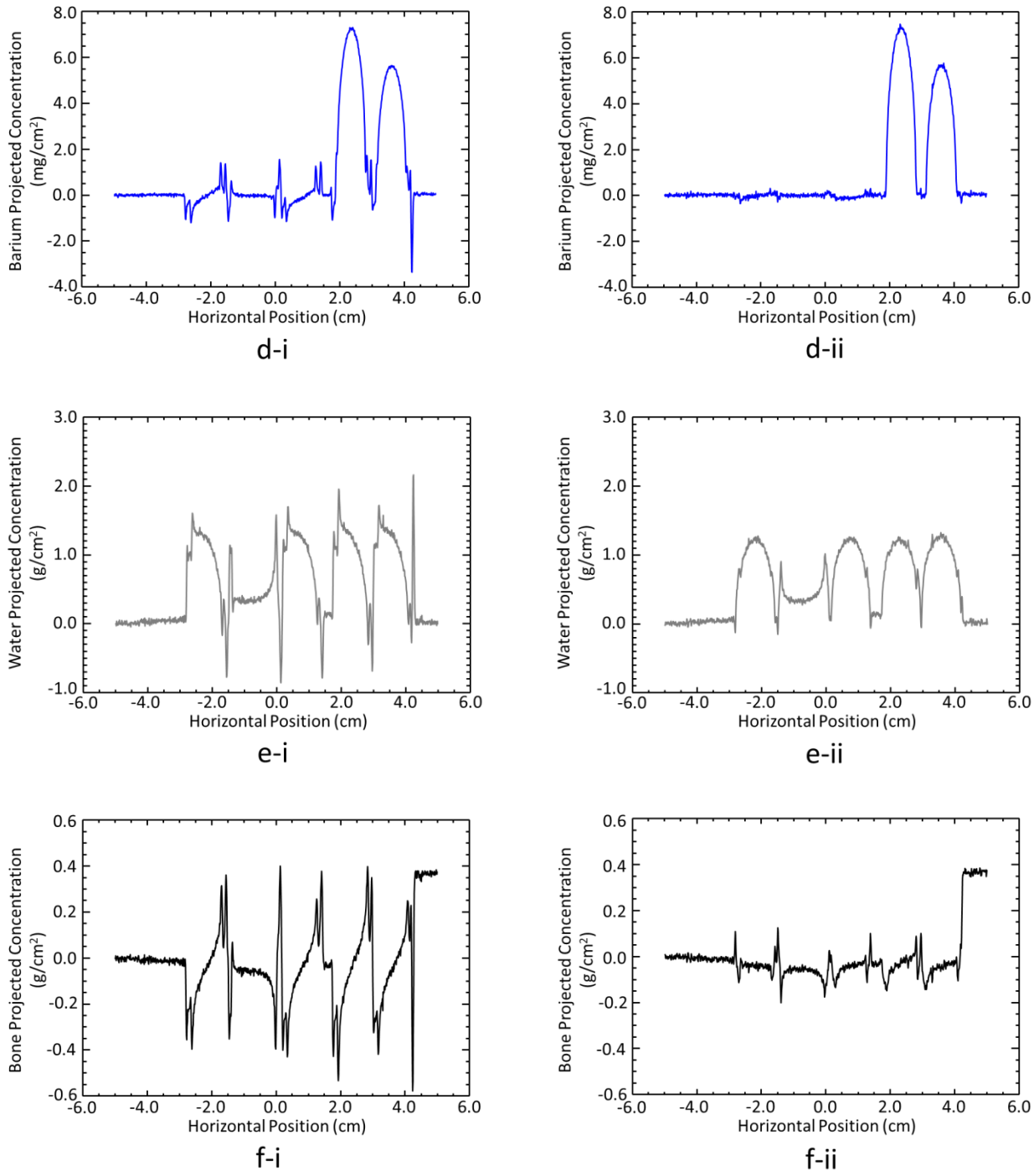

Figure 6.12: Reduction of crossover artifact in experimental MEI projected concentration plots. Offset correction is -0.5 cm. The uncorrected data are on the left (i column) and corrected on the right (ii column) for iodine (a), xenon (b), cesium (c), barium (d), water (e), and bone (f).

From figures 6.10, 6.11 and 6.12, it will be agreed that the crossover reduction algorithm work well for both modeled and experimental data. Images shown in figure 6.11 are that of a rat femur bone that has incorporated a small amount of barium as a marker of new bone growth. There are spectral KES images and are from experimental data courtesy of Dr. David M. L. Cooper laboratory. Spectral KES has a relatively narrow energy range (~0.55 keV with 37.4 keV K-edge energy for Ba) and hence range of angles in the focused beam compared to MEI might be expected to be more easily correctable. The uncorrected image (figure 6.11 a-i) clearly shows the derivative like behavior of a crossover artifact. The corrected image (figure 6.11a-ii) has reduced the visibility of any features to almost the point of invisibility using the same contrast scale. For reference, the water image (figure 6.11b-i and 6.11b-ii) is also shown and corrections have little visible effect on its appearance due to the highly structured nature of the bone and the contrast scale. It should be noted that the reduction in the crossover artifact appears to remove image detail in figures 6.11a-i and 6.11b-i. This occurs because of the reduction in edge enhancement due to the derivative like behaviour of the crossover artifact - the detail in those images is not real.

MEI images in terms of the projected concentration plots are shown in figure 6.12 and are also based on experimental data. Due to the large spectral energy range, and angular range of the focused beam, the images are somewhat more susceptible to the crossover artifact. Examples of the artifact suppression are shown in figure 6.12a- to 6.12f-ii using the same crossover correction algorithm. Though the experimental data were taken near the focus, there are quite large crossover artifacts. The approximate correction is equivalent to about 0.5 cm motion from the location of the subject. In some instances, the artifact suppression is nearly complete.

CHAPTER 7

CONCLUSIONS AND FUTURE RESEARCH

The desires and efforts to make the BMIT facility at the CLS more attractive to researchers in the field of biomedical imaging have resulted in the development of yet another novel imaging system. Details of this novel imaging system, MEI, have been presented in this thesis. Spectral-KES system is the novel imaging system earlier developed at the BMIT facility. The MEI system is developed for biomedical imaging applications at BMIT BM beamline, and is based on a single bent Laue Si (5, 1, 1) crystal monochromator. The imaging beam prepared is horizontally focused because the MEI bent Laue Si monochromator focuses in the horizontal direction, the SR filtered white beam incident on it. And depending on the incident beam size, the focused beam energy bandwidth varies, covering K-edges of iodine, xenon, cesium, and barium, which are all within the diagnostic energy range. Thus, it is possible to use these energies simultaneous for imaging. The large beam width of the BMIT BM beamline is in part what allows the large spectral energy to be covered. With the MEI system, six materials (I, Xe, Cs, Ba, bone, and water) have been successfully decomposed in terms of their project concentrations. The novel aspect of this MEI system is the large energy bandwidth that can be achieved-up to 15 keV with a middle energy around 30 keV. To the best of our knowledge, never before has such a large energy range been achieved with a single bent Laue Si crystal monochromator and up to six materials decomposed from the spectral energy data.

For quantification of iodine, cesium and barium in a subject, the minimum detection limit of the MEI system is about 1.0 mg/ml for iodine and barium, and 0.5 mg/ml for cesium. The detection limit of 1.0 mg/ml for iodine is comparable to 1.3 mg/ml reported for Spectral KES imaging system (Zhu et al., 2014). In joint arthrography, the concentration of iodine used as contrast agent is said to be relatively high-15 to 80 mg/ml upon dilution in the synovial fluid [180]. In the study by Schültke et al. (2010), it is stated that after administering 0.9 ml/kg iodinated contrast agent (Xenetix®) to a pig model via intravenous injection, the peak iodine concentration in the internal carotid and middle cerebral arteries reached 35 mg/ml. Also, in a lung cancer and angiogenesis imaging using synchrotron radiation [209], the concentration of barium contrast agent ($BaSO_4$ suspension) injected to a mouse was 500 mg/ml. These stated

concentrations of iodine and barium contrast agents are very high when compared to the minimum detection limits of iodine and barium for the MEI system. Clearly, the sensitivity of the MEI system may be sufficient for K-edge and multiple K-edge imaging (projection not CT mode) applications in which these elements, including xenon, are used as contrast agents.

Crossover artifacts are a pervasive problem for focal type K-edge subtraction systems where the imaging beams cross near the subject location. A major concern with the MEI system was crossover artifacts in the projected concentrations of materials decomposed from the spectral energy data obtained but this is no more a problem. Based on our understanding of the physical and mathematical origins of crossover artifact, the issue of this artifact has been addressed, not just for the MEI, but also for the dual-beam form of KES and spectral KES imaging. The ability to reduce crossover artifacts in MEI, spectral KES and dual-beam images after acquisition is very important as this will avoid unnecessary dose and additional imaging sessions.

For future research, the large energy range that can be covered raises the possibility of using the MEI system in a vertical diffraction plane. When used in the vertical diffraction plane, the imaging energy can be changed rapidly by a simple vertical motion of the monochromator to different K-edges. This motion would need to be coupled with motions of the subject and detector which may be very challenging, but the simplicity of the system might warrant its use in this way. Also, though the projected concentration values for the materials decomposed are generally non-negative, there is plan to develop a non-negative least squares (NNLS) based algorithm using the IMSL_LINLSQ routine in IDL for materials decomposition.

The large energy range of the MEI system is attributed to the bent Laue Si crystal and incident beam size in the diffraction plane. Based on these, it is also possible to develop an x-ray tube based MEI system using the bremsstrahlung component of the tube's spectrum, for example, that of a tungsten target tube. Some considerations should be given to the shape of the bent crystal, presumably elliptical, to give an acceptable focus. There has been preliminary work in this area [210], which was limited in energy range.

For the MEI system, a cylindrical bent crystal was used because of convenience. Given the geometry where the source to crystal (f_1) distance is much larger than the crystal to focus distance (f_2), a parabolic geometry is best used. Some of the sizes of the beam at the focus are almost certainly due to the cylindrical versus parabolic bend. In optics, this would have been referred to as spherical aberration; however, in our case of focusing in one dimension, it would

be more properly called cylindrical aberration. Preliminary experience with a parabolic geometry for x-ray reflectometry is being prepared for publication (Cahit Karanfil et al. to be published).

REFERENCES

[1] A. Webb, Introduction to Biomedical Imaging, John Wiley & Sons, Inc., New Jersey, USA, 2003.

[2] A. Oppelt, Imaging Systems for Medical Diagnostics, Publicis Corporate Publishing, Erlangen, Germany, 2005.

[3] J.T. Bushberg, J.A. Seibert, J. Edwin M. Leidholdt, J.M. Boone, The Essential Physics of Medical Imaging, Second ed., Lippincott Williams & Wilkins, Philadelphia, USA, 2002.

[4] N.G. Anderson, A.P. Butler, N.J.A. Scott, N.J. Cook, J.S. Butzer, N. Schleich, M. Firsching, R. Grasset, N. de Ruiter, M. Campbell, P. H. Butler, Spectroscopic (multi-energy) CT distinguishes iodine and barium contrast material in MICE, European Radiology, 20 (2010) 2126-2134.

[5] J. Fornaro, S. Leschka, D. Hibbeln, A. Butler, N. Anderson, G. Pache, H. Scheffel, S. Wildermuth, H. Alkadhi, P. Stolzmann, Dual- and multi-energy CT: approach to functional imaging, Insights Imaging, 2 (2011) 149-159.

[6] S.J. Nik, J. Meyer, R. Watts, Optimal material discrimination using spectral x-ray imaging, Physics in Medicine and Biology, 56 (2011) 5969-5983.

[7] H. Ghadiri, M.R. Ay, M.B. Shiran, H. Soltanian-Zadeh, H. Zaidi, K-edge ratio method for identification of multiple nanoparticulate contrast agents by spectral CT imaging, British Journal of Radiology, 86 (2013) 1-20.

[8] F.L. Roder, Principles, history, and status of dual-energy computerized tomographic explosives detection, Journal of Testing and Evaluation, 13 (1985) 211-216.

[9] J. Lee, Y. Lee, S. Cho, B.-C. Lee, A dual-energy material decomposition method for high-energy X-ray cargo inspection, Journal of the Korean Physical Society, 61 (2012) 821-824.

[10] S.J. Nik, R.S. Thing, R. Watts, T. Dale, B. Currie, J. Meyer, Monte Carlo validation of optimal material discrimination using spectral x-ray imaging, Journal of Instrumentation, 9 (2014) 1-16.

[11] K. Dong-Goo, S. Younghun, K. SungSu, L. SeongDeok, J.D. Kim, Multiple object decomposition based on independent component analysis of multi-energy x-ray projections, Image Processing (ICIP), 16th IEEE International Conference on, Cairo, Egypt, 2009, 4173-4176.

[12] K. Ham, L.G. Butler, Algorithms for three-dimensional chemical analysis via multi-energy synchrotron X-ray tomography, Nuclear Instruments and Methods in Physics Research B 262 (2007) 117-127.

[13] H.B. Donald, E. Pascal, W. Edgar, Review of third and next generation synchrotron light sources, Journal of Physics B: Atomic, Molecular and Optical Physics, 38 (2005) S773-S797.

[14] T.W. Wysokinski, D. Chapman, G. Adams, M. Renier, P. Suortti, W. Thomlinson, Beamlines of the biomedical imaging and therapy facility at the Canadian Light Source-Part 1, Nuclear Instruments and Methods in Physics Research A 582 (2007) 73-76.

[15] T.W. Wysokinski, D. Chapman, G. Adams, M. Renier, P. Suortti, W. Thomlinson, Beamlines of the biomedical imaging and therapy facility at the Canadian Light Source - Part 2, Journal of Physics: Conference Series, 425 (2013) 1-4.

[16] T.W. Wysokinski, D. Chapman, G. Adams, M. Renier, P. Suortti, W. Thomlinson, Beamlines of the biomedical imaging and therapy facility at the Canadian Light Source-Part 3, Nuclear Instruments and Methods in Physics Research A 775 (2015) 1-4.

[17] E. Schültke, S. Fiedler, C. Nemoz, L. Ogieglo, M.E. Kelly, P. Crawford, F. Esteve, T. Brochard, M. Renier, H. Requardt, G. Le Duc, B. Juurlink, K. Meguro, Synchrotron-based intra-venous K-edge digital subtraction angiography in a pig model: A feasibility study, European Journal of Radiology, 73 (2010) 677-681.

[18] S.A. McDonald, F. Marone, C. Hintermuller, G. Mikuljan, C. David, F. Pfeiffer, M. Stampanoni, Advanced phase-contrast imaging using a grating interferometer, Journal of Synchrotron Radiation, 16 (2009) 562-572.

[19] J.Z. Hu, T.D. Wu, L. Zeng, H.Q. Liu, Y. He, G.H. Du, H.B. Lu, Visualization of microvasculature by x-ray in-line phase contrast imaging in rat spinal cord, Physics in Medicine and Biology, 57 (2012) N55-63.

[20] F. Arfelli, D. Pelliccia, A. Cedola, A. Astolfo, I. Bukreeva, P. Cardarelli, D. Dreossi, S. Lagomarsino, R. Longo, L. Rigon, N. Sodini, R.H. Menk, Recent developments on techniques for differential phase imaging at the medical beamline of ELETTRA, Journal of Instrumentation, 8 (2013) 1-14.

[21] C. Hall, Large-scale imaging on the Australian synchrotron imaging and medical beamline, Synchrotron Radiation News, 28 (2015) 24-29.

[22] K. Uesugi, H. Yasuda, B. Pierscionek, K. Toyoda, M. Hoshino, N. Yagi, Large-field x-ray imaging at SPring-8 BL20B2, Synchrotron Radiation News, 28 (2015) 30-35.

[23] M. Ando, N. Sunaguchi, Y. Wu, S. Do, Y. Sung, A. Louissaint, T. Yuasa, S. Ichihara, R. Gupta, Crystal analyser-based X-ray phase contrast imaging in the dark field: implementation and evaluation using excised tissue specimens, European Radiology, 24 (2014) 423-433.

[24] D. Chapman, N. Samadi, M. Martnson, B. Bassey, S. Boire, G. Belev, T. Wysokinski, X-ray optics development for biomedical imaging applications at the Canadian Light Source, Physics in Canada, 70 (2014) 19-23.

[25] J. Als-Nielsen, D. McMorrow, Elements of Modern X-ray Physics, Second ed., John Wiley & Sons, Ltd, London, United Kingdom, 2011.

[26] I. Thomas S. Curry, J.E. Dowdey, J. Robert C. Murry, Christensen's Physics of Diagnostic Radiology, Fourth ed., Lippincott Williams & Wilkins, Philadelphia, USA, 1990.

[27] S. Ebashi, M. Koch, E. Rubenstein, Handbook on Synchrotron Radiation, in: E.-E. Koch, T. Sasaki, H. Winick (Eds.), Elsevier Science Publishers B. V., Amsterdam, Netherlands, 1991.

[28] R. Lewis, Medical applications of synchrotron radiation x-rays, Physics in Medicine and Biology, 42 (1997) 1213-1243.

[29] W.R. Hendee, E.R. Ritenour, Medical Imaging Physics, Fourth ed., John Wiley & Sons, Inc., New York, USA, 2002.

[30] E.B. Podgorsak, Radiation Physics for Medical Physicists, Spinger-Verlag Berlin Heidelberg, Berlin, Germany, 2006.

[31] M.A. Omar, Elementary Solid State Physics: Principles and Applications, Addison-Wesley Publishing Company, Inc. Carlifornia, USA, 1975.

[32] B.A. Schueler, Clinical applications of basic x-ray physics principles, RadioGraphics, 18 (1998) 731-744.

[33] P. Suortti, W. Thomlinson, Medical applications of synchrotron radiation, Physics in Medicine and Biology, 48 (2003) R1-R35.

[34] A. Erko, F. Schäfers, W. Gudat, N.V. Abrosimov, S.N. Rossolenko, V. Alex, S. Groth, W. Schröder, On the feasibility of employing gradient crystals for high resolution synchrotron optics, Nuclear Instruments and Methods in Physics Research A 374 (1996) 408-412.

[35] C. Schulze, U. Lienert, M. Hanfland, M. Lorenzen, F. Zontone, Microfocusing of hard x-rays with cylindrically bent crystal monochromators, Journal of Synchrotron Radiation, 5 (1998) 77-81.

[36] B.E. Warren, X-Ray Diffraction, Dover Publications, Inc., New York, USA, 1990.

[37] M. Hart, L. Berman, X-ray Optics for Synchrotron Radiation; Perfect crystals, mirrors and multilayers, Acta Crystallographica Section A, 54 (1998) 850-858.

[38] N.W. Ashcroft, N.D. Mermin, Solid State Physics, Thomson Learning, Inc. New York, USA, 1976.

[39] W.H. Zachariasen, Theory of X-Ray Diffraction in Crystals, Dover Publications Inc., Mineola, New York, 1967.

[40] P. Suortti, C. Schulze, Fixed-exit monochromators for high-energy synchrotron radiation, Journal of Synchrotron Radiation, 2 (1995) 6-12.

[41] S.D. Shastri, K. Fezzaa, A. Mashayekhi, W.-K. Lee, P.B. Fernandez, P.L. Lee, Cryogenically cooled bent double-Laue monochromator for high-energy undulator x-rays (50-200 keV), Journal of Synchrotron Radiation, 9 (2002) 317-322.

[42] P. Suortti, Pattison, P. & W. Weyrich, An x-ray spectrometer for inelastic scattering experiments. I. Curved-crystal X-ray optics, Journal of Applied Crystallography, 19 (1986) 336-342.

[43] P. Suortti, U. Lienert, C. Schulze, Bent crystal optics for high energy synchrotron radiation, American Institute of Physics Conference Proceedings, 389 (1997) 175-192.

[44] B. Ren, F.A. Dilmanian, L.D. Chapman, X.Y. Wu, Z. Zhong, I. Ivanov, W.C. Thomlinson, X. Huang, Beam-smiling in bent-Laue monochromators, American Institute of Physics Conference Proceedings, 417 (1997) 106-116.

[45] A.R. Lennie, D. Laundy, M.A. Roberts, G. Bushnell-Wye, A novel facility using a Laue focusing monochromator for high-pressure diffraction at the SRS, Daresbury, UK, Journal of Synchrotron Radiation, 14 (2007) 433-438.

[46] C. Karanfil, D. Chapman, C.U. Segre, G. Bunker, A device for selecting and rejecting x-ray harmonics in synchrotron radiation beams, Journal of Synchrotron Radiation, 11 (2004) 393-398.

[47] V. Mocella, J.P. Guigay, J. Hrdy, C. Ferrero, J. Hoszowska, Bent crystals in Laue geometry: dynamical focusing of a polychromatic incident beam, Journal of Applied Crystallography, 37 (2004) 941-946.

[48] B. Ren, F.A. Dilmanian, L.D. Chapman, I. Ivanov, X.Y. Wu, Z. Zhong, X. Huang, A bent Laue–Laue monochromator for a synchrotron-based computed tomography system, Nuclear Instruments and Methods in Physics Research A 428 (1999) 528-550.

[49] J.Y.P. Ko, B.O. Benjamin, J.S. James, K.P. Alan, L. Aaron, R. Peter, P.M. Matthew, D.B. Joel, Designing and commissioning of a prototype double Laue monochromator at CHESS, Journal of Physics: Conference Series, 493 (2014) 1-5.

[50] Z.H. Kalman, S. Weissmann, On the X-ray reflectivity of elastically bent perfect crystals, Journal of Applied Crystallography, 16 (1983) 295-303.

[51] C. Schulze, P. Suortti, D. Chapman, Test of a bent Laue double crystal fixed exit monochromator, Synchrotron Radiation News, 7 (1994) 8-11.

[52] S. Bellucci, S. Bini, V.M. Biryukov, Y.A. Chesnokov, S. Dabagov, G. Giannini, V. Guidi, Y.M. Ivanov, V.I. Kotov, V.A. Maisheev, C. Malagù, G. Martinelli, A.A. Petrunin, V.V. Skorobogatov, M. Stefancich, D. Vincenzi, Experimental study for the feasibility of a crystalline undulator, Physical Review Letters, 90 (2003) 1-3.

[53] N. Barriere, V. Guidi, V. Bellucci, R. Camattari, T. Buslaps, J. Rousselle, G. Roudil, F.-X. Arnaud, P. Bastie, L. Natalucci, High diffraction efficiency at hard x-ray energy in a silicon crystal bent by indentation, Journal of Applied Crystallography, 43 (2010) 1519-1521.

[54] V. Bellucci, R. Camattari, V. Guidi, I. Neri, N. Barrière, Self-standing bent silicon crystals for very high efficiency Laue lens, Experimental Astronomy, 31 (2011) 45-58.

[55] R. Smither, K. Saleem, D. Roa, M. Beno, P. Ballmoos, G. Skinner, High diffraction efficiency, broadband, diffraction crystals for use in crystal diffraction lenses, Experimental Astronomy, 20 (2005) 201-210.

[56] R. Smither, K.A. Saleem, M. Beno, C. Kurtz, A. Khounsary, N. Abrosimov, Diffraction efficiency and diffraction bandwidth of thermal-gradient and composition-gradient crystals, Review of Scientific Instruments, 76 (2005) 1-19.

[57] N.V. Abrosimov, S.N. Rossolenko, V. Alex, A. Gerhardt, W. Schröder, Single crystal growth of Si1 − xGex by the Czochralski technique, Journal of Crystal Growth, 166 (1996) 657-662.

[58] R. Camattari, E. Dolcini, V. Bellucci, A. Mazzolari, V. Guidi, High diffraction efficiency with hard x-rays through a thick silicon crystal bent by carbon fiber deposition, Journal of Applied Crystallography, 47 (2014) 1762-1764.

[59] R. Camattari, G. Paterno, A. Battelli, V. Bellucci, P. Bastie, V. Guidi, High-efficiency focusing of hard x-rays exploiting the quasi-mosaic effect in a bent germanium crystal, Journal of Applied Crystallography, 47 (2014) 799-802.

[60] V. Bellucci, G. Paterno, R. Camattari, V. Guidi, M. Jentschel, P. Bastie, High-efficiency diffraction and focusing of x-rays through asymmetric bent crystalline planes, Journal of Applied Crystallography, 48 (2015) 297-300.

[61] V. Guidi, V. Bellucci, R. Camattari, I. Neri, Proposal for a Laue lens with quasi-mosaic crystalline tiles, Journal of Applied Crystallography, 44 (2011) 1255-1258.

[62] R. Camattari, V. Guidi, V. Bellucci, A. Mazzolari, The `quasi-mosaic' effect in crystals and its applications in modern physics, Journal of Applied Crystallography, 48 (2015) 977-989.

[63] Y. Wu, S. Xiao, J. Lu, L. Liu, Q. Yang, X. Huang, Research on a logarithmically bent Laue crystal analyzer for x-ray monochromatic backlight imaging, Review of Scientific Instruments, 84 (2013) 1-5.

[64] C. Karanfil, G. Bunker, M. Newville, C.U. Segre, D. Chapman, Quantitative performance measurements of bent crystal Laue analyzers for x-ray fluorescence spectroscopy, Journal of Synchrotron Radiation, 19 (2012) 375-380.

[65] Z. Zhong, L.D. Chapman, B.A. Bunker, G.B. Bunker, R. Fischetti, C.U. Segre, A bent Laue analyzer for fluorescence EXAFS detection, Journal of Synchrotron Radiation, 6 (1999) 212-214.

[66] Z. Zhong, C.C. Kao, D.P. Siddons, J.B. Hastings, Rocking-curve width of sagittally bent Laue crystals, Acta crystallographica, 58 (2002) 487-493.

[67] Z. Zhong, C.C. Kao, D.P. Siddons, J.B. Hastings, Sagittal focusing of high-energy synchrotron X-rays with asymmetric Laue crystals. I. Theoretical considerations, Journal of Applied Crystallography, 34 (2001) 504-509.

[68] Z. Zhong, C.C. Kao, D.P. Siddons, J.B. Hastings, Sagittal focusing of high-energy synchrotron x-rays with asymmetric Laue crystals. II. Experimental studies, Journal of Applied Crystallography, 34 (2001) 646-653.

[69] S. Keitel, C. Malgrange, T. Niemoller, J.R. Schneider, Diffraction of 100 to 200 keV x-rays from an Si1-xGex gradient crystal: comparison with results from dynamical theory, Acta Crystallographica, 55 (1999) 855-863.

[70] C. Malgrange, X-ray propagation in distorted crystals: from dynamical to kinematical theory, Crystal Research and Technology, 37 (2002) 654-662.

[71] P. Suortti, T. Buslaps, P. Fajardo, V. Honkimaki, M. Kretzschmer, U. Lienert, J.E. McCarthy, M. Renier, A. Shukla, T. Tschentscher, T. Meinander, Scanning x-ray spectrometer for high-resolution Compton profile measurements at ESRF, Journal of Synchrotron Radiation, 6 (1999) 69-80.

[72] T. Tschentscher, P. Suortti, Experiments with very high energy synchrotron radiation, Journal of Synchrotron Radiation, 5 (1998) 286-292.

[73] G. Paterno, V. Bellucci, R. Camattari, V. Guidi, Design study of a Laue lens for nuclear medicine, Journal of Applied Crystallography, 48 (2015) 125-137.

[74] B.W. Batterman, H. Cole, Dynamical diffraction of x-rays by perfect crystals, Reviews of Modern Physics, 36 (1964) 681-717.

[75] P. Suortti, Focusing monochromators for high energy synchrotron radiation, Review of Scientific Instruments, 63 (1992) 942-945.

[76] M. Sanchez del Rio, N. Perez-Bocanegra, X. Shi, V. Honkimaki, L. Zhang, Simulation of x-ray diffraction profiles for bent anisotropic crystals, Journal of Applied Crystallography, 48 (2015) 477-491.

[77] M. Sanchez del Rio, C. Ferrero, V. Mocella, Computer simulation of bent perfect crystal diffraction profiles, Proceedings of SPIE, 3151 (1997) 312-323.

[78] Z. Zhong, C.C. Kao, D.P. Siddons, H. Zhong, J.B. Hastings, A lamellar model for the x-ray rocking curves of sagittally bent Laue crystals, Acta crystallographica. Section A, Foundations of crystallography, 59 (2003) 1-6.

[79] E. Erola, V. Etelaniemi, P. Suortti, P. Pattison, W. Thomlinson, X-ray reflectivity of bent perfect crystals in Bragg and Laue geometry, Journal of Applied Crystallography, 23 (1990) 35-42.

[80] C. Schulze, D. Chapman, pepo: A program for the calculation of the reflectivity of cylindrically bent Laue crystal monochromators, Review of Scientific Instruments, 66 (1995) 2220-2223.

[81] P. Suortti, S. Fiedler, A. Bravin, T. Brochard, M. Mattenet, M. Renier, P. Spanne, W. Thomlinson, A.M. Charvet, H. Elleaume, C. Schulze-Briese, A.C. Thompson, Fixed-exit monochromator for computed tomography with synchrotron radiation at energies 18-90 keV, Journal of Synchrotron Radiation, 7 (2000) 340-347.

[82] Y.I. Nesterets, S.W. Wilkins, A flexible configuration for a high-energy phase-contrast imaging beamline involving in-line focusing crystal optics, Radiation Physics and Chemistry, 75 (2006) 1981-1985.

[83] Y.I. Nesterets, S.W. Wilkins, Evaluation of the focusing performance of bent Laue crystals using wave-optical theory, Journal of Applied Crystallography, 41 (2008) 237-248.

[84] G. Illing, J. Heuer, B. Reime, M. Lohmann, R.H. Menk, L. Schildwächter, W.R. Dix, W. Graeff, Double beam bent Laue monochromator for coronary angiography, Review of Scientific Instruments, 66 (1995) 1379-1381.

[85] P. Suortti, W. Thomlinson, D. Chapman, N. Gmur, D. P. Siddons, and C. Schulze, A single crystal bent Laue monochromator for coronary angiography, Nuclear Instruments and Methods in Physics Research A 336 (1993) 304-309.

[86] P. Suortti, W. Thomlinson, A bent Laue crystal monochromator for angiography at the NSLS, Nuclear Instruments and Methods A 269 (1988) 639-648.

[87] M. Martinson, N. Samadi, B. Bassey, A. Gomez, D. Chapman, Phase-preserving beam expander for biomedical X-ray imaging, Journal of Synchrotron Radiation, 22 (2015) 801-806.

[88] J.P. Sutter, T. Connolley, M. Drakopoulos, T.P. Hill, D.W. Sharp, Ray traces of an arbitrarily deformed double-crystal Laue x-ray monochromator, Proceedings of SPIE, Advances in X-Ray/EUV Optics and Components III, 7077 (2008) 1-12.

[89] B. Jacobson, Dichromatic absorption radiography; dichromography, Acta Radiologica, 39 (1953) 437-452.

[90] Y. Zhu, N. Samadi, M. Martinson, B. Bassey, Z. Wei, G. Belev, D. Chapman, Spectral K-edge subtraction imaging, Physics in Medicine and Biology, 59 (2014) 2485-2503.

[91] P. Suortti, W. Thomlinson, D. Chapman, N. Gmür, R. Greene, N. Lazarz, Performance evaluation of a bent Laue monochromator, Nuclear Instruments and Methods in Physics Research A 297 (1990) 268-274.

[92] H. Elleaume, S. Fiedler, F. Estève, B. Bertrand, A.M. Charvet, P. Berkvens, G. Berruyer, T. Brochard, G.L. Duc, C. Nemoz, M. Renier, P. Suortti, W. Thomlinson, J.F.L. Bas, First human transvenous coronary angiography at the European synchrotron radiation facility, Physics in Medicine and Biology, 45 (2000) L39-L43.

[93] W.R. Dix, H.J. Besch, W. Graeff, C.W. Hamm, G. Illing, W. Kupper, M. Lohmann, T. Meinertz, R.H. Menk, B. Reime, C. Rust, L. Schildwächter, A.H. Walenta, Intravenous coronary angiography with synchrotron radiation, Physica Scripta, 1996 (1996) 51-56.

[94] A. Peterzol, A. Bravin, P. Coan, H. Elleaume, Performance of the K-edge digital subtraction angiography imaging system at the European synchrotron radiation facility, Radiation Protection Dosimetry, 117 (2005) 44-49.

[95] P. Baldelli, A. Bravin, C.D. Maggio, G. Gennaro, A. Sarnelli, A. Taibi, M. Gambaccini, Evaluation of the minimum iodine concentration for contrast-enhanced subtraction mammography, Physics in Medicine and Biology, 51 (2006) 4233-4251.

[96] J.C. Giacomini, H. Gordon, R. O'Neil, A. Van Kessel, B. Cason, D. Chapman, W. Lavendar, N. Gmur, R. Menk, W. Thomlinson, Z. Zhong, E. Rubenstein, Bronchial imaging in humans using xenon K-edge dichromography, Nuclear Instruments and Methods in Physics Research A 406 (1998) 473-478.

[97] H. Suhonen, L. Porra, S. Bayat, A.R.A. Sovijärvi, P. Suortti, Simultaneous in vivo synchrotron radiation computed tomography of regional ventilation and blood volume in rabbit lung using combined K-edge and temporal subtraction, Physics in Medicine and Biology, 53 (2008) 775-791.

[98] A. Panahifar, N. Samadi, T.M. Swanston, L.D. Chapman, D.M. Cooper, Spectral K-edge subtraction imaging of experimental non-radioactive barium uptake in bone, Physica Medica, 32 (2016) 1765-1770.

[99] A.C. Thompson, J. Llacer, L. Campbell Finman, E.B. Hughes, J.N. Otis, S. Wilson, H.D. Zeman, Computed tomography using synchrotron radiation, Nuclear Instruments and Methods in Physics Research, 222 (1984) 319-323.

[100] N. Hiraoka, H. Fukui, H. Tanida, H. Toyokawa, Y.Q. Cai, K.D. Tsuei, An X-ray Raman spectrometer for EXAFS studies on minerals: bent Laue spectrometer with 20 keV x-rays, Journal of Synchrotron Radiation, 20 (2013) 266-271.

[101] A.J. Kropf, J.A. Fortner, R.J. Finch, J.C. Cunnane, C. Karanfil, A bent silicon crystal in the Laue geometry to resolve actinide x-ray fluorescence for x-ray absorption spectroscopy, Physica Scripta, T115 (2005) 998-1000.

[102] R.L. Bilsborrow, P.A. Atkinson, N. Bliss, A.J. Dent, B.R. Dobson, P.C. Stephenson, A wide-aperture dynamically focusing sagittal monochromator for X-ray spectroscopy and diffraction, Journal of Synchrotron Radiation, 13 (2006) 54-58.

[103] A.J. Kropf, R.J. Finch, J.A. Fortner, S. Aase, C. Karanfil, C.U. Segre, J. Terry, G. Bunker, L.D. Chapman, Bent silicon crystal in the Laue geometry to resolve x-ray fluorescence for x-ray absorption spectroscopy, Review of Scientific Instruments, 74 (2003) 4696-4702.

[104] C. Karanfil, Z. Zhong, L.D. Chapman, R. Fischetti, G.B. Bunker, C.U. Segre, B.A. Bunker, A bent Laue analyzer detection system for dilute fluorescence XAFS, American Institute of Physics Conference Proceedings, 521 (2000) 178-182.

[105] C. Karanfil, L.D. Chapman, G.B. Bunker, C.U. Segre, N.E. Leyarovska, A 'beam cleaner' for harmonic selection/rejection, American Institute of Physics Conference Proceedings, 521 (2000) 276-282.

[106] C. Schulze, U. Kleuker, A bent Laue analyser crystal for Rayleigh-to-Compton computed tomography, Journal of Synchrotron Radiation, 5 (1998) 1085-1087.

[107] N. Hiraoka, M. Itou, T. Ohata, M. Mizumaki, Y. Sakurai, N. Sakai, A new X-ray spectrometer for high-resolution Compton profile measurements at SPring-8, Journal of Synchrotron Radiation, 8 (2001) 26-32.

[108] P. Suortti, T. Buslaps, M. DiMichiel, V. Honkimäki, U. Lienert, J.E. McCarthy, J.M. Merino, A. Shukla, Dispersion-compensating scanning X-ray spectrometer for Compton profile measurements, Nuclear Instruments and Methods in Physics Research A 467–468, (2001) 1541-1544.

[109] M. Martinson, N. Samadi, G. Belev, B. Bassey, R. Lewis, G. Aulakh, D. Chapman, Development of a bent Laue beam-expanding double-crystal monochromator for biomedical X-ray imaging, Journal of Synchrotron Radiation, 21 (2014) 479-483.

[110] M. Firsching, F. Nachtrab, N. Uhlmann, R. Hanke, Multi-energy x-ray imaging as a quantitative method for materials characterization, Advanced Materials, 23 (2011) 2655-2656.

[111] J.C. Miller, Multi-Energy Computed Tomography - New opportunities in imaging the abdomen, Radiology Rounds, A Newsletter for Referring Physicians, Department of Radiology, Massachusetts General Hospital, 2010, 1-5.

[112] A. Bonnin, P. Duvauchelle, V. Kaftandjian, P. Ponard, Concept of effective atomic number and effective mass density in dual-energy x-ray computed tomography, Nuclear Instruments and Methods in Physics Research B 318 (2014) 223-231.

[113] C.H. McCollough, S. Leng, L. Yu, J.G. Fletcher, Dual- and Multi-Energy CT: Principles, Technical Approaches, and Clinical Applications, Radiology, 276 (2015) 637-653.

[114] A.C. Langheinrich, A. Michniewicz, D.G. Sedding, B. Lai, S.M. Jorgensen, R.M. Bohle, E.L. Ritman, Quantitative x-ray imaging of intraplaque hemorrhage in aortas of $apoE^{-/-}$ /$LDL^{-/-}$ double knockout mice, Investigative Radiology, 42 (2007) 263-273.

[115] L. Caschera, A. Lazzara, L. Piergallini, D. Ricci, B. Tuscano, A. Vanzulli, Contrast agents in diagnostic imaging: present and future, Pharmacological Research, 110 (2016) 65-75.

[116] C.O. Schirra, B. Brendel, M.A. Anastasio, E. Roessl, Spectral CT: a technology primer for contrast agent development, Contrast Media & Molecular Imaging, 9 (2014) 62-70.

[117] S.V. Naydenov, V.D. Ryzhikov, C.F. Smith, Direct reconstruction of the effective atomic number of materials by the method of multi-energy radiography, Nuclear Instruments and Methods in Physics Research B 215 (2004) 552-560.

[118] J.P. Ronaldson, R. Zainon, N.J.A. Scott, S.P. Gieseg, A.P. Butler, P.H. Butler, N.G. Anderson, Toward quantifying the composition of soft tissues by spectral CT with Medipix3, Medical Physics, 39 (2012) 6847-6857.

[119] R.E. Alvarez, J.A. Seibert, S.K. Thompson, Comparison of dual energy detector system performance, Medical Physics, 31 (2004) 556-565.

[120] T. Xu, J.L. Ducote, J.T. Wong, S. Molloi, Feasibility of real time dual-energy imaging based on a flat panel detector for coronary artery calcium quantification, Medical Physics, 33 (2006) 1612-1622.

[121] X.Y. Wu, F.A. Dilmanian, Z. Chen, B. Ren, D.N. Slatkin, D. Chapman, M. Shleifer, F.A. Staicu, W. Thomlinson, Multiple energy computed tomography (MECT) at the NSLS: Status report, Review of Scientific Instruments, 66 (1995) 1346-1347.

[122] J.P. Schlomka, E. Roessl, R. Dorscheid, S. Dill, G. Martens, T. Istel, C. Bäumer, C. Herrmann, R. Steadman, G. Zeitler, A. Livne, R. Proksa, Experimental feasibility of multi-energy photon-counting K-edge imaging in pre-clinical computed tomography, Physics in Medicine and Biology, 53 (2008) 4031-4047.

[123] P.V. Granton, S.I. Pollmann, N.L. Ford, M. Drangova, D.W. Holdsworth, Implementation of dual- and triple-energy cone-beam micro-CT for postreconstruction material decomposition, Medical Physics, 35 (2008) 5030-5042.

[124] A.P.H. Butler, N.G. Anderson, R. Tipples, N. Cook, R. Watts, J. Meyer, A.J. Bell, T.R. Melzer, P.H. Butler, Bio-medical X-ray imaging with spectroscopic pixel detectors, Nuclear Instruments and Methods in Physics Research A 591 (2008) 141-146.

[125] C. Jiyang, C. Wenxiang, L. Liang, W. Ge, Combination of current-integrating/photon-counting detector modules for spectral CT, Physics in Medicine and Biology, 58 (2013) 7009-7024.

[126] R.E. Alvarez, A. Macovski, Energy-selective reconstructions in X-ray computerised tomography, Physics in Medicine and Biology, 21 (1976) 733-744.

[127] T. Krasnicki, P. Podgorski, M. Guzinski, A. Czarnecka, K. Tupikowski, J. Garcarek, M. Marek Sasiadek, Novel clinical applications of dual energy computed tomography, Advances in Clinical and Experimental Medicine, 21 (2012) 831-841.

[128] M. Yagi, T. Ueguchi, M. Koizumi, T. Ogata, S. Yamada, Y. Takahashi, I. Sumida, Y. Akino, K. Konishi, F. Isohashi, N. Tomiyama, Y. Yoshioka, K. Ogawa, Gemstone spectral imaging: determination of CT to ED conversion curves for radiotherapy treatment planning, Journal of Applied Clinical Medical Physics, 14 (2013) 173-186.

[129] S. Aran, L. Daftari Besheli, M. Karcaaltincaba, R. Gupta, E.J. Flores, H.H. Abujudeh, Applications of Dual-Energy CT in Emergency Radiology, American Journal of Roentgenology, 202 (2014) W314-W324.

[130] M.R.P. Homem, N.D.A. Mascarenhas, P.E. Cruvinel, The linear attenuation coefficients as features of multiple energy CT image classification, Nuclear Instruments and Methods in Physics Research A 452 (2000) 351-360.

[131] H.Q. Le, S. Molloi, Least squares parameter estimation methods for material decomposition with energy discriminating detectors, Medical Physics, 38 (2011) 245-255.

[132] S. Faby, S. Kuchenbecker, S. Sawall, D. Simons, H.-P. Schlemmer, M. Lell, M. Kachelrieß, Performance of today's dual energy CT and future multi energy CT in virtual non-contrast imaging and in iodine quantification: A simulation study, Medical Physics, 42 (2015) 4349-4366.

[133] N.M. Kulkarni, D.F. Pinho, A.R. Kambadakone, D.V. Sahani, Emerging Technologies in CT- Radiation Dose Reduction and Dual-Energy CT, Seminars in Roentgenology, 48 (2013) 192-202.

[134] Y. Yao, A.S. Wang, N.J. Pelc, Efficacy of fixed filtration for rapid kVp-switching dual energy x-ray systems, Medical Physics, 41 (2014) 1-2.

[135] V. Rebuffel, J.M. Dinten, Dual-energy x-ray imaging: benefits and limits, Insight - Non-Destructive Testing and Condition Monitoring, 49 (2007) 589-594.

[136] S. Aran, K. Shaqdan, H. Abujudeh, Dual-energy computed tomography (DECT) in emergency radiology: basic principles, techniques, and limitations, Emergency Radiology, 21 (2014) 391-405.

[137] P.S. Timothy, C. Guang-Hong, Dual energy CT using slow kVp switching acquisition and prior image constrained compressed sensing, Physics in Medicine and Biology, 55 (2010) 6411.

[138] H. Alkadhi, S. Leschka, Dual-energy CT: Principles, clinical value and potential applications in forensic imaging, Journal of Forensic Radiology and Imaging, 1 (2013) 180-185.

[139] S. Masetti, M. Fiaschetti, A. Turco, L. Roma, P.L. Rossi, M. Mariselli, N. Lanconelli, G. Baldazzi, Development of a multi-energy CT for small animals: characterization of the quasi-monochromatic x-ray source, IEEE Transactions on Nuclear Science, 56 (2009) 29-35.

[140] C.-H. Baek, D. Kim, X-ray beam design for multi-energy imaging with charge-integrating detector: A simulation study, Nuclear Instruments and Methods in Physics Research A 799 (2015) 132-136.

[141] D. Kim, S. Lee, P.H. Jeon, Experimental results of use of triple-energy x-ray beam with K-edge filter in multi-energy imaging, Journal of Instrumentation, 11 (2016) 1-11.

[142] F.A. Dilmanian, X.Y. Wu, E.C. Parsons, B. Ren, J. Kress, T.M. Button, L.D. Chapman, J.A. Coderre, F. Giron, D. Greenberg, D.J. Krus, Z. Liang, S. Marcovici, M.J. Petersen, C.T. Roque, M. Shleifer, D.N. Slatkin, W.C. Thomlinson, K. Yamamoto, Z. Zhong,

Single- and dual-energy CT with monochromatic synchrotron x-rays, Physics in Medicine and Biology, 42 (1997) 371-387.

[143] F. Arfelli, Synchrotron light and imaging systems for medical radiology, Nuclear Instruments and Methods in Physics Research A 454 (2000) 11-25.

[144] S. Puong, R. Iordache, X. Bouchevreau, S. Muller, Dual-energy contrast enhanced digital mammography: theoretical and experimental study of optimal monoenergetic beam parameters using synchrotron radiation, Proceedings of SPIE, 7258 (2009), 1-10.

[145] R. Mokso, P. Oberta, Simultaneous dual-energy X-ray stereo imaging, Journal of Synchrotron Radiation, 22 (2015) 1078-1082.

[146] R.J. Warp, J.T. Dobbins, Quantitative evaluation of noise reduction strategies in dual-energy imaging, Medical Physics, 30 (2003) 190-198.

[147] J.H. Siewerdsen, N.A. Shkumat, A.C. Dhanantwari, D.B. Williams, S. Richard, M.J. Daly, N.S. Paul, D.J. Moseley, D.A. Jaffray, J. Yorkston, R.V. Metter, High-performance dual-energy imaging with a flat-panel detector: Imaging physics from blackboard to benchtop to bedside, Proceedings of SPIE 6142, (2006) 1-10.

[148] X. Wang, D. Meier, S. Mikkelsen, G.E. Maehlum, D.J. Wagenaar, B.M.W. Tsui, B.E. Patt, E.C. Frey, MicroCT with energy-resolved photon-counting detectors, Physics in Medicine and Biology, 56 (2011) 2791-2816.

[149] K. Taguchi, J.S. Iwanczyk, Vision 20/20: Single photon counting x-ray detectors in medical imaging, Medical Physics, 40 (2013) 1-19.

[150] J. Tanguay, S. Yun, H.K. Kim, I.A. Cunningham, Detective quantum efficiency of photon-counting x-ray detectors, Medical Physics, 42 (2015) 491-509.

[151] R. Ballabriga, M. Campbell, E.H.M. Heijne, X. Llopart, L. Tlustos, The Medipix3 prototype, a pixel readout chip working in single photon counting mode with improved spectrometric performance, IEEE Transactions on Nuclear Science, 54 (2007) 1824-1829.

[152] M.S. Polad, Soft tissue imaging with photon counting spectroscopic CT, Physics in Medicine and Biology, 60 (2015) 2453-2474.

[153] X. Wang, D. Meier, K. Taguchi, D.J. Wagenaar, B.E. Patt, E.C. Frey, Material separation in x-ray CT with energy resolved photon-counting detectors, Medical Physics, 38 (2011) 1534-1546.

[154] J.L. Ducote, T. Xu, S. Molloi, Optimization of a flat-panel based real time dual-energy system for cardiac imaging, Medical Physics, 33 (2006) 1562-1568.

[155] J.C. Han, H.K. Kim, D.W. Kim, S. Yun, H. Youn, S. Kam, J. Tanguay, I.A. Cunningham, Single-shot dual-energy x-ray imaging with a flat-panel sandwich detector for preclinical imaging, Current Applied Physics, 14 (2014) 1734-1742.

[156] S.N. Fedotov, N.G. Volkov, Analysis of the pulse-height spectra distortion caused by the pile-up effect, Nuclear Instruments and Methods, 122 (1974) 463-465.

[157] S. Pommé, Cascades of pile-up and dead time, Applied Radiation and Isotopes, 66 (2008) 941-947.

[158] A.S. Wang, D. Harrison, V. Lobastov, J.E. Tkaczyk, Pulse pileup statistics for energy discriminating photon counting x-ray detectors, Medical Physics, 38 (2011) 4265-4275.

[159] U.W. Arndt, Counting losses of detectors for x-rays from storage rings, Journal of Physics E: Scientific Instruments, 11 (1978) 671-673.

[160] C.H. Westcott, A study of expected loss rates in the counting of particles from pulsed sources, Proceedings of the Royal Society of London. Series A. Mathematical and Physical Sciences, 194 (1948) 508-526.

[161] J.E. Bateman, The effect of beam time structure on counting detectors in SRS experiments, Journal of Synchrotron Radiation, 7 (2000) 307-312.

[162] V. Honkimaki, P. Suortti, Energy-dispersive diffraction with synchrotron radiation and a germanium detector, Journal of Synchrotron Radiation, 14 (2007) 331-338.

[163] T. Hatsui, H. Graafsma, X-ray imaging detectors for synchrotron and XFEL sources, International Union of Crystallography Journal, 2 (2015) 371-383.

[164] N. Kozul, G.R. Davis, P. Anderson, J.C. Elliott, Elemental quantification using multiple-energy x-ray absorptiometry, Measurement Science and Technology, 10 (1999) 252-259.

[165] Y. Zhu, Bent Laue crystals in biomedical x-ray imaging applications, Division of Biomedical Engineering, University of Saskatchewan, 2012.

[166] M.H. Van Benthem, M.R. Keenan, Fast algorithm for the solution of large-scale non-negativity-constrained least squares problems, Journal of Chemometrics, 18 (2004) 441-450.

[167] D. Chen, R.J. Plemmons, Nonnegativity constraints in numerical analysis, in: A. Bultheel, R. Cools (Eds.) The Birth of Numerical Analysis, World Scientific Publishing Co. Pte. Ltd, Singapore, 2010.

[168] R. Bro, S.D. Jong, A fast non-negativity-constrained least squares algorithm, Journal of Chemometrics, 11 (1997) 393-401.

[169] W. Gander, M.J. Gander, F. Kwok, Scientific Computing - An Introduction using Maple and MATLAB, Springer Internaional Publishing, Switzerland, 2014.

[170] Y. Luo, R. Duraiswami, Efficient parallel nonnegative least squares on multicore architecture, SIAM Journal on Scientific Computing, 33 (2011) 2848-2863.

[171] P. Désesquelles, T.M.H. Ha, A. Korichi, F.L. Blanc, C.M. Petrache, NNLC: non-negative least chi-square minimization and application to HPGe detectors, Journal of Physics G: Nuclear and Particle Physics, 36 (2009) 1-7.

[172] D.C. Heinz, I.C. Chein, Fully constrained least squares linear spectral mixture analysis method for material quantification in hyperspectral imagery, IEEE Transactions on Geoscience and Remote Sensing, 39 (2001) 529-545.

[173] A. Panahifar, T.M. Swanston, M.J. Pushie, G. Belev, D. Chapman, L. Weber, D.M.L. Cooper, Three-dimensional labeling of newly formed bone using synchrotron radiation barium K-edge subtraction imaging, Physics in Medicine and Biology, 61 (2016) 5077-5088.

[174] P. Deman, S. Tan, G. Belev, N. Samadi, M. Martinson, D. Chapman, N.L. Ford, Respiratory-gated KES imaging of a rat model of acute lung injury at the Canadian Light Source, Journal of Synchrotron Radiation, 24 (2017) 679-685.

[175] C. Hall, D. Hausermann, A. Maksimenko, A. Astolfo, K. Siu, J. Pearson, A. Stevenson, Detectors for the Imaging and Medical Beam Line at the Australian Synchrotron, Journal of Instrumentation, 8 (2013) 1-5.

[176] V. Bellucci, V. Guidi, R. Camattari, I. Neri, Calculation of diffraction efficiency for curved crystals with arbitrary curvature radius, Journal of Applied Crystallography, 46 (2013) 415-420.

[177] B. Bassey, M. Mercedes, N. Samadi, G. Belev, C. Karanfil, D. Chapman, Multiple energy synchrotron biomedical imaging system- preliminary results, in: D.A. Jaffray (Ed.) World Congress on Medical Physics and Biomedical Engineering, June 7-12, 2015, Toronto, Canada, Springer International Publishing, 2015, 248-251.

[178] B. Bassey, M. Martinson, N. Samadi, G. Belev, C. Karanfil, P. Qi, D. Chapman, Multiple energy synchrotron biomedical imaging system, Physics in Medicine and Biology, 61 (2016) 8180-8198.

[179] A. Mittone, F. Baldacci, A. Bravin, E. Brun, F. Delaire, C. Ferrero, S. Gasilov, N. Freud, J.M. Letang, D. Sarrut, F. Smekens, P. Coan, An efficient numerical tool for dose deposition prediction applied to synchrotron medical imaging and radiation therapy, Journal of Synchrotron Radiation, 20 (2013) 785-792.

[180] W. Zbijewski, G.J. Gang, J. Xu, A.S. Wang, J.W. Stayman, K. Taguchi, J.A. Carrino, J.H. Siewerdsen, Dual-energy cone-beam CT with a flat-panel detector: effect of reconstruction algorithm on material classification, Medical Physics, 41 (2014) 1-15.

[181] E. Roessl, A. Thran, G. Martens, T. Istel, R. Proksa, J.P. Schlomka, Dual-energy x-ray imaging by simultaneous integration and campbelling readout, IEEE Nuclear Science Symposium Conference Record (NSS/MIC), 2010, 2112-2115.

[182] E. Roessl, C. Herrmann, Cramér-Rao lower bound of basis image noise in multiple-energy x-ray imaging, Physics in Medicine and Biology, 54 (2009) 1307-1318.

[183] L.J. Erasmus, D. Hurter, M. Naude, H.G. Kritzinger, S. Acho, A short overview of MRI artefacts, South African Journal of Radiology, 8 (2004) 13-17.

[184] C.E. Willis, S.K. Thompson, S.J. Shepard, Artifacts and misadventures in digital radiography, Applied Radiology, 33 (2004) 11-20.

[185] C.M. Shetty, A. Barthur, A. Kambadakone, N. Narayanan, R. Kv, Computed radiography image artifacts revisited, American Journal of Roentgenology, 196 (2011) W37-W47.

[186] W.R. Geiser, T.M. Haygood, L. Santiago, T. Stephens, D. Thames, G.J. Whitman, Challenges in Mammography: Part 1, Artifacts in digital mammography, American Journal of Roentgenology, 197 (2011) W1023-W1030.

[187] S.L. Solomon, R.G. Jost, H.S. Glazer, S.S. Sagel, D.J. Anderson, P.L. Molina, Artifacts in computed radiography, American Journal of Roentgenology, 157 (1991) 181-185.

[188] F.E. Boas, D. Fleischmann, CT artifacts: causes and reduction techniques, Imaging in Medicine, 4 (2012) 229-240.

[189] D.A. Jiménez, L.J. Armbrust, R.T. O'Brien, D.S. Biller, Artifacts in digital radiography, Veterinary Radiology & Ultrasound, 49 (2008) 321-332.

[190] R. Schulze, U. Heil, D. Gross, D.D. Bruellmann, E. Dranischnikow, U. Schwanecke, E. Schoemer, Artefacts in CBCT: a review, Dento Maxillo Facial Radiology, 40 (2011) 265-273.

[191] Mehran Yazdi, L. Beaulieu, Artifacts in spiral x-ray CT scanners: problems and solutions, International Journal of Electrical, Computer, Energetic, Electronic and Communication Engineering, 1 (2007) 1599-1603.

[192] L.J. Cesar, B.A. Schueler, F.E. Zink, T.R. Daly, J.P. Taubel, L.L. Jorgenson, Artefacts found in computed radiography, The British Journal of Radiology, 74 (2001) 195-202.

[193] W. Sureshbabu, O. Mawlawi, PET/CT imaging artifacts, Journal of Nuclear Medicine Technology, 33 (2005) 156-161; quiz 163-154.

[194] T.M. Blodgett, A.S. Mehta, A.S. Mehta, C.M. Laymon, J. Carney, D.W. Townsend, PET/CT artifacts, Clinical Imaging, 35 (2011) 49-63.

[195] C. Pettinato, C. Nanni, M. Farsad, P. Castellucci, A. Sarnelli, S. Civollani, R. Franchi, S. Fanti, M. Marengo, C. Bergamini, Artefacts of PET/CT images, Biomedical Imaging and Intervention Journal, 2 (2006) 1-7.

[196] K. Krupa, M. Bekiesińska-Figatowska, Artifacts in magnetic resonance imaging, Polish Journal of Radiology, 80 (2015) 93-106.

[197] E. Pusey, R.B. Lufkin, R.K. Brown, M.A. Solomon, D.D. Stark, R.W. Tarr, W.N. Hanafee, Magnetic resonance imaging artifacts: mechanism and clinical significance, RadioGraphics, 6 (1986) 891-911.

[198] J. Zhuo, R.P. Gullapalli, MR artifacts, safety, and quality control, RadioGraphics, 26 (2006) 275-297.

[199] R.S. Ayyala, M. Chorlton, R.H. Behrman, P.J. Kornguth, P.J. Slanetz, Digital mammographic artifacts on full-field systems: what are they and how do I fix them?, RadioGraphics, 28 (2008) 1999-2008.

[200] J.J. Choi, S.H. Kim, B.J. Kang, B.G. Choi, B. Song, H. Jung, Mammographic artifacts on full-field digital mammography, Journal of Digital Imaging, 27 (2014) 231-236.

[201] C. Van Ongeval, J. Jacobs, H. Bosmans, Artifacts in digital mammography, Journal Belge de Radiologie-Belgisch Tijdschrift voor Radiogi, 91 (2008) 262-263.

[202] L. Chaloeykitti, M. Muttarak, K.H. Ng, Artifacts in mammography: ways to identify and overcome them, Singapore Medical Journal, 47 (2006) 634-640; quiz 641.

[203] M.K. Feldman, S. Katyal, M.S. Blackwood, US Artifacts, RadioGraphics, 29 (2009) 1179-1189.

[204] F.W. Kremkau, K.J. Taylor, Artifacts in ultrasound imaging, Journal of ultrasound in medicine : official journal of the American Institute of Ultrasound in Medicine, 5 (1986) 227-237.

[205] R.M. Kirberger, Imaging artifacts in diagnostic ultrasound-a review, Veterinary Radiology & Ultrasound, 36 (1995) 297-306.

[206] H.D. Zeman, Imaging apparatus and techniques for synchrotron radiation angiography, in: S. Ebashi, M. Koch, E. Rubenstein (Eds.) Handbook on Synchrotron Radiation, Elsvier Science Publishers B. V., North-Holland, 1991.

[207] H.D. Zeman, H.R. Moulin, Removal of harmonic artifacts from synchrotron radiation coronary angiograms, IEEE Nuclear Science Symposium and Medical Imaging Conference, vol. 1823, 1991, 1826-1830.

[208] B. Bertrand, F. Esteve, H. Elleaume, C. Nemoz, S. Fiedler, A. Bravin, G. Berruyer, T. Brochard, M. Renier, J. Machecourt, W. Thomlinson, J.F. Le Bas, Comparison of synchrotron radiation angiography with conventional angiography for the diagnosis of in-stent restenosis after percutaneous transluminal coronary angioplasty, European Heart Journal, 26 (2005) 1284-1291.

[209] L. Xiaoxia, Z. Jun, S. Jianqi, G. Xiang, X. Tiqiao, L. Ping, X.X. Lisa, Lung cancer and angiogenesis imaging using synchrotron radiation, Physics in Medicine and Biology, 55 (2010) 2399-2409.

[210] Z. Zhong, D. Chapman, R. Menk, J. Richardson, S. Theophanis, W. Thomlinson, Monochromatic energy-subtraction radiography using a rotating anode source and a bent Laue monochromator, Physics in Medicine and Biology, 42 (1997) 1751.

[211] F. Biggs, R. Lighthill, Analytical approximations for x-ray cross sections III, SANDIA Report, Sandia National Laboratory, California, United States, 1988, 1-141.

APPENDIX A
COPYRIGHTS FROM PUBLISHED WORK

An academic journal article and a conference paper have been published based on this research work. For the article, Ref. [178], published in the academic journal-Physics in Medicine and Biology (PMB), I have the right to include all or part of the article in this thesis. Also, I have secured the permissions (copyrights) to reuse figures from work published by other people in this thesis. These are as summarized in Table A .1, followed by the licenses/permissions.

Table A.1. Licenses to reuse paper and figures that have already been published.

License Number	Article Reference	Author	Reuse content	Reuse location in this thesis
Appendix A.1	[178]	B. Bassey et al.	Full article with modifications	Chapters 1, 3, 4, 5, and 7
Appendix A.2	[54]	V. Bellucci et al.	Figure 3	Figure 3.6
Appendix A.3	[56]	R. Smither et al.	Figure 2	Figure 3.7
Appendix A.4	[84]	G. Illing et al.	Figure 2	Figure 3.8
Appendix A.5	[97]	H. Suhonen et al.	Figure 1	Figure 3.10
Appendix A.6	[90]	Y. Zhu et al.	Figure 1	Figure 3.11
Appendix A.7	[139]	S. Masetti et al.	Figure 1	Figure 4.4
Appendix A.8	[177]	B. Bassey et al.	Figures 1 and 4	Figures 3.2 and 5.7b
Appendix A.9	[208]	B. Bertrand et al.	Figure 1(E)	Figure 6.3
Appendix A.10	[96]	J. Giacomini et al.	Figure 3(a)	Figure 6.4

Appendix A.1

Assignment of copyright and publication agreement

IOP Publishing Limited ("IOP") agrees on behalf of the Institute of Physics and Engineering in Medicine ("IPEM") to publish:

Manuscript Title: Multiple energy synchrotron biomedical imaging system (the "Article") written by

Names of all authors: Bassey, Bassey; Martinson, Mercedes; Samadi, Nazanin; Belev, George; Karanfil, Cahit; Qi, peng; Chapman, Dean ("the Named Authors") in the following journal Physics in Medicine and Biology ("the Journal")

Name of copyright owner(s) (if not the Named Author(s) – see Important Information above):

("the Institution")

IOP Ref: PMB-104334

Part 1 - Subscription Copyright Assignment

Assignment of copyright

1.1 In consideration for acceptance and publication of the Article, the Named Authors of the Article and/or the Institution hereby assign, where necessary by present assignment of future copyright, to IPEM with full title guarantee the entire copyright in all original material published as part of the Article (which expression includes but is not limited to the text, abstract, tables, figures and graphs, related corrigenda or "comments" and multimedia content but excludes any other item referred to as supplementary material) throughout the world for the full term of copyright (including any extensions or renewals thereof) for all media and formats, whether known or unknown. Such assignment shall be effective only if the Article (or any resubmission of the Article) is accepted for publication. For the avoidance of doubt, copyright does not subsist in any fundamental data underlying the Article and nothing in this agreement is intended to limit access to or use of such data.

1.2 If the Article, or any part of it, is protected by Crown Copyright, in consideration for acceptance and publication of the Article, the relevant Named Authors and the relevant originating department or agency hereby grant IOP and IPEM a royalty-free worldwide freely-transferrable licence for the full term of copyright (including any extensions or renewals thereof) for all media and formats, whether known or unknown, to do in relation to the Article all acts restricted by copyright worldwide including, but not limited to, the right of action under section 101A of the Copyright Designs and Patents Act 1988. Such licence shall be effective only if the Article is accepted for publication and shall be exclusive to IOP and IPEM for a period of twelve calendar months following the date of online publication of the Article. Thereafter, the licence shall be non-exclusive.

1.3 In consideration for acceptance and publication of the Article, the Named Authors and/or the Institution hereby grant IOP and IPEM a royalty-free non-exclusive worldwide freely transferrable licence for the full term of copyright (including any extensions or renewals thereof) to do in relation to any supplementary material not deemed to be part of the Article and/or any video abstract all acts restricted by copyright worldwide. This shall include, but not be limited to, making the material available under any licence that IOP or IPEM deems appropriate for purposes including, but not limited to, the maximisation of visibility and the long term preservation of the content.

1.4 Each of the Named Authors consents to the publication and processing by IOP and IPEM of their email addresses.

Appendix A.2

SPRINGER LICENSE
TERMS AND CONDITIONS

Aug 08, 2017

This Agreement between Bassey Bassey ("You") and Springer ("Springer") consists of your license details and the terms and conditions provided by Springer and Copyright Clearance Center.

License Number	4164301236830
License date	Aug 08, 2017
Licensed Content Publisher	Springer
Licensed Content Publication	Experimental Astronomy
Licensed Content Title	Self-standing bent silicon crystals for very high efficiency Laue lens
Licensed Content Author	Valerio Bellucci
Licensed Content Date	Jan 1, 2011
Licensed Content Volume	31
Licensed Content Issue	1
Type of Use	Thesis/Dissertation
Portion	Figures/tables/illustrations
Number of figures/tables/illustrations	1
Author of this Springer article	No
Order reference number	
Original figure numbers	Figure 3
Title of your thesis / dissertation	Development of a multiple energy synchrotron biomedical imaging system
Expected completion date	Aug 2017
Estimated size(pages)	135
Requestor Location	Bassey Bassey 15-310 Clarence Avenue South Saskatoon, SK S7N1H6 Canada Attn: Bassey Bassey
Billing Type	Invoice
Billing Address	Bassey Bassey 802 Arlington Avenue Saskatoon, SK S7H2X4 Canada Attn: Bassey Bassey
Total	0.00 CAD
Terms and Conditions	

Appendix A.3

SPRINGER LICENSE
TERMS AND CONDITIONS

Aug 08, 2017

This Agreement between Bassey Bassey ("You") and Springer ("Springer") consists of your license details and the terms and conditions provided by Springer and Copyright Clearance Center.

License Number	4164290398810
License date	Aug 08, 2017
Licensed Content Publisher	Springer
Licensed Content Publication	Springer eBook
Licensed Content Title	High diffraction efficiency, broadband, diffraction crystals for use in crystal diffraction lenses
Licensed Content Author	Robert K. Smither
Licensed Content Date	Jan 1, 2006
Type of Use	Thesis/Dissertation
Portion	Figures/tables/illustrations
Number of figures/tables/illustrations	2
Author of this Springer article	No
Order reference number	
Original figure numbers	Figure 2: (a) and (b)
Title of your thesis / dissertation	Development of a multiple energy synchrotron biomedical imaging system
Expected completion date	Aug 2017
Estimated size(pages)	135
Requestor Location	Bassey Bassey 15-310 Clarence Avenue South Saskatoon, SK S7N1H6 Canada Attn: Bassey Bassey
Billing Type	Invoice
Billing Address	Bassey Bassey 802 Arlington Avenue Saskatoon, SK S7H2X4 Canada Attn: Bassey Bassey
Total	0.00 CAD
Terms and Conditions	

Introduction
The publisher for this copyrighted material is Springer. By clicking "accept" in connection

Appendix A.4

AIP PUBLISHING LLC LICENSE
TERMS AND CONDITIONS

Aug 08, 2017

This Agreement between Bassey Bassey ("You") and AIP Publishing LLC ("AIP Publishing LLC") consists of your license details and the terms and conditions provided by AIP Publishing LLC and Copyright Clearance Center.

License Number	4164280927104
License date	Aug 08, 2017
Licensed Content Publisher	AIP Publishing LLC
Licensed Content Publication	Review of Scientific Instruments
Licensed Content Title	Double beam bent Laue monochromator for coronary angiography
Licensed Content Author	G. Illing, J. Heuer, B. Reime, et al
Licensed Content Date	Feb 1, 1995
Licensed Content Volume	66
Licensed Content Issue	2
Type of Use	Thesis/Dissertation
Requestor type	Student
Format	Electronic
Portion	Figure/Table
Number of figures/tables	2
Title of your thesis / dissertation	Development of a multiple energy synchrotron biomedical imaging system
Expected completion date	Aug 2017
Estimated size (number of pages)	135
Requestor Location	Bassey Bassey 15-310 Clarence Avenue South Saskatoon, SK S7N1H6 Canada Attn: Bassey Bassey
Billing Type	Invoice
Billing Address	Bassey Bassey 802 Arlington Avenue Saskatoon, SK S7H2X4 Canada Attn: Bassey Bassey
Total	0.00 CAD

Terms and Conditions

AIP Publishing LLC -- Terms and Conditions: Permissions Uses

AIP Publishing hereby grants to you the non-exclusive right and license to use and/or distribute the Material according to the use specified in your order, on a one-time basis, for the specified

Appendix A.5

Fw: Permission to Use Figure and Table from PMB Journal

Kathryn Shaw <Kathryn.Shaw@iop.org> on behalf of Permissions <permissions@iop.org>

Fri 10/28/2016 4:56 AM

To:Bassey, Bassey <beb074@campus.usask.ca>;

Dear Bassey Bassey,

Thank you for your request to reproduce IOP Publishing material in your thesis.

Regarding:

Figure 1 and Table 1 (H Suhonen et al 2008 Phys. Med. Biol. 53 775)

We are happy to grant permission for the use you request on the terms set out below.

Conditions

Non-exclusive, non-transferrable, revocable, worldwide, permission to use the material in print and electronic form will be granted **subject to the following conditions:**

- Permission will be cancelled without notice if you fail to fulfil any of the conditions of this letter.
- You will make reasonable efforts to contact the author(s) to seek consent for your intended use. Contacting one author acting expressly as authorised agent for their co-authors is acceptable.
- You will reproduce the following prominently alongside the material:
  - the source of the material, including author, article title, title of journal, volume number, issue number (if relevant), page range (or first page if this is the only information available) and date of first publication. This information can be contained in a footnote or reference note; or
  - a link back to the article (via DOI); and
  - if practical and IN ALL CASES for works published under any of the Creative Commons licences the words "© Institute of Physics and Engineering in Medicine. Reproduced by permission of IOP Publishing. All rights reserved."
- The material will not, without the express permission of the author(s), be used in any way which, in the opinion of IOP Publishing, could distort or alter the author(s)' original intention(s) and meaning, be prejudicial to the honour or reputation of the author(s) and/or imply endorsement by the author(s) and/or IOP Publishing.
- Payment of £0 is received in full by IOP Publishing prior to use.

This permission does not apply to any material/figure which is credited to another source in our publication or has been obtained from a third party. Express permission for such materials/figures must be obtained from the copyright owner.

If you have any questions, please feel free to contact our Permissions team at permissions@iop.org.

I should be grateful if you would acknowledge receipt of this email.

Kind regards,

Kathryn Shaw

Copyright & Permissions Team
Gemma Alaway – Rights & Permissions Adviser
Kathryn Shaw - Editorial Assistant

Contact Details
E-mail: permissions@iop.org

For further information: http://iopscience.iop.org/page/copyright

Please see our Author Rights Policy http://ioppublishing.org/author-rights/

Please note: We do not provide signed permission forms as a separate attachment. Please print this email and provide it to your institution as proof of permission.

Please note: Any statements made by IOP Publishing to the effect that authors do not need to get permission to use any content are not intended to constitute any sort of legal advice. Authors must make their own decisions as to the suitability of the content they are using and whether they require permission for it to be published within their article.

Appendix A.6

Re: A Request for Permission to Reuse a Figure

Christina Colwell <Christina.Colwell@iop.org> on behalf of Permissions <permissions@iop.org>

Wed 8/9/2017 3:45 AM

To: Bassey, Bassey <beb074@campus.usask.ca>;

Dear Bassey Bassey,

Thank you for your request to reproduce IOP Publishing material ***in your thesis.***

Regarding:

Figure 1 Spectral K-edge subtraction imaging (Y Zhu et al. 2014 Phys. Med. Biol. 59 2485),

We are happy to grant permission for the use you request on the terms set out below.

Conditions

Non-exclusive, non-transferrable, revocable, worldwide, permission to use the material in print and electronic form will be granted **subject to the following conditions:**

- Permission will be cancelled without notice if you fail to fulfil any of the conditions of this letter.
- You will reproduce the following prominently alongside the material:

o the source of the material, including author, article title, title of journal, volume number, issue number (if relevant), page range (or first page if this is the only information available) and date of first publication. This information can be contained in a footnote or reference note; or

o a link back to the article (via DOI); and

o ***if practical and IN ALL CASES for works published under any of the Creative Commons licences the words "© Institute of Physics and Engineering in Medicine. Reproduced by permission of IOP Publishing. All rights reserved"***

- The material will notbe used in any way which, in the opinion of IOP Publishing, could distort or alter the original intention(s) and meaning, be prejudicial to the honour or reputation of and/or imply endorsement by the author(s) and/or IOP Publishing.
- Payment of £0 is received in full by IOP Publishing prior to use.

This permission does not apply to any material/figure which is credited to another source in our publication or has been obtained from a third party. Express permission for such materials/figures must be obtained from the copyright owner.

Special Conditions – For STM Signatories ONLY (as agreed as part of the STM Guidelines)

Any permissions granted for a particular edition will apply also to subsequent editions and for editions in other languages, provided such editions are for the work as a whole in situ and does not involve the separate exploitation of the permitted illustrations or excerpts.

I should be grateful if you would acknowledge receipt of this email.

Kind regards

Christina

Copyright & Permissions Team
Gemma Alaway – Senior Rights & Permissions Adviser
Christina Colwell - Rights & Permissions Assistant

Contact Details
E-mail: permissions@iop.org

For further information about copyright and how to request permission: http://iopscience.iop.org/page/copyright

Please see our Author Rights Policy http://ioppublishing.org/author-rights/

Please note: We do not provide signed permission forms as a separate attachment. Please print this email and provide it to your publisher as proof of permission.

Please note: Any statements made by IOP Publishing to the effect that authors do not need to get permission to use any content where IOP Publishing is not the publisher is not intended to constitute any sort of legal advice. Authors must make their own decisions as to the suitability of the content they are using and whether they require permission for it to be published within their article.

Appendix A.7

Thesis / Dissertation Reuse

The IEEE does not require individuals working on a thesis to obtain a formal reuse license, however, you may print out this statement to be used as a permission grant:

Requirements to be followed when using any portion (e.g., figure, graph, table, or textual material) of an IEEE copyrighted paper in a thesis:

1) In the case of textual material (e.g., using short quotes or referring to the work within these papers) users must give full credit to the original source (author, paper, publication) followed by the IEEE copyright line © 2011 IEEE.
2) In the case of illustrations or tabular material, we require that the copyright line © [Year of original publication] IEEE appear prominently with each reprinted figure and/or table.
3) If a substantial portion of the original paper is to be used, and if you are not the senior author, also obtain the senior author's approval.

Requirements to be followed when using an entire IEEE copyrighted paper in a thesis:

1) The following IEEE copyright/ credit notice should be placed prominently in the references: © [year of original publication] IEEE. Reprinted, with permission, from [author names, paper title, IEEE publication title, and month/year of publication]
2) Only the accepted version of an IEEE copyrighted paper can be used when posting the paper or your thesis on-line.
3) In placing the thesis on the author's university website, please display the following message in a prominent place on the website: In reference to IEEE copyrighted material which is used with permission in this thesis, the IEEE does not endorse any of [university/educational entity's name goes here]'s products or services. Internal or personal use of this material is permitted. If interested in reprinting/republishing IEEE copyrighted material for advertising or promotional purposes or for creating new collective works for resale or redistribution, please go to http://www.ieee.org/publications_standards/publications/rights/rights_link.html to learn how to obtain a License from RightsLink.

If applicable, University Microfilms and/or ProQuest Library, or the Archives of Canada may supply single copies of the dissertation.

BACK CLOSE WINDOW

Appendix A.8

SPRINGER LICENSE
TERMS AND CONDITIONS

Aug 09, 2017

This Agreement between Bassey Bassey ("You") and Springer ("Springer") consists of your license details and the terms and conditions provided by Springer and Copyright Clearance Center.

License Number	4164971032801
License date	Aug 09, 2017
Licensed Content Publisher	Springer
Licensed Content Publication	Springer eBook
Licensed Content Title	Multiple Energy Synchrotron Biomedical Imaging System-Preliminary Results
Licensed Content Author	B. Bassey
Licensed Content Date	Jan 1, 2015
Type of Use	Thesis/Dissertation
Portion	Figures/tables/illustrations
Number of figures/tables/illustrations	3
Author of this Springer article	Yes and you are the sole author of the new work
Order reference number	
Original figure numbers	Figures 1, 2 and 4
Title of your thesis / dissertation	Development of a multiple energy synchrotron biomedical imaging system
Expected completion date	Aug 2017
Estimated size(pages)	135
Requestor Location	Bassey Bassey 15-310 Clarence Avenue South Saskatoon, SK S7N1H6 Canada Attn: Bassey Bassey
Billing Type	Invoice
Billing Address	Bassey Bassey 802 Arlington Avenue Saskatoon, SK S7H2X4 Canada Attn: Bassey Bassey
Total	0.00 CAD
Terms and Conditions	

Introduction
The publisher for this copyrighted material is Springer. By clicking "accept" in connection

Appendix A.9

OXFORD UNIVERSITY PRESS LICENSE
TERMS AND CONDITIONS

Aug 10, 2017

This Agreement between Bassey Bassey ("You") and Oxford University Press ("Oxford University Press") consists of your license details and the terms and conditions provided by Oxford University Press and Copyright Clearance Center.

License Number	4165521447409
License date	Aug 10, 2017
Licensed content publisher	Oxford University Press
Licensed content publication	European Heart Journal
Licensed content title	Comparison of synchrotron radiation angiography with conventional angiography for the diagnosis of in-stent restenosis after percutaneous transluminal coronary angioplasty
Licensed content author	Bertrand, Bernard; Estève, François
Licensed content date	Feb 25, 2005
Type of Use	Thesis/Dissertation
Institution name	
Title of your work	Development of a multiple energy synchrotron biomedical imaging system
Publisher of your work	n/a
Expected publication date	Aug 2017
Permissions cost	0.00 CAD
Value added tax	0.00 CAD
Total	0.00 CAD
Requestor Location	Bassey Bassey 15-310 Clarence Avenue South Saskatoon, SK S7N1H6 Canada Attn: Bassey Bassey
Publisher Tax ID	GB125506730
Billing Type	Invoice
Billing Address	Bassey Bassey 802 Arlington Avenue Saskatoon, SK S7H2X4 Canada Attn: Bassey Bassey
Total	0.00 CAD
Terms and Conditions	

STANDARD TERMS AND CONDITIONS FOR REPRODUCTION OF MATERIAL FROM AN OXFORD UNIVERSITY PRESS JOURNAL

1. Use of the material is restricted to the type of use specified in your order details.

Appendix A.10

ELSEVIER LICENSE
TERMS AND CONDITIONS

Aug 10, 2017

This Agreement between Bassey Bassey ("You") and Elsevier ("Elsevier") consists of your license details and the terms and conditions provided by Elsevier and Copyright Clearance Center.

License Number	4165530462495
License date	Aug 10, 2017
Licensed Content Publisher	Elsevier
Licensed Content Publication	Nuclear Instruments and Methods in Physics Research Section A: Accelerators, Spectrometers, Detectors and Associated Equipment
Licensed Content Title	Bronchial imaging in humans using xenon K-edge dichromography
Licensed Content Author	J.C Giacomini,H Gordon,R O'Neil,A Van Kessel,B Cason,D Chapman,W Lavendar,N Gmur,R Menk,W Thomlinson,Z Zhong,E Rubenstein
Licensed Content Date	Apr 11, 1998
Licensed Content Volume	406
Licensed Content Issue	3
Licensed Content Pages	6
Start Page	473
End Page	478
Type of Use	reuse in a thesis/dissertation
Intended publisher of new work	other
Portion	figures/tables/illustrations
Number of figures/tables/illustrations	1
Format	electronic
Are you the author of this Elsevier article?	No
Will you be translating?	No
Original figure numbers	Figure 3(a)
Title of your thesis/dissertation	Development of a multiple energy synchrotron biomedical imaging system
Expected completion date	Aug 2017
Estimated size (number of pages)	135
Requestor Location	Bassey Bassey 15-310 Clarence Avenue South Saskatoon, SK S7N1H6 Canada Attn: Bassey Bassey

APPENDIX B
MATERIAL DECOMPOSITION ALGORITHM

bassey_data_new_6_v2.pro

```
function bassey_data_new_6_v2, out_path=out_path, reverse_energy_direction=reverse_energy_direction, threshold=threshold, $
    use_tomos_for_flats=use_tomos_for_flats, use_before=use_before, use_after=use_after, use_average=use_average, use_linear=use_linear

if n_elements( threshold ) eq 0 then threshold = 0.5
;path = 'C:\Users\dec456\Dropbox\Bassey-shared with Prof Dean Chapman\On Energy Dispersive Imaging System\test object-Energy Dispersive Imaging System-March 13\'
path = 'C:\Users\Bassey Bassey\.idl\IDL Data\Energy Dispersive Biomedical Imaging System\Imaging\To be analysed\'
if n_elements(path) eq 0 then path = dialog_pickfile(/dir)
; path to flats, darks and edges
dark_path = path+'darks\'        & dark_files = file_search(dark_path,'*.tif') & dark = read_average_tifs(dark_files)
edge_path = path+'edges\'        & edge_files = file_search(edge_path,'*.tif') & edge = read_average_tifs(edge_files) - dark
tomo_path = path+'Tomos\'        & tomo_files = file_search(tomo_path,'*.tif') & ix   = n_elements(tomo_files)
flat_path = path+'more_flats\'
 linear_flat = 0
if keyword_set(use_tomos_for_flats) then begin
 nflts = 5
 flat_files_before = tomo_files(0       :nflts-1)
 flat_files_after  = tomo_files(ix-nflts:   ix-1)
 flat_before       = read_average_tifs(flat_files_before) - dark
 flat_after        = read_average_tifs(flat_files_after ) - dark
 flat_average      = 0.5*(flat_before+flat_after)
 sf = size(flat_before) & fnx = sf(1) & fny = sf(2) & nf = ix
 flats = fltarr(nf,fnx,fny)
 for i=0,nf-1 do flats(i,*,*) = flat_before + float(i)*(flat_after-flat_before)/float(nf-1)
 flat=flat_average
 if keyword_set(use_before ) then flat = flat_before
 if keyword_set(use_after  ) then flat = flat_after
 if keyword_set(use_average) then flat = flat_average
 if keyword_set(use_linear ) then begin
   flat        = flat_average
   linear_flat = 1
 endif
endif else begin
 flat_files = file_search(flat_path,'*.tif') & flat = read_average_tifs(flat_files) - dark
endelse

sz = size(dark) & nx = sz(1) & ny = sz(2)
b         = horizontal_vertical_beam_edges(flat, threshold) & beam      = b.beam
hbeam     = total(beam,2)      & vbeam = total(beam,1)
hbeam     = where(hbeam gt 0) & vbeam = where(vbeam gt 0)
top_clip  = min(b.top(hbeam)) & bot_clip  = max(b.bot(hbeam)) & left_clip = b.left & right_clip = b.right
c_flat    = flat(left_clip:right_clip,bot_clip:top_clip) & if linear_flat then c_flats = flats(*,left_clip:right_clip,bot_clip:top_clip)
c_dark    = dark(left_clip:right_clip,bot_clip:top_clip)
c_edge    = edge(left_clip:right_clip,bot_clip:top_clip)
csz       = size(c_flat) & cnx = csz(1) & cny = csz(2)
if keyword_set(reverse_energy_direction) then begin
 c_flat  = rotate(c_flat,5) & if linear_flat then for i=0,nf-1 do cflats(i,*,*) = rotate(reform(c_flats(i,*,*)),5)
 c_dark  = rotate(c_dark,5)
 c_edge  = rotate(c_edge,5)
endif
r_edge    = -alog(c_edge/c_flat)
e_info    = extract_energy_information_new(r_edge, /plot, out_path=out_path)
mrI       = e_info.mr1
mrBa      = e_info.mr2
mrW       = e_info.mrm
```

Page 1

```
55 mrB       = e_info.mrb
56 mrCs      = e_info.mr3
57 mrXe      = e_info.mr4
58 es        = e_info.es
59 mrsq      = make_square_average_murhos_new(mrI, mrBa, mrCs, mrXe, mrB, mrW, original=M)
60
61 ix      = n_elements(tomo_files)
62 iy      = cny
63 rtI     = fltarr(ix,iy) & rtBa   = fltarr(ix,iy) & rtCs   = fltarr(ix,iy) & rtXe   = fltarr(ix,iy) & rtB   = fltarr(ix,iy) & rtW   = fltarr(ix,iy)
64 rmrIs   = fltarr(ix,iy) & rmrBas = fltarr(ix,iy) & rmrCss = fltarr(ix,iy) & rmrXes = fltarr(ix,iy) & rmrBs = fltarr(ix,iy) & rmrWs = fltarr(ix,iy)
65 rs      = fltarr(ix,cnx,iy)
66 uy        = fltarr(cny)+1.0
67 for i=0,ix-1 do begin
68   raw        = float(read_tiff(tomo_files(i))) - dark
69   c_raw      = raw(left_clip:right_clip,bot_clip:top_clip)
70   if keyword_set(reverse_energy_direction) then c_raw  = rotate(c_raw,5)
71   if NOT linear_flat then r = -alog(c_raw/c_flat)
72   if     linear_flat then r = -alog(c_raw/reform(c_flats(i,*,*)))
73   rs(i,*,*)  = r
74   rmrI       = total(( mrI#uy)*r,1)/float(cnx) & rmrIs(i,*)  = rmrI
75   rmrBa      = total((mrBa#uy)*r,1)/float(cnx) & rmrBas(i,*) = rmrBa
76   rmrCs      = total((mrCs#uy)*r,1)/float(cnx) & rmrCss(i,*) = rmrCs
77   rmrXe      = total((mrXe#uy)*r,1)/float(cnx) & rmrXes(i,*) = rmrXe
78   rmrB       = total(( mrB#uy)*r,1)/float(cnx) & rmrBs(i,*)  = rmrB
79   rmrW       = total(( mrW#uy)*r,1)/float(cnx) & rmrWs(i,*)  = rmrW
80   ; 6 component inversion I, Ba, Cs, Xe, Bone, Water
81   rtI( i,*) = mrsq(0,0)*rmrI  + mrsq(0,1)*rmrBa + mrsq(0,2)*rmrCs + mrsq(0,3)*rmrXe + mrsq(0,4)*rmrB  + mrsq(0,5)*rmrW
82   rtBa(i,*) = mrsq(1,0)*rmrI  + mrsq(1,1)*rmrBa + mrsq(1,2)*rmrCs + mrsq(1,3)*rmrXe + mrsq(1,4)*rmrB  + mrsq(1,5)*rmrW
83   rtCs(i,*) = mrsq(2,0)*rmrI  + mrsq(2,1)*rmrBa + mrsq(2,2)*rmrCs + mrsq(2,3)*rmrXe + mrsq(2,4)*rmrB  + mrsq(2,5)*rmrW
84   rtXe(i,*) = mrsq(3,0)*rmrI  + mrsq(3,1)*rmrBa + mrsq(3,2)*rmrCs + mrsq(3,3)*rmrXe + mrsq(3,4)*rmrB  + mrsq(3,5)*rmrW
85   rtB( i,*) = mrsq(4,0)*rmrI  + mrsq(4,1)*rmrBa + mrsq(4,2)*rmrCs + mrsq(4,3)*rmrXe + mrsq(4,4)*rmrB  + mrsq(4,5)*rmrW
86   rtW( i,*) = mrsq(5,0)*rmrI  + mrsq(5,1)*rmrBa + mrsq(5,2)*rmrCs + mrsq(5,3)*rmrXe + mrsq(5,4)*rmrB  + mrsq(5,5)*rmrW
87 endfor
88
89 rt   = {     I:rtI,      Ba:rtBa,      Cs:rtCs,     Xe:rtXe,      B:rtB,     W:rtW,     r:rs,   flat:c_flat,   $
90          rmrI:rmrIs,  rmrBa:rmrBas,  rmrB:rmrBs,  rmrW:rmrWs,     es:es,    nes:cnx,    nx:ix,     ny:cny }
91 mus  = {     I:mrI,     Ba:mrBa,     Cs:mrCs,     Xe:mrXe,     B:mrB,     W:mrW,  mrsq:mrsq,    es:es,        nx:ix,        ny:cny   }
92 s    = { rt:rt, mu:mus, nx:ix, ny:cny, es:es, e_info:e_info }
93 return, s
94 end
```

APPENDIX C
SNR EVALUATION BASED ON POISSON STATISTICS

The derivations shown in this appendix were originally done by Ying Zhu, 2012 [166], more details can be found in the cited reference. The slight modification to our SNR evaluation is the assumption that the dark current, N_D is zero which reduces eqn. C.6 to C.7. And thus, the N_{ip} used in eqn. C.9 is slightly different from the original work by Ying Zhu. Here R represents the measurement made at each of the x ray energies, that is, the image data acquired.

With reference to the theoretical framework of section 4.3 of this thesis, for a subject composed of m components and imaged with photons having n number of energies, the projected density equations are given by [90, 165]:

$$\begin{aligned}\rho_j t_j &= \frac{1}{D_{mm}}\left[R_{j1}\frac{1}{n}\sum_i\left(\frac{\mu}{\rho}_{1i} r_i\right)+\ldots+R_{jj}\frac{1}{n}\sum_i\left(\frac{\mu}{\rho}_{ji} r_i\right)+\ldots+R_{jm}\frac{1}{n}\sum_i\left(\frac{\mu}{\rho}_{mi} r_i\right)\right] \\ &= \sum_k R_{jk}\left[\frac{1}{n}\sum_i\left(\frac{\mu}{\rho}_{ki} r_i\right)\right]\frac{1}{D_{mm}}\end{aligned} \tag{C.1}$$

where $$r_i = -\ln\left(\frac{N_i - N_D}{N_{0i} - N_D}\right) = \sum_j \frac{\mu}{\rho}_{ji}\rho_j t_j \qquad (1 \le i \le n,\ 1 \le j \le m,\ n > m) \tag{C.2}$$

Applying propagation of error on eqn. C.1 assumes independent measurements of the incident beam at each energy N_{0i} and the transmitted beam at each energy N_i as well as the measured dark current, N_D

$$\sigma^2_{\rho_j t_j} = \sum_i\left[\left(\frac{\partial \rho_j t_j}{\partial N_i}\right)^2(\delta N_i)^2 + \left(\frac{\partial \rho_j t_j}{\partial N_{0i}}\right)^2(\delta N_{0i})^2 + \left(\frac{\partial \rho_j t_j}{\partial N_D}\right)^2(\delta N_D)^2\right] \tag{C.3}$$

With Poisson statistics, the variance in the photon counts,

$$(\delta N_i)^2 = N_i \qquad (\delta N_{0i})^2 = N_{0i} \qquad (\delta N_D)^2 = N_D$$

The included partial derivatives are,

$$\frac{\partial \rho_j t_j}{\partial N_i} = \frac{\partial \rho_j t_j}{\partial r_i}\frac{\partial r_i}{\partial N_i} \qquad \frac{\partial \rho_j t_j}{\partial N_{0i}} = \frac{\partial \rho_j t_j}{\partial r_i}\frac{\partial r_i}{\partial N_{0i}} \qquad \frac{\partial \rho_j t_j}{\partial N_D} = \frac{\partial \rho_j t_j}{\partial r_i}\frac{\partial r_i}{\partial N_D}$$

$$\frac{\partial r_i}{\partial N_i} = -\frac{\partial}{\partial N_i}\left(\ln\frac{N_i - N_D}{N_{0i} - N_D}\right) = -\frac{1}{N_i - N_D} \qquad \frac{\partial r_i}{\partial N_{0i}} = -\frac{\partial}{\partial N_{0i}}\left(\ln\frac{N_i - N_D}{N_{0i} - N_D}\right) = \frac{1}{N_{0i} - N_D}$$

$$\frac{\partial r_i}{\partial N_D} = -\frac{\partial}{\partial N_D}\left(\ln\frac{N_i - N_D}{N_{0i} - N_D}\right) = \frac{N_{0i} - N_i}{(N_i - N_D)(N_{0i} - N_D)}$$

$$\frac{\partial \rho_j t_j}{\partial r_i} = \frac{1}{D_{mm}}\frac{\partial}{\partial r_i}\left[R_{j1}\frac{1}{n}\sum_i\left(\frac{\mu}{\rho_{1i}}r_i\right) + \ldots + R_{jj}\frac{1}{n}\sum_i\left(\frac{\mu}{\rho_{ji}}r_i\right) + \ldots + R_{jm}\frac{1}{n}\sum_i\left(\frac{\mu}{\rho_{mi}}r_i\right)\right] = \frac{1}{nD_{mm}}\left[R_{j1}\frac{\mu}{\rho_{1i}} + \ldots + R_{jj}\frac{\mu}{\rho_{ji}} + \ldots + R_{jm}\frac{\mu}{\rho_{mi}}\right]$$

The image noise from eqn. C.3 can be determined by combining the above partial derivatives.

$$\sigma^2_{\rho_j t_j} = \sum_i\left[\left(\frac{\partial \rho_j t_j}{\partial N_i}\right)^2(\delta N_i)^2 + \left(\frac{\partial \rho_j t_j}{\partial N_{0i}}\right)^2(\delta N_{0i})^2 + \left(\frac{\partial \rho_j t_j}{\partial N_D}\right)^2(\delta N_D)^2\right]$$

$$= \sum_i\left[\begin{array}{l}\left(\frac{1}{nD_{mm}}\left[R_{j1}\frac{\mu}{\rho_{1i}} + \ldots + R_{jj}\frac{\mu}{\rho_{ji}} + \ldots + R_{jm}\frac{\mu}{\rho_{mi}}\right]\right)^2 \times \\ \left(\left(-\frac{1}{N_i - N_D}\right)^2 N_i + \left(\frac{1}{N_{0i} - N_D}\right)^2 N_{0i} + \left(\frac{N_{0i} - N_i}{(N_i - N_D)(N_{0i} - N_D)}\right)^2 N_D\right)\end{array}\right]$$

$$\sigma^2_{\rho_j t_j} = \frac{1}{n^2 D^2_{mm}}\sum_i\left[\begin{array}{l}\left(R_{j1}\frac{\mu}{\rho_{1i}} + \ldots + R_{jj}\frac{\mu}{\rho_{ji}} + \ldots + R_{jm}\frac{\mu}{\rho_{mi}}\right)^2 \times \\ \left(\left(\frac{1}{N_i - N_D}\right)^2 N_i + \left(\frac{1}{N_{0i} - N_D}\right)^2 N_{0i} + \left(\frac{N_{0i} - N_i}{(N_i - N_D)(N_{0i} - N_D)}\right)^2 N_D\right)\end{array}\right] \qquad \text{(C.4)}$$

$$\sigma^2_{\rho_j t_j} = \frac{1}{n^2 D^2_{mm}}\sum_i\left[\begin{array}{l}\left(R_{j1}\frac{\mu}{\rho_{1i}} + \ldots + R_{jj}\frac{\mu}{\rho_{ji}} + \ldots + R_{jm}\frac{\mu}{\rho_{mi}}\right)^2 \times \\ \left(\frac{(N_{0i} - N_D)^2 N_i + (N_i - N_D)^2 N_{0i} + (N_{0i} - N_i)^2 N_D}{(N_i - N_D)^2(N_{0i} - N_D)^2}\right)\end{array}\right] \qquad \text{(C.5)}$$

For simplification, let

$$\frac{1}{N_{iP}} \equiv \left(\frac{(N_{0i} - N_D)^2 N_i + (N_i - N_D)^2 N_{0i} + (N_{0i} - N_i)^2 N_D}{(N_i - N_D)^2(N_{0i} - N_D)^2}\right) \qquad \text{(C.6)}$$

Assuming $N_D = 0$, eqn. C.6 reduces to

$$\frac{1}{N_{iP}} \equiv \left(\frac{(N_{0i})^2 N_i + (N_i)^2 N_{0i}}{(N_i)^2 (N_{0i})^2} \right) \equiv \left(\frac{N_{0i} + N_i}{N_i N_{0i}} \right) \tag{C.7}$$

Thus, eqn. C.5 becomes

$$\sigma^2_{\rho_j t_j} = \frac{1}{n^2 D^2_{mm}} \sum_i \left[\left(R_{j1} \frac{\mu}{\rho_{1i}} + \ldots + R_{jj} \frac{\mu}{\rho_{ji}} + \ldots + R_{jm} \frac{\mu}{\rho_{mi}} \right)^2 \frac{1}{N_{iP}} \right]$$

That is,

$$\sigma_{\rho_j t_j} = \frac{1}{n D_{mm}} \sqrt{\sum_i \left[\left(R_{j1} \frac{\mu}{\rho_{1i}} + \ldots + R_{jj} \frac{\mu}{\rho_{ji}} + \ldots + R_{jm} \frac{\mu}{\rho_{mi}} \right)^2 \frac{1}{N_{iP}} \right]} \tag{C.8}$$

The SNR for the projected contrast image will be,

$$SNR_j = \frac{\rho_j t_j}{\sigma_{\rho_j t_j}} = \frac{n D_{mm}}{\sqrt{\sum_i \left[\left(R_{j1} \frac{\mu}{\rho_{1i}} + \ldots + R_{jj} \frac{\mu}{\rho_{ji}} + \ldots + R_{jm} \frac{\mu}{\rho_{mi}} \right)^2 \frac{1}{N_{iP}} \right]}} \rho_j t_j \tag{C.9}$$

APPENDIX D
KES, SPECTRAL KES AND MEI SYSTEMS COMPUTER MODEL OF CROSSOVER ARTIFACT

model_plate_crossover_artifact.pro

```
function model_plate_crossover_artifact, min_energy=min_energy, max_energy=max_energy, number_det_pixels=number_det_pixels, materials=materials, $
    plate=plate, x_offset=x_offset, poisson=poisson, pixel=pixel, hkl=hkl, dist_x_det=dist_x_det, mei=mei
n0_poisson = -1
; origin of this system is at the focus
; the x-axis is the central ray at th0 or the ray at the K-edge of the contrast element
; the object or cylinder will move verticallly through the bundle of rays
; x_offset is the distance from the focus that the cylinder goes through the beam
; materials - the materials to be solved for
; obj_material - the material the cylinder is made of
if n_elements(       min_energy) eq 0 then          min_energy =   33.169-0.250 ;I K-Edge
if n_elements(       max_energy) eq 0 then          max_energy =   33.169+0.250 ;I K-Edge
if n_elements(        materials) eq 0 then           materials = ['I','Water']          ; what the program will solve for
if n_elements(            plate) eq 0 then               plate = { height:0.1000, thickness:0.100, material:'Lucite'}
if n_elements(         x_offset) eq 0 then            x_offset =    0.000 ; default is going through the focus
if n_elements(          poisson) ne 0 then          n0_poisson = poisson ;photons per pixel in incident beam on average
if n_elements(number_det_pixels) eq 0 then   number_det_pixels = 51;101
if n_elements(              pixel) eq 0 then                pixel =   0.010 ;0.002 cm pixel size
if n_elements(                hkl) eq 0 then                  hkl =    [3,1,1]
if n_elements(       dist_x_det) eq 0 then          dist_x_det =  300.000 ;cm
geometry  = 'Spectral KES'
spec_flag = 1
mei_flag  = 0
if keyword_set(mei) then begin
  geometry  = 'Multiple Energy Imaging'
  spec_flag = 0
  mei_flag  = 1
endif

nmats     = n_elements(materials)
; xtal
dhkl      = 5.4305/sqrt(total(hkl^2))
; arrangement
dxd       = dist_x_det
lines     = calculate_beam_paths(min_energy=min_energy, max_energy=max_energy, pixel=pixel, hkl=hkl, $
                                 dist_x_det=dist_x_det, number_det_pixels=number_det_pixels, mei=mei, x_offset=x_offset)
nes       = number_det_pixels
es        = lines.es
radius    = plate.height/2.0

nscanpts  = fix(round(4.0*radius/pixel))
ny2       = nscanpts/2
ny        = 2*ny2+1
nx        = ny    ; we will make square images
x         = findgen(nx)*pixel & x = x-(max(x)/2.0)
yscan     = pixel*(findgen(ny)-float(ny2)) + lines.y_offset & scan_rng = max(yscan)-min(yscan)
xscan     = fltarr(ny) + x_offset
traj      = fltarr(2,ny) & traj(0,*)=xscan & traj(1,*)=yscan
;
distances = { pixel:pixel, distance_xtal_detector:lines.dxd, distance_xtal_focus:lines.dxf, $
              distance_focus_detector:lines.dfd, y_scan:yscan, ny:ny, x:x, nx:nx, trajectory:traj, $
              x_offset:x_offset, y_offset:lines.y_offset, energies:lines.es, nes:nes, $
              position_on_detector:-lines.a, size_of_beam_on_detector:pixel*float(nes), lines:lines }
;
; the image field will be square in x & y and order is energy, x, y
; need to extend the object along x...since it is a plate, it is pretty easy
```

Page 1

```
ue          = fltarr(nes)+1.0
uy          = fltarr(ny) +1.0
ux          = fltarr(nx) +1.0
mrs         = fltarr(nmats,nx,nes)
mu_rs       = fltarr(nmats,nes)
beam        = ux#ue
for im=0, nmats-1 do begin
  mr          = murho(materials(im),es)
  mu_rs(im,*) = mr
  mrs(im,*,*) = ux#mr
endfor
m           = general_mean_square_murhos(mrs, beam)

; need attenuation of object - plate

mur_plate = murho(plate.material,es,dens=d_plate) & mu_plate = mur_plate*d_plate
murs       = { solve_for_mu_rs:mu_rs, obj_mu_plate:mu_plate }
; trans number of energies, number of x's and number of y's
trans       = fltarr(nx,nes,ny)
r0          = fltarr(nx,nes,ny)    ;mut
r           = fltarr(nx,nes,ny)    ;poisson
n0          = 1.0
if n_elements(poisson) ne 0 then n0 = randomu(seed,nx,ny,poisson=n0_poisson)
for ie = 0, nes-1 do begin
  a    = lines.a(ie) & b = lines.b(ie) & c = lines.c(ie) & line = [a,b,c]
  thkl = plate_thickness(traj, line, radius, plate.thickness)
  mut  = mu_plate(ie)*(ux#thkl)
  trs  = exp(-mut)
  n    = 1.0 & if n_elements(poisson) ne 0 then n = randomu(seed,nx,ny,poisson=n0_poisson)
  trans(*,ie,*) = trs*n/n0
      r(*,ie,*) = -alog(reform(trans(*,ie,*)))
;print,ie,string(thkl,format="(f5.2,1x)")
;stop
endfor
; now we have "data" and now we need to apply (1) spectral KES and (2) KES
rts     = general_NEI_vector(r,  mrs, m, beam)

; now put all relevant information into a structure to be output
input  = { center_energy:0.5*(min_energy+max_energy), min_energy:min_energy, max_energy:max_energy, $
           materials:materials, plate:plate, x_offset:x_offset, y_offset:lines.y_offset, n0_poisson:n0_poisson, $
           hkl:hkl, pixel:pixel, distances:distances, spec_flag:spec_flag, mei_flag:mei_flag, geometry:geometry }
output = { rts:rts, r:r, mrs:mrs, m:m, beam:beam, energy:es, murs:murs, input:input }

return, output
end
```

```
function model_rod_crossover_artifact, min_energy=min_energy, max_energy=max_energy, number_det_pixels=number_det_pixels, materials=materials, $
    rod=rod, x_offset=x_offset, poisson=poisson, pixel=pixel, hkl=hkl, dist_x_det=dist_x_det, mei=mei
n0_poisson = -1
; origin of this system is at the focus
; the x-axis is the central ray at th0 or the ray at the K-edge of the contrast element
; the object or cylinder will move verticallly through the bundle of rays
; x_offset is the distance from the focus that the cylinder goes through the beam
; materials - the materials to be solved for
; obj_material - the material the cylinder is made of
if n_elements(       min_energy) eq 0 then        min_energy =   33.169-0.250 ;I K-Edge
if n_elements(       max_energy) eq 0 then        max_energy =   33.169+0.250 ;I K-Edge
if n_elements(        materials) eq 0 then         materials = ['I','Water']        ; what the program will solve for
if n_elements(              rod) eq 0 then               rod = { OD:2.5000, material:'Lucite' }
if n_elements(         x_offset) eq 0 then          x_offset =    0.000 ; default is going through the focus
if n_elements(          poisson) ne 0 then        n0_poisson = poisson ;photons per pixel in incident beam on average
if n_elements(number_det_pixels) eq 0 then number_det_pixels =   51
if n_elements(            pixel) eq 0 then              pixel =    0.010 ; cm pixel size
if n_elements(              hkl) eq 0 then                hkl =    [3,1,1]
if n_elements(       dist_x_det) eq 0 then        dist_x_det =  300.000 ;cm
geometry  = 'Spectral KES'
spec_flag = 1
mei_flag  = 0
if keyword_set(mei) then begin
  geometry  = 'Multiple Energy Imaging'
  spec_flag = 0
  mei_flag  = 1
endif

nmats     = n_elements(materials)
; xtal
dhkl      = 5.4305/sqrt(total(hkl^2))
; arrangement
dxd       = dist_x_det
lines     = calculate_beam_paths(min_energy=min_energy, max_energy=max_energy, pixel=pixel, hkl=hkl, $
                                 dist_x_det=dist_x_det, number_det_pixels=number_det_pixels, mei=mei, x_offset=x_offset)
nes       = number_det_pixels
es        = lines.es
;radius    =   0.250 ;cm radius of rod
radius    = rod.OD/2.0

nscanpts  = fix(round(4.0*radius/pixel))
ny2       = nscanpts/2
ny        = 2*ny2+1
nx        = round(0.5*ny)     ; we will make square images
x         = findgen(nx)*pixel & x = x-(max(x)/2.0)
yscan     = pixel*(findgen(ny)-float(ny2)) + lines.y_offset & scan_rng = max(yscan)-min(yscan)
xscan     = fltarr(ny) + x_offset
traj      = fltarr(2,ny) & traj(0,*)=xscan & traj(1,*)=yscan
;
distances = { pixel:pixel, distance_xtal_detector:lines.dxd, distance_xtal_focus:lines.dxf, $
              distance_focus_detector:lines.dfd, y_scan:yscan, ny:ny, x:x, nx:nx, trajectory:traj, $
              x_offset:x_offset, y_offset:lines.y_offset, energies:lines.es, nes:nes, $
              position_on_detector:-lines.a, size_of_beam_on_detector:pixel*float(nes), lines:lines }
;
; the image field will be square in x & y and order is energy, x, y
```

```
; need to extend the object along x...since it is a cylinder, it is pretty easy
ue          = fltarr(nes)+1.0
uy          = fltarr(ny) +1.0
ux          = fltarr(nx) +1.0
mrs         = fltarr(nmats,nx,nes)
mu_rs       = fltarr(nmats,nes)
beam        = ux#ue
for im=0, nmats-1 do begin
  mr            = murho(materials(im),es)
  mu_rs(im,*) = mr
  mrs(im,*,*) = ux#mr
endfor
m           = general_mean_square_murhos(mrs, beam)

; need attenuation of object - rod

mur_rod     = murho( rod.material,es,dens=d_rod) & mu_rod = mur_rod*d_rod
murs        = { solve_for_mu_rs:mu_rs, obj_mu_rod:mu_rod }
; trans number of energies, number of x's and number of y's
trans       = fltarr(nx,nes,ny)
r0          = fltarr(nx,nes,ny)    ;mut
r           = fltarr(nx,nes,ny)    ;poisson
n0          = 1.0
if n_elements(poisson) ne 0 then n0 = randomu(seed,nx,ny,poisson=n0_poisson)
for ie = 0, nes-1 do begin
  a     = lines.a(ie) & b = lines.b(ie) & c = lines.c(ie) & line = [a,b,c]

  thk   = cylinder_thickness(traj, line, radius)
  mut   = mu_rod(ie)*(ux#thk)
  trs   = exp(-mut)
  n     = 1.0 & if n_elements(poisson) ne 0 then n = randomu(seed,nx,ny,poisson=n0_poisson)
  trans(*,ie,*) = trs*n/n0
        r(*,ie,*) = -alog(reform(trans(*,ie,*)))
endfor
; now we have "data" and now we need to apply (1) spectral KES and (2) KES
rts     = general_NEI_vector(r,  mrs, m, beam)

; now put all relevant information into a structure to be output
input  = { center_energy:0.5*(min_energy+max_energy), min_energy:min_energy, max_energy:max_energy, $
  materials:materials, rod:rod, x_offset:x_offset, y_offset:lines.y_offset, n0_poisson:n0_poisson, $
  hkl:hkl, pixel:pixel, distances:distances, spec_flag:spec_flag, mei_flag:mei_flag, geometry:geometry }
output = { rts:rts, r:r, mrs:mrs, m:m, beam:beam, energy:es, murs:murs, input:input }

return, output
end
```

```
function model_tube_crossover_artifact, min_energy=min_energy, max_energy=max_energy, number_det_pixels=number_det_pixels, materials=materials, $
    tube=tube, x_offset=x_offset, poisson=poisson, pixel=pixel, hkl=hkl, dist_x_det=dist_x_det, mei=mei
n0_poisson = -1
; origin of this system is at the focus
; the x-axis is the central ray at th0 or the ray at the K-edge of the contrast element
; the object or cylinder will move vertically through the bundle of rays
; x_offset is the distance from the focus that the cylinder goes through the beam
; materials - the materials to be solved for
; obj_material - the material the cylinder is made of
if n_elements(       min_energy) eq 0 then        min_energy =   33.169-0.250 ;I K-Edge
if n_elements(       max_energy) eq 0 then        max_energy =   33.169+0.250 ;I K-Edge
if n_elements(        materials) eq 0 then         materials = ['I','Water']        ; what the program will solve for
if n_elements(             tube) eq 0 then              tube = { OD:2.5000, ID:2.100, material:'Lucite', $
                                                              content_material:['Water','NaI'], content_concentration:[1.000,0.000]}

if n_elements(         x_offset) eq 0 then          x_offset =     0.000 ; default is going through the focus
if n_elements(          poisson) ne 0 then        n0_poisson = poisson ;photons per pixel in incident beam on average
if n_elements(number_det_pixels) eq 0 then number_det_pixels =   51
if n_elements(            pixel) eq 0 then             pixel =    0.010 ; cm pixel size
if n_elements(              hkl) eq 0 then               hkl =    [3,1,1]
if n_elements(       dist_x_det) eq 0 then        dist_x_det =  300.000 ;cm

geometry  = 'Spectral KES'
spec_flag = 1
mei_flag  = 0
if keyword_set(mei) then begin
  geometry  = 'Multiple Energy Imaging'
  spec_flag = 0
  mei_flag  = 1
endif

nmats     = n_elements(materials)
; xtal
dhkl      = 5.4305/sqrt(total(hkl^2))
; arrangement
dxd       = dist_x_det
lines     = calculate_beam_paths(min_energy=min_energy, max_energy=max_energy, pixel=pixel, hkl=hkl, $
                                 dist_x_det=dist_x_det, number_det_pixels=number_det_pixels, mei=mei, x_offset=x_offset)
nes       = number_det_pixels
es        = lines.es
;radius    =   0.250 ;cm radius of rod
radius    = tube.OD/2.0

nscanpts  = fix(round(4.0*radius/pixel))
ny2       = nscanpts/2
ny        = 2*ny2+1
nx        = ny    ; we will make square images
x         = findgen(nx)*pixel & x = x-(max(x)/2.0)
yscan     = pixel*(findgen(ny)-float(ny2)) + lines.y_offset & scan_rng = max(yscan)-min(yscan)
xscan     = fltarr(ny) + x_offset
traj      = fltarr(2,ny) & traj(0,*)=xscan & traj(1,*)=yscan
;
distances = { pixel:pixel, distance_xtal_detector:lines.dxd, distance_xtal_focus:lines.dxf, $
              distance_focus_detector:lines.dfd, y_scan:yscan, ny:ny, x:x, nx:nx, trajectory:traj, $
              x_offset:x_offset, y_offset:lines.y_offset, energies:lines.es, nes:nes, $
              position_on_detector:-lines.a, size_of_beam_on_detector:pixel*float(nes), lines:lines }
;
```

```
; the image field will be square in x & y and order is energy, x, y
; need to extend the object along x...since it is a cylinder, it is pretty easy
ue          = fltarr(nes)+1.0
uy          = fltarr(ny) +1.0
ux          = fltarr(nx) +1.0
mrs         = fltarr(nmats,nx,nes)
mu_rs       = fltarr(nmats,nes)
beam        = ux#ue
for im=0, nmats-1 do begin
  mr            = murho(materials(im),es)
  mu_rs(im,*) = mr
  mrs(im,*,*) = ux#mr
endfor
m           = general_mean_square_murhos(mrs, beam)

; need attenuation of object - tube has shell and contents
rad_ID      = tube.ID/2.0
mur_shell = murho(tube.material,es,dens=d_shell) & mu_shell = mur_shell*d_shell
ntc         = n_elements(tube.content_material)
mu_conts  = fltarr(nes)
for ic = 0, ntc-1 do begin
  mr        = murho(tube.content_material(ic),es)*tube.content_concentration(ic)
  mu_conts = mu_conts+mr
endfor
murs        = { solve_for_mu_rs:mu_rs, obj_mu_shell:mu_shell, obj_mu_contents:mu_conts }
; trans number of energies, number of x's and number of y's
trans       = fltarr(nx,nes,ny)
r0          = fltarr(nx,nes,ny)    ;mut
r           = fltarr(nx,nes,ny)    ;poisson
n0          = 1.0
if n_elements(poisson) ne 0 then n0 = randomu(seed,nx,ny,poisson=n0_poisson)
for ie = 0, nes-1 do begin
  a     = lines.a(ie) & b = lines.b(ie) & c = lines.c(ie) & line = [a,b,c]

  thk1 = cylinder_thickness(traj, line, radius)
  thk2 = cylinder_thickness(traj, line, rad_ID)
  mut  = mu_shell(ie)*(ux#(thk1-thk2)) + mu_conts(ie)*(ux#thk2)
  trs  = exp(-mut)
  n     = 1.0 & if n_elements(poisson) ne 0 then n = randomu(seed,nx,ny,poisson=n0_poisson)
  trans(*,ie,*) = trs*n/n0
      r(*,ie,*) = -alog(reform(trans(*,ie,*)))
endfor
; now we have "data" and now we need to apply (1) spectral KES and (2) KES
rts     = general_NEI_vector(r,  mrs, m, beam)

; now put all relevant information into a structure to be output
input  = { center_energy:0.5*(min_energy+max_energy), min_energy:min_energy, max_energy:max_energy, $
  materials:materials, tube:tube, x_offset:x_offset, y_offset:lines.y_offset, n0_poisson:n0_poisson, $
  hkl:hkl, pixel:pixel, distances:distances, spec_flag:spec_flag, mei_flag:mei_flag, geometry:geometry }
output = { rts:rts, r:r, mrs:mrs, m:m, beam:beam, energy:es, murs:murs, input:input }

return, output
end
```

```
function model_MEI_plate_crossover_artifact, min_energy=min_energy, max_energy=max_energy, materials=materials, plate=plate, x_offset=x_offset,
poisson=poisson, $
    pixel=pixel, hkl=hkl, dist_x_det=dist_x_det, mei=mei
n0_poisson = -1
; origin of this system is at the focus
; the x-axis is the central ray at th0 or the ray at the K-edge of the contrast element
; the object or cylinder will move verticallly through the bundle of rays
; x_offset is the distance from the focus that the cylinder goes through the beam
; materials - the materials to be solved for
; obj_material - the material the cylinder is made of
if n_elements(       min_energy) eq 0 then          min_energy =   33.169-0.250 ;I K-Edge
if n_elements(       max_energy) eq 0 then          max_energy =   33.169+0.250 ;I K-Edge
if n_elements(        materials) eq 0 then           materials = ['I','Water']        ; what the program will solve for
if n_elements(            plate) eq 0 then               plate = { height:2.5000, thickness:0.100, material:'Lucite'}
if n_elements(         x_offset) eq 0 then            x_offset =    0.000 ; default is going through the focus
if n_elements(          poisson) ne 0 then          n0_poisson = poisson ;photons per pixel in incident beam on average
if n_elements(number_det_pixels) eq 0 then   number_det_pixels = 51
if n_elements(             pixel) eq 0 then                pixel =    0.010 ; cm pixel size
if n_elements(               hkl) eq 0 then                  hkl =    [3,1,1]
if n_elements(       dist_x_det) eq 0 then          dist_x_det =  300.000 ;cm
geometry  = 'Spectral KES'
spec_flag = 1
mei_flag  = 0
if keyword_set(mei) then begin
  geometry  = 'Multiple Energy Imaging'
  spec_flag = 0
  mei_flag  = 1
endif

nmats     = n_elements(materials)
; xtal
dhkl      = 5.4305/sqrt(total(hkl^2))
; arrangement
dxd       = dist_x_det
lines     = calculate_beam_paths(min_energy=min_energy, max_energy=max_energy, pixel=pixel, hkl=hkl, $
                                 dist_x_det=dist_x_det, number_det_pixels=number_detector_pixels, mei=mei, x_offset=x_offset)
nes       = number_det_pixels
es        = lines.es
radius    = plate.height/2.0

nscanpts  = fix(round(4.0*radius/pixel))
ny2       = nscanpts/2
ny        = 2*ny2+1
nx        = ny     ; we will make square images
x         = findgen(nx)*pixel & x = x-(max(x)/2.0)
yscan     = pixel*(findgen(ny)-float(ny2)) + lines.y_offset & scan_rng = max(yscan)-min(yscan)
xscan     = fltarr(ny) + x_offset
traj      = fltarr(2,ny) & traj(0,*)=xscan & traj(1,*)=yscan
;
distances = { pixel:pixel, distance_xtal_detector:lines.dxd, distance_xtal_focus:lines.dxf, $
              distance_focus_detector:lines.dfd, y_scan:yscan, ny:ny, x:x, nx:nx, trajectory:traj, $
              x_offset:x_offset, y_offset:lines.y_offset, energies:lines.es, nes:nes, $
              position_on_detector:-lines.a, size_of_beam_on_detector:pixel*float(nes), lines:lines }
;
; the image field will be square in x & y and order is energy, x, y
```

```
; need to extend the object along x...since it is a plate, it is pretty easy
ue          = fltarr(nes)+1.0
uy          = fltarr(ny) +1.0
ux          = fltarr(nx) +1.0
mrs         = fltarr(nmats,nx,nes)
mu_rs       = fltarr(nmats,nes)
beam        = ux#ue
for im=0, nmats-1 do begin
  mr          = murho(materials(im),es)
  mu_rs(im,*) = mr
  mrs(im,*,*) = ux#mr
endfor
m           = general_mean_square_murhos(mrs, beam)

; need attenuation of object - plate

mur_plate = murho(plate.material,es,dens=d_plate) & mu_plate = mur_plate*d_plate
murs       = { solve_for_mu_rs:mu_rs, obj_mu_plate:mu_plate }
; trans number of energies, number of x's and number of y's
trans      = fltarr(nx,nes,ny)
r0         = fltarr(nx,nes,ny)    ;mut
r          = fltarr(nx,nes,ny)    ;poisson
n0         = 1.0
if n_elements(poisson) ne 0 then n0 = randomu(seed,nx,ny,poisson=n0_poisson)
for ie = 0, nes-1 do begin
  a    = lines.a(ie) & b = lines.b(ie) & c = lines.c(ie) & line = [a,b,c]
  thk1 = plate_thickness(traj, line, radius, plate.thickness)
  mut  = mu_plate(ie)*(ux#thk1)
  trs  = exp(-mut)
  n    = 1.0 & if n_elements(poisson) ne 0 then n = randomu(seed,nx,ny,poisson=n0_poisson)
  trans(*,ie,*) = trs*n/n0
      r(*,ie,*) = -alog(reform(trans(*,ie,*)))

endfor
; now we have "data" and now we need to apply (1) spectral KES and (2) KES
rts     = general_NEI_vector(r,  mrs, m, beam)

; now put all relevant information into a structure to be output
input  = { center_energy:0.5*(min_energy+max_energy), min_energy:min_energy, max_energy:max_energy, $
           materials:materials, plate:plate, x_offset:x_offset, y_offset:lines.y_offset, n0_poisson:n0_poisson, $
           hkl:hkl, pixel:pixel, distances:distances, spec_flag:spec_flag, mei_flag:mei_flag, geometry:geometry }
output = { rts:rts, r:r, murs:murs, input:input }

return, output
end
```

```
function model_MEI_rod_crossover_artifact, min_energy=min_energy, max_energy=max_energy, materials=materials, rod=rod, x_offset=x_offset,
poisson=poisson, $
    pixel=pixel, hkl=hkl, dist_x_det=dist_x_det, mei=mei
n0_poisson = -1
; origin of this system is at the focus
; the x-axis is the central ray at th0 or the ray at the K-edge of the contrast element
; the object or cylinder will move verticallly through the bundle of rays
; x_offset is the distance from the focus that the cylinder goes through the beam
; materials - the materials to be solved for
; obj_material - the material the cylinder is made of
if n_elements(       min_energy) eq 0 then        min_energy =   33.169-0.250 ;I K-Edge
if n_elements(       max_energy) eq 0 then        max_energy =   33.169+0.250 ;I K-Edge
if n_elements(        materials) eq 0 then         materials = ['I','Water']        ; what the program will solve for
if n_elements(              rod) eq 0 then               rod = { OD:2.5000, material:'Lucite' }
if n_elements(         x_offset) eq 0 then          x_offset =    0.000 ; default is going through the focus
if n_elements(          poisson) ne 0 then        n0_poisson = poisson ;photons per pixel in incident beam on average
if n_elements(number_det_pixels) eq 0 then number_det_pixels =   51
if n_elements(            pixel) eq 0 then              pixel =    0.010 ; cm pixel size
if n_elements(              hkl) eq 0 then              hkl =    [3,1,1]
if n_elements(       dist_x_det) eq 0 then        dist_x_det =  300.000 ;cm
geometry  = 'Spectral KES'
spec_flag = 1
mei_flag  = 0
if keyword_set(mei) then begin
  geometry  = 'Multiple Energy Imaging'
  spec_flag = 0
  mei_flag  = 1
endif

nmats     = n_elements(materials)
; xtal
dhkl      = 5.4305/sqrt(total(hkl^2))
; arrangement
dxd       = dist_x_det
lines     = calculate_beam_paths(min_energy=min_energy, max_energy=max_energy, pixel=pixel, hkl=hkl, $
                                 dist_x_det=dist_x_det, number_det_pixels=number_detector_pixels, mei=mei, x_offset=x_offset)
nes       = number_det_pixels
es        = lines.es
;radius    =   0.250 ;cm radius of rod
radius    = rod.OD/2.0

nscanpts  = fix(round(4.0*radius/pixel))
ny2       = nscanpts/2
ny        = 2*ny2+1
nx        = ny    ; we will make square images
x         = findgen(nx)*pixel & x = x-(max(x)/2.0)
yscan     = pixel*(findgen(ny)-float(ny2)) + lines.y_offset & scan_rng = max(yscan)-min(yscan)
xscan     = fltarr(ny) + x_offset
traj      = fltarr(2,ny) & traj(0,*)=xscan & traj(1,*)=yscan
;
distances = { pixel:pixel, distance_xtal_detector:lines.dxd, distance_xtal_focus:lines.dxf, $
              distance_focus_detector:lines.dfd, y_scan:yscan, ny:ny, x:x, nx:nx, trajectory:traj, $
              x_offset:x_offset, y_offset:lines.y_offset, energies:lines.es, nes:nes, $
              position_on_detector:-lines.a, size_of_beam_on_detector:pixel*float(nes), lines:lines }
;
```

```
; the image field will be square in x & y and order is energy, x, y
; need to extend the object along x...since it is a cylinder, it is pretty easy
ue          = fltarr(nes)+1.0
uy          = fltarr(ny) +1.0
ux          = fltarr(nx) +1.0
mrs         = fltarr(nmats,nx,nes)
mu_rs       = fltarr(nmats,nes)
beam        = ux#ue
for im=0, nmats-1 do begin
  mr            = murho(materials(im),es)
  mu_rs(im,*) = mr
  mrs(im,*,*) = ux#mr
endfor
m           = general_mean_square_murhos(mrs, beam)

; need attenuation of object - rod

mur_rod     = murho( rod.material,es,dens=d_rod) & mu_rod = mur_rod*d_rod
murs        = { solve_for_mu_rs:mu_rs, obj_mu_rod:mu_rod }
; trans number of energies, number of x's and number of y's
trans       = fltarr(nx,nes,ny)
r0          = fltarr(nx,nes,ny)    ;mut
r           = fltarr(nx,nes,ny)    ;poisson
n0          = 1.0
if n_elements(poisson) ne 0 then n0 = randomu(seed,nx,ny,poisson=n0_poisson)
for ie = 0, nes-1 do begin
  a     = lines.a(ie) & b = lines.b(ie) & c = lines.c(ie) & line = [a,b,c]

  thk   = cylinder_thickness(traj, line, radius)
  mut   = mu_rod(ie)*(ux#thk)
  trs   = exp(-mut)
  n     = 1.0 & if n_elements(poisson) ne 0 then n = randomu(seed,nx,ny,poisson=n0_poisson)
  trans(*,ie,*) = trs*n/n0
      r(*,ie,*) = -alog(reform(trans(*,ie,*)))
endfor
; now we have "data" and now we need to apply (1) spectral KES and (2) KES
rts     = general_NEI_vector(r,  mrs, m, beam)

; now put all relevant information into a structure to be output
input  = { center_energy:0.5*(min_energy+max_energy), min_energy:min_energy, max_energy:max_energy, $
  materials:materials, rod:rod, x_offset:x_offset, y_offset:lines.y_offset, n0_poisson:n0_poisson, $
  hkl:hkl, pixel:pixel, distances:distances, spec_flag:spec_flag, mei_flag:mei_flag, geometry:geometry }
output = { rts:rts, r:r, mrs:mrs, m:m, beam:beam, energy:es, murs:murs, input:input }

return, output
end
```

```
function model_MEI_tube_crossover_artifact, min_energy=min_energy, max_energy=max_energy, materials=materials, tube=tube, x_offset=x_offset,
 poisson=poisson, $
    pixel=pixel, hkl=hkl, dist_x_det=dist_x_det, mei=mei
n0_poisson = -1
; origin of this system is at the focus
; the x-axis is the central ray at th0 or the ray at the K-edge of the contrast element
; the object or cylinder will move verticallly through the bundle of rays
; x_offset is the distance from the focus that the cylinder goes through the beam
; materials - the materials to be solved for
; obj_material - the material the cylinder is made of
if n_elements(       min_energy) eq 0 then        min_energy = 33.169-0.250  ;28.4250 ;I K-Edge
if n_elements(       max_energy) eq 0 then        max_energy = 33.169+0.250  ;45.9342 ;I K-Edge
if n_elements(        materials) eq 0 then         materials = ['I','Water']        ; what the program will solve for
if n_elements(             tube) eq 0 then              tube = { OD:1.1900, ID:0.9600, material:'Lucite', $
                                                             content_material:['Water','NaI'], content_concentration:[1.000,0.0045]}
if n_elements(         x_offset) eq 0 then          x_offset =    0.000 ; default is going through the focus
if n_elements(          poisson) ne 0 then        n0_poisson = poisson ;photons per pixel in incident beam on average
if n_elements(number_det_pixels) eq 0 then number_det_pixels = 51    ;881
if n_elements(              pixel) eq 0 then              pixel =    0.010 ; cm pixel size
if n_elements(                hkl) eq 0 then               hkl =    [3,1,1]
if n_elements(       dist_x_det) eq 0 then        dist_x_det = 300.00 ;129.00  ;300.000 ;cm
geometry  = 'Spectral KES'
spec_flag = 1
mei_flag  = 0
if keyword_set(mei) then begin
  geometry  = 'Multiple Energy Imaging'
  spec_flag = 0
  mei_flag  = 1
endif

nmats     = n_elements(materials)
; xtal
dhkl      = 5.4305/sqrt(total(hkl^2))
; arrangement
dxd       = dist_x_det
lines     = calculate_beam_paths(min_energy=min_energy, max_energy=max_energy, pixel=pixel, hkl=hkl, $
                                 dist_x_det=dist_x_det, number_det_pixels=number_detector_pixels, mei=mei, x_offset=x_offset)
nes       = number_det_pixels
es        = lines.es
;radius    =   0.250 ;cm radius of rod
radius    = tube.OD/2.0

nscanpts  = fix(round(4.0*radius/pixel))
ny2       = nscanpts/2
ny        = 2*ny2+1
nx        = ny    ; we will make square images
x         = findgen(nx)*pixel & x = x-(max(x)/2.0)
yscan     = pixel*(findgen(ny)-float(ny2)) + lines.y_offset & scan_rng = max(yscan)-min(yscan)
xscan     = fltarr(ny) + x_offset
traj      = fltarr(2,ny) & traj(0,*)=xscan & traj(1,*)=yscan
;
distances = { pixel:pixel, distance_xtal_detector:lines.dxd, distance_xtal_focus:lines.dxf, $
              distance_focus_detector:lines.dfd, y_scan:yscan, ny:ny, x:x, nx:nx, trajectory:traj, $
              x_offset:x_offset, y_offset:lines.y_offset, energies:lines.es, nes:nes, $
              position_on_detector:-lines.a, size_of_beam_on_detector:pixel*float(nes), lines:lines }
```

```
;
; the image field will be square in x & y and order is energy, x, y
; need to extend the object along x...since it is a cylinder, it is pretty easy
ue          = fltarr(nes)+1.0
uy          = fltarr(ny) +1.0
ux          = fltarr(nx) +1.0
mrs         = fltarr(nmats,nx,nes)
mu_rs       = fltarr(nmats,nes)
beam        = ux#ue
for im=0, nmats-1 do begin
  mr            = murho(materials(im),es)
  mu_rs(im,*) = mr
  mrs(im,*,*) = ux#mr
endfor
m           = general_mean_square_murhos(mrs, beam)

; need attenuation of object - tube has shell and contents
rad_ID      = tube.ID/2.0
mur_shell = murho(tube.material,es,dens=d_shell) & mu_shell = mur_shell*d_shell
ntc         = n_elements(tube.content_material)
mu_conts    = fltarr(nes)
for ic = 0, ntc-1 do begin
  mr        = murho(tube.content_material(ic),es)*tube.content_concentration(ic)
  mu_conts = mu_conts+mr
endfor
murs        = { solve_for_mu_rs:mu_rs, obj_mu_shell:mu_shell, obj_mu_contents:mu_conts }
; trans number of energies, number of x's and number of y's
trans       = fltarr(nx,nes,ny)
r0          = fltarr(nx,nes,ny)    ;mut
r           = fltarr(nx,nes,ny)    ;poisson
n0          = 1.0
if n_elements(poisson) ne 0 then n0 = randomu(seed,nx,ny,poisson=n0_poisson)
for ie = 0, nes-1 do begin
  a     = lines.a(ie) & b = lines.b(ie) & c = lines.c(ie) & line = [a,b,c]

  thk1 = cylinder_thickness(traj, line, radius)
  thk2 = cylinder_thickness(traj, line, rad_ID)
  mut  = mu_shell(ie)*(ux#(thk1-thk2)) + mu_conts(ie)*(ux#thk2)
  trs  = exp(-mut)
  n    = 1.0 & if n_elements(poisson) ne 0 then n = randomu(seed,nx,ny,poisson=n0_poisson)
  trans(*,ie,*) = trs*n/n0
      r(*,ie,*) = -alog(reform(trans(*,ie,*)))
endfor
; now we have "data" and now we need to apply (1) spectral KES and (2) KES
rts     = general_NEI_vector(r,  mrs, m, beam)

; now put all relevant information into a structure to be output
input  = { center_energy:0.5*(min_energy+max_energy), min_energy:min_energy, max_energy:max_energy, $
  materials:materials, tube:tube, x_offset:x_offset, y_offset:lines.y_offset, n0_poisson:n0_poisson, $
  hkl:hkl, pixel:pixel, distances:distances, spec_flag:spec_flag, mei_flag:mei_flag, geometry:geometry }
output = { rts:rts, r:r, mrs:mrs, m:m, beam:beam, energy:es, murs:murs, input:input }

return, output
end

```

APPENDIX E
CROSSOVER ARTIFACT REDUCTION ALGORITHMS

output_fix_plate_model.pro

```
pro output_fix_plate_model, s, output_path, display=display, write=write, name=name

output_plate_model, s, output_path, display=display, write=write, name=name
snew    = FIND_FIX_SPECTRAL_CROSSOVER(s, /plot, /loop, error=0.001, slope=slope)
dfd     = s.input.distances.distance_focus_detector
xoc     = dfd*slope
xocs    = 'Offset_Corr_'+strf(xoc,9,4)+'cm'
print, xocs
if n_elements(name) eq 0 then fname  = 'Fixed_'+xocs
if n_elements(name) ne 0 then fname  = 'Fixed_'+xocs+'_'+name
if n_elements(name) eq 0 then cname  = 'Compare'
if n_elements(name) ne 0 then cname  = 'Compare_'+name
output_plate_model, snew, output_path, display=display, write=write, name=fname
output_plate_model_compare, s, snew, output_path, display=display, write=write, name=cname, /separate
return
end
```

Page 1

output_fix_rod_model.pro

```
pro output_fix_rod_model, s, output_path=output_path, display=display, write=write, name=name

output_rod_model, s, output_path=output_path, display=display, write=write, name=name
snew   = FIND_FIX_SPECTRAL_CROSSOVER(s, /plot, /loop, error=0.001, slope=slope)
dfd    = s.input.distances.distance_focus_detector
xoc    = dfd*slope
xocs   = 'Offset_Corr_'+strf(xoc,9,4)+'cm'
print, xocs
if n_elements(name) eq 0 then fname  = 'Fixed_'+xocs
if n_elements(name) ne 0 then fname  = 'Fixed_'+xocs+'_'+name
if n_elements(name) eq 0 then cname  = 'Compare'
if n_elements(name) ne 0 then cname  = 'Compare_'+name
output_rod_model, snew, output_path=output_path, display=display, write=write, name=fname
output_rod_model_compare, s, snew, output_path, display=display, write=write, name=cname, /separate
return
end
```

```
1 pro output_fix_tube_model, s, output_path, display=display, write=write, name=name
2
3 output_tube_model, s, output_path, display=display, write=write, name=name
4 snew   = FIND_FIX_SPECTRAL_CROSSOVER(s, /plot, /loop, error=0.001, slope=slope)
5 dfd    = s.input.distances.distance_focus_detector
6 xoc    = dfd*slope
7 xocs   = 'Offset_Corr_'+strf(xoc,9,4)+'cm'
8 print, xocs
9 if n_elements(name) eq 0 then fname  = 'Fixed_'+xocs
10 if n_elements(name) ne 0 then fname  = 'Fixed_'+xocs+'_'+name
11 if n_elements(name) eq 0 then cname  = 'Compare'
12 if n_elements(name) ne 0 then cname  = 'Compare_'+name
13 output_tube_model, snew, output_path, display=display, write=write, name=fname
14 output_tube_model_compare, s, snew, output_path, display=display, write=write, name=cname, /separate
15 return
16 end
17
18
19
20
21
22
```

```
pro output_fix_spectral, s, output_path, display=display, write=write, name=name, flatten=flatten

output_data_spectral, s, output_path, display=display, write=write, name=name, scales=scales, flatten=flatten
err      = FIND_XOVER_IMAGE_CORRECTION(s.r, s.beam, slope=slope,/plot)
rnew     = SHIFT_XVSE_XEY_ARRAY(err, s.r, /shift)
rtsnew   = general_nei_vector(rnew, s.mrs, s.m, s.beam)
;snew    = FIND_FIX_SPECTRAL_CROSSOVER(s, /plot, /loop, error=0.001, slope=slope, flatten=flatten)
snew     = s
snew.rts = rtsnew

dxd      = s.s.beam_parameters.dist_xtal_det
dxf      = s.s.beam_parameters.f2r
dfd      = (dxd-dxf)/10.0 ;dxd & dxf is in mm
xoc      = dfd*slope
xocs     = 'Offset_Corr_'+strf(xoc,9,4)+'cm'
print, xocs
if n_elements(name) eq 0 then fname  = 'Fixed_'+xocs
if n_elements(name) ne 0 then fname  = 'Fixed_'+xocs+'_'+name
if n_elements(name) eq 0 then cname  = 'Compare'
if n_elements(name) ne 0 then cname  = 'Compare_'+name
output_data_spectral, snew, output_path, display=display, write=write, name=fname, in_scale=scales, flatten=flatten
output_data_spectral_compare, s, snew, output_path, display=display, write=write, name=cname, /separate, flatten=flatten
return
end
```

```
pro output_fix_data6, s, output_path, display=display, write=write, name=name

output_data6, s, output_path, display=display, write=write, name=name, scales=scales
err      = FIND_XOVER_IMAGE_CORRECTION(s.r, s.beam, slope=slope)
;err      = FIND_X_OVER_CORRECTION(s.r, slope=slope)
rnew     = SHIFT_XVSE_XEY_ARRAY(err, s.r, /shift)
rtsnew   = general_nei_vector(rnew, s.mrs, s.m, s.beam)
snew     = s
snew.rts = rtsnew
dfd      = s.s.e_info.d/10.0 ;d is in mm
xoc      = dfd*slope
xocs     = 'Offset_Corr_'+strf(xoc,9,4)+'cm'
print, xocs
if n_elements(name) eq 0 then fname  = 'Fixed_'+xocs
if n_elements(name) ne 0 then fname  = 'Fixed_'+xocs+'_'+name
if n_elements(name) eq 0 then cname  = 'Compare'
if n_elements(name) ne 0 then cname  = 'Compare_'+name
output_data6, snew, output_path, display=display, write=write, name=fname, in_scale=scales
output_data6_compare, s, snew, output_path, display=display, write=write, name=cname, /separate
return
end
```